NONINVASIVE ULTRASOUND MEASUREMENT OF TEMPERATURE DISTRIBUTION IN REFRACTORIES OF COAL AND BIOMASS GASIFIERS

by

Yunlu Jia

A dissertation submitted to the faculty of
The University of Utah
in partial fulfillment of the requirements for the degree of

Doctor of Philosophy

Department of Chemical Engineering

The University of Utah

August 2015

The University of Utah Graduate School

STATEMENT OF DISSERTATION APPROVAL

The dissertation of **Yunlu Jia**

has been approved by the following supervisory committee members:

Mikhail Skliar	, Chair	**05-18-2015** Date Approved
Anthony Butterfield	, Member	**05-04-2015** Date Approved
Douglas A. Christensen	, Member	**05-04-2015** Date Approved
Eric Eddings	, Member	**05-04-2015** Date Approved
Kevin Whitty	, Member	**05-04-2015** Date Approved

and by **Milind Deo** , Chair/Dean of

the Department/College/School of **Chemical Engineering**

and by David B. Kieda, Dean of The Graduate School.

ABSTRACT

A gasifier's temperature is the primary characteristic that must be monitored to ensure its performance and the longevity of its refractory. One of the key technological challenges impacting the reliability and economics of coal and biomass gasification is the lack of temperature sensors that are capable of providing accurate, reliable, and long-life performance in an extreme gasification environment.

This research has proposed, demonstrated, and validated a novel approach that uses a noninvasive ultrasound method that provides real-time temperature distribution monitoring across the refractory, especially the hot face temperature of the refractory.

The essential idea of the ultrasound measurements of segmental temperature distribution is to use an ultrasound propagation waveguide across a refractory that has been engineered to contain multiple internal partial reflectors at known locations. When an ultrasound excitation pulse is introduced on the cold side of the refractory, it will be partially reflected from each scatterer in the US propagation path in the refractory wall and returned to the receiver as a train of partial echoes. The temperature in the corresponding segment can be determined based on recorded ultrasonic waveform and experimentally defined relationship between the speed of sound and temperature.

The ultrasound measurement method offers a powerful solution to provide continuous real-time temperature monitoring for the occasions that conventional thermal, optical, and other sensors are infeasible, such as the impossibility of insertion of temperature sensors, harsh environment, unavailable optical path, and more. Our developed ultrasound system consists of an ultrasound engineered waveguide, ultrasound transducer/receiver, and data acquisition, logging, interpretation, and online display system, which is simple to install on the existing units with minimal modification on the gasifier or to use with new units.

This system has been successfully tested with a 100 kW pilot-scale downflow oxyfuel combustor, capturing in real-time temperature changes during all relevant combustion process changes. The ultrasound measurements have excellent agreement with thermocouple measurements, and appear to be more sensitive to temperature changes before the thermocouples response, which is believed to be the first demonstration of ultrasound measurements segmental temperature distribution across refractories.

CONTENTS

LIST OF FIGURES

LIST OF TABLES

ACRONYMS

The National Energy Technology Laboratory (NETL)

One-dimensional (1D)

Two-dimensional (2D)

Three-dimensional (3D)

Thermocouple (TC)

Resistance temperature device (RTD)

Coefficient of thermal expansion (CTE)

Fiber bragg grating (FBG)

Ultrasound (US)

Nondestructive testing (NDT)

Speed of sound (SOS)

Time of flight (TOF)

Ultrasound measurements of segmental temperature distribution (US-MSTD)

Internal diameter (I.D.)

Signal-to-noise ratio (SNR)

Oxyfuel combustor (OFC)

Partial stabilized zirconia (PSZ)

Tetragonal zirconia polycrystal (TZP)

Yttria stabilized zirconia polycrystal (Y-TZP)

Surface acoustic wave (SAW)

CHAPTER 1

INTRODUCTION

1.1 Background and Motivation

1.1.1 Gasficiation and Gasifier

Modern day gasification technology was first introduced by the oil industry to process low-value petroleum and its by-products. Since the 1970s, the gasification process has adapted to a variety of carbon-based feedstocks, such as coals, low-cost, widely available petroleum coke, biomass, and agriculture (solid) waste [43].

Gasification technology has been predicted to be a major source of clean-fuel technology for the coming future. Gasification involves the thermal beakdown of carbon rich materials in a hot, reactive environment to produce synthesis gas, or syngas, which is rich in hydrogen (H_2) and carbon monoxide (CO). The produced syngas can then be used as an alternative feedstock for many chemical processes, such as those used in methanol, butanol, dimethyl ether, diesel, and gasoline production. When used in power generation, the syngas produced by coal or biomass gasifiers is burned as a fuel in carbon neutral or carbon capture-ready power generation. Gasification plants tend to use less makeup water and produce less solid waste and airborne pollutants than typical coal combustion-based plants. Gasifiers mainly consume oxygen (O_2), instead of air, which is more efficient and economical during the conversion of the carbon feedstock, carbon dioxide (CO_2) separation, capture, and sequestration [56]. The ability of eliminating most air pollutants and potential greenhouse gases makes gasification a more environmentally sustainable technology for the energy plants compared with traditional coal combustion. Gasification-based electric power plants are operating commercially in many countries.

There are three major types of commercially-available gasifiers based on their

feedstock and end-product requirements: fixed bed gasifiers, fluidized bed gasifiers, and entrained bed gasifiers. Gasifiers can also be grouped based on their ash treatment: slagging gasifier and nonslagging gasifier. A nonslagging gasifier normally operates at temperatures below the ash melting point of the feedstock, which is about 500–600 °C. This type of gasifier is much easier to operate, since the wall temperature is significantly low so that it does not require a refractory lining. However, the transformations of the inorganic to ash form in nonslagging gasifier sometimes cause a heavy metal leaching problem [109]. In addition, due to its low operating temperature, air-blown gasification is more favorable than oxygen-blown gasification, which would cause the low efficiency of carbon capture [77]. A slagging gasifier operates at a temperature that is higher than the feedstock ash melting point. The ashes are present in a liquid form (molten slags) that can flow down and be removed regularly. This type of gasifier offers advantages, such as high gas production capacity, lower steam consumption, absence of tars and oils in the product steam, and relatively easy disposal of waste during operation. Examples of the slagging gasifiers include (1) for the fixed-bed system: Lurgi Dry-Ash and British Gas/Lurgi gasifiers; (2) for the fluidized bed system: KBR Transpoint, High Temperature Winkler, and ICC/CAS AFB gasifiers; (3) for the entrained-bed system: GE Energy (formerly Chevron Texaco), Shell, and CB& I E-Gas^{TM} gasifiers [25]. However, this high efficient gasification process generally involves high temperatures and pressures, and aggressive chemical composites which would results in an extraordinarily severe environment for the structural components of the slagging gasification system [21].

Typical operating conditions are a temperature of 1300 °C (slurry feed) or 1500–1800 °C (dry feed) and pressure of 0.15 to 2.45 MPa for fixed bed gasifiers, 900–1200 °C and up to 2.94 MPa for a fluidized bed, and 1200–1600 °C and 2–8 MPa for entrained flow gasifiers [70]. The overall reaction of gasification is shown as follows:

$C + H_2O(\text{steam}) + O_2(\text{shortage}) \longrightarrow CO + H_2 + CO_2 + \text{minority gases} + \text{by-products} + \text{heat}.$

The minority gases in a slagging gasifier primarily consist of H_2O (steam), H_2,

CO, and CO_2, and small amounts of methane (CH_4), N_2, NH_3, and H_2S may also exist. The by-products, in ash or slag form, are basically mixtures of various oxides, such as SiO_2, Al_2O_3, FeO, CaO, MgO, Fe_2O_3, MnO, Na_2O_3, K_2O, TiO_3, TiO_2, and P_2O_5 [9].

The adopted temperatures and pressures in a slagging gasifier generally depend on the specific gasification process and the reactivity of the feedstock. Increasing gasification temperature and pressure can usually increase operational efficiency and reduce the size of gasifier. The high temperatures are not permissible for the vessel shell of the gasifier, and thus the shell is generally protected by a refractory lining system.

1.1.2 Gasifier Lining Wear and Failure

The refractory lining system provides resistance to extreme operating conditions and insulates the gasifier from energy loss. The lining system is composed of refractory linings, generally two to six layers of bricks with proper mortar joints and cooling systems. The emphasis on liner materials is on the hot-face refractory materials, which are exposed to the most aggressive environment. At these elevated temperatures and pressures, the processing gases and by-products, especially in slag form, attack the refractory lining in various ways.

The steam can oxidize the iron-containing metal shell and cause cracking and spalling problems in the shells during heating cycles. Such problems become very severe at high temperature levels. At high temperatures, steam can affect refractory materials by causing the extraction of soluble oxides or hydroxides, resulting in the reduction of refractory strength and erosion resistance.

The feedstock ashes melt into fluid slags in the high temperature and are maintained as a liquid state in slagging gasifiers. Slags run down the wall, flow over the bed of the gasifier, and pass through a slag tap to a quench tank where slags are removed continuously. This concept provides an easy method for waste disposal and creates minimal environmental problems. This slag penetrates and reacts with the refractory, causing degradation and corossion resulting from a combination of mechanical stresses and thermal expansion mismatches. The gasifier operating conditions and slag chemistry have a significant impact on the performance of

refractories.

Refractory linings under slagging coal gasification experience the combination of a chemical (reaction and phase change) and physical (erosion) effect, followed by a failure in required performance [95]. The molten slag is corrosive to the hot face refractory of the gasifier. The corrosion process involves three mechanisms: dissolution, penetration, and erosion. Refractories exposed to slag might be irregularly dissolved in slag. This causes continuous loss in mass and thickness of the refractory linings. Since refractory material is porous, slag may penetrate into refractories that reacts and chemically dissolves the refractory material, causing degradation and corrosion. The penetration of slags into refractories depends on the porosity and the temperature of the refracoties. Chemical erosion creates local microcracking, weakens material mechanical properties, and causes cracking and spalling problems in the refractories. In addition, the combination of thermal expansion mismatch and boundary confinement between the refractory brick and the slag causes cracking and joint failure in the lining. This leads to gradual development of several microstructural cracks inside the refractory surface, which eventually merge together into bulk removal of material of refractory walls.

High-alumina and high-chromia dense refractories are usually used in slagging gasifiers. Erosion is not a governing destructive factor for hot face refractories in slagging gasifiers. However, the chemical dissolution of refractory walls degrades the material mechanical strength and irregular dissolution of the material leads to fatigue damage. Fatigue crack growth leads to further slag penetration that, in turn, causes more chemical dissolution.

The slag and harsh gasifier environment are core issues challenging the gasifier lining's refractory service life and key barriers to generalize commercialization of gasification technology. The expected refractory lining should have a reliable life of at least 3 years. Current refractories last 4–18 months, which has yet to meet the desired service life [27]. The replacement cost of a failed refractory lining is over 1 million U.S. dollars, both in terms of the material cost (depending on gasifier size and rebuild requirements) and also in terms of 2–3 weeks lost production time. Research for improving refractory products that can withstand these environments

for a continuous, efficient, and reliable gasification process has not stopped [9], [68].

The National Energy Technology Laboratory (NETL) has worked with Harbison-Walker Refractory Company to develop a new refractory, which was designed specifically for longer service life in gasifier. This patented technology has been on market as Aurex® 95P. This new refractory has been tested at several commercial gasifier sites in the United States and showed significantly improved performance relative to other commercially-available materials [8].

Early detection of initial damage in the refractory walls is necessary to prevent unscheduled shutdown of a gasification plant. A real-time diagnosis tool with capabilities of generating early warnings is critical for extending the refractory's service life. The pivotal idea for damage detection and prediction of the refractory wall in particular and the entire gasification system in general is built upon the fact that a local anomaly is likely to influence the temperature gradient in the refractory wall due to changes in the thermal impedance. Current degradation monitoring of slagging gasifiers provides a variety of fault diagnostic methodologies that are primarily built upon microstructural analytical models of damaged refractory bricks. However, lack of real-time sensor-based information is one of the major technical challenges for accurate refractory damage diagnosis.

An optimum refractory monitoring system should involve information of thermomechanical material and system behavior, corrosion behavior, and their interaction in the gasification environment. Temperature profile is one of most important sensor-based parameters required for the refractories over an extended period of operation. The mechanical properties of refractories, including compressive strength, tensile strength, Young's modulus, and creep rate, are primarily temperature- and load history-dependent. As the critical temperature is reached, refractories lose their strength. This critical temperature depends on the melting point and refractoriness of the materials. The strength loss results in excessive deformation and the loss of load-carrying capability with the consequent loss in integrity of the lining system [21].

Both steady state spatial temperature distributions and dynamic temperature profiles undergo different types of changes that provide important information

for detection and identification of an anomalous plant condition. Temperature variations across the cross-section of the gasifer lining at different vertical levels can be used to predict the slag flow and refractory dissolution, something difficult to monitor during the gasification. Using the integrated model of heat transfer, heat loss and heat flux can be calculated based on refractory temperature profiles. [19].

Furthermore, since a gasifier reactor uses a multilayered lining, temperature profiles are important in understanding the thermal interaction between complex layers, choosing proper combinations of materials that will prevent overheating of refractories and improve energy conversion efficiency. Temperature along the refractory wall is also a key input for the 2D and 3D stress analysis for the gasifier support structures, such as the shell and anchors.

1.2 Current Temperature Measurement Techniques

1.2.1 Direct Measurements

The current dominant temperature measurement technology for gasifiers is the classic thermocouple (TC) or electrical resistance temperature device (RTD) probe. The most common material used in TCs is precious platinum-rhodium that can handle the extreme temperature measurement range. However, TCs are very susceptible to the harsh operating environment inside the slagging gasifier and often fail within hours of gasifier start-up, leaving the operator with no real-time means of temperature measurement. The conventional approach is to create a more corrosion-resistant thermocouple using a ceramic sheath or an improved filler material. An improved filler material has been developed by NETL, along with a dry-pressing method of manufacture that can be readily adapted to a commercial setting, which has proven to have limited effectiveness in the aggressive gasifier environment [27]. However, the heavy sheathing makes such devices less sensitive to dynamic changes in temperatures. In addition, protective sheathings degrade with time under the attack of the ash and slag, causing erosion damage, which would lead to delayed read-out and faulty readings. Metal-based-improved TCs have a typical life less than 120 days. Failure rates can be up to 50% within 15 days, and 75% within 30 days. This is especially true for entrained flow slagging

gasifiers since even the most hardened sensors are unlikely to survive for more than 1 or 2 months as the inner surface of the refractory wall degrades and recesses, exposing sensors directly to the corrosive slagging environment. Alkali vapors and transition metals attachments, and solid coal slag build-ups affect thermocouple measurement and accelerate surface corrosion. Above the material limits, TCs can disintegrate completely [7]. The large thermal ramps and mechanical stresses the TC probe suffers cause multimaterial probe mechanical failure due to coefficient of thermal expansion (CTE) mismatch of probe materials [10]. Although local nitrogen or other purge gas may provide protection for TCs, this would result in understated temperatures.

In reality, the gasifier operator would sacrifice the temperature measurement absolute value for a continuous and steady temperature reading. The approach is not to position the TCs' tips flush with the refractory wall, but slightly withdraw the TCs into the wall. In this manner, we can protect the TCs from slag or other erosion damage [43]. The actual temperature measured is closer to that of the refractory than that of the reactor core, and thus is highly dependent on the extent of the depth of withdrawal from the reactor space.

1.2.2 Indirect Measurements

Several reports describe how secondary measurements that are relatively easy to obtain—such as temperatures, pressures, and compositions of streams into and out of a gasifier—can be used in conjunction with empirical or theoretical models and correlations to estimate inaccessible operating parameters inside the reaction zone. The advantage of indirect measurement is that sensors are usually located at the downstream of the gasifier, which would be away from the extreme environment of the gasifier. For example, Higman and van der Burgt [43] conclude that the temperature of a dry slurry feed gasifier can be monitored by measuring the concentration of CH_4 or CO_2 in the product gas. In fact, it was reported that this approach was used to estimate gasification temperature during the Tampa Electric Integrated Gasification Combined-Cycle Demonstration Project [6], [44] and is believed to be in common use by at least some operators of gasification

units in the United States. An attempt to correlate a large number of routinely measured process variables to the composition of the produced syngas was also reported [39]. Texaco Inc. [17] has developed an apparatus that monitors the weight of slag as it accumulates and subsequently as it flows form the gasification chamber during a deslagging operation. The resulting data were fed into a preprogrammed computer to evaluate the gasifier operation conditions, including temperature. The evaluation results will cause the fuel composition and its rate of feed to be automatically adjusted by the computer program. Computational study by Sarigul [90] showed close correlation between CH_4 concentration and the adiabatic flame temperature of the gasifier. The same approach is used at Eastman; in fact, the gasifier operators routinely report temperature inside the reactor in ppm of methane. The advantage of this method is that it gives an integral measurement of the temperature at the reactor outlet. However, it does not give an indication about local hot spots. Moreover, the measurement has a certain time delay for real-time monitors.

A heat flux measurement is comprised of an installation of a small piece of membrane wall in the wall of the refractory and measurement of the increase in water temperature of a known amount of water flowing through the membrane wall. Its response time is relatively slow, usually 10–30 seconds, indicating the local average temperature [65], [85], [97].

Despite limited current use, the inferential sensors remain a promising approach in gasification applications, with further advantages of relatively small investments and retrofit requirements for their deployment. However, two fundamental limitations of inferential measurements must be taken into account. First, the quality of inferences critically depends on modeling errors and uncertainties, and unmodeled changes to the process itself (e.g., due to ware and aging), its feed, and unknown process disturbances. Second, the measurement accuracy, sensitivity, and response time of inferential measurement compare poorly with the corresponding characteristics of the direct measurements. Therefore, the direct measurements in gasification will continue to be desirable despite a long development time, high development cost, and technical challenges that must be

overcome.

1.2.3 Noninvasive Measurements

An alternative technique to obtain direct measurements of gasification temperature is using methods that do not require the direct or partial insertion of a fragile sensing element into the harsh environment. The most widely used techniques in this category are optical measurements, used for combustion-specific measurements of temperatures and reaction composition [87]. Typical fiber optic sensors include those based upon optical reflection, scattering, interference, absorption, fluorescence, and thermally generated radiation [26]. Optical pyrometry [72] is a practical method for measuring temperatures of flames if the blackbody radiation emissitivity factor is constant or calibratable. Texaco Inc. [62] used an optical pyrometer in its pilot unit for several years. However, conventional total radiation or single-wavelength pyrometers cannot provide accurate measurement of the flame temperature because of the unknown or nonuniform emissivity of the flame. In addition, the background radiation can interfere the measurement. Two-color pyrometry removes the emissivity limitation by using the ratio of irradiances at two carefully selected wavelengths, which has been used from flame in utility furnaces to various open flames, such as premixed and diffusion flames [66]. The multicolour method has also been developed over recent years. Most existing optical pyrometries can only provide a measurement of average temperature of a single-point or a small area defined by the field of view of the probe. The 3D temperature profile can be reconstructed based on a collected 2D flame temperature image transformed from the color flame images [113].

Though minimally invasive (requiring a transparent access port), optical techniques are not suitable for temperature and composition measurements when an optically transparent line-of-sight is difficult or impossible to maintain, as in the case of slagging gasification or when high particle concentration in the reaction zone prevents light transmission. The ash and slag would block optical access ports. Continuously blow nitrogen gas is required to keep the pores open, which make it expensive and results in a loss of reading very frequently. Therefore, any

commercialization of optical pyrometry is likely to be in addition to rather than as a replacement of thermocouples.

Various optical-based methods have also been studied for extreme temperature measurements [60], including an optical fiber bragg grating (FBG) sensor, optical resonator cavity sensor, optical sapphire fiber-based fluorescence sensor, optical single crystal sapphire-based sensor, etc. Photosensitive FBG sensors and optical resonator cavity sensors, such as Fabry-Perot cavity-based sensor, are both silica fiber based, which cannot survive temperatures over 1000°C because of material limitations.

In long-term thermal tests of FBGs at temperatures close to or above 1000°C in air for hundreds of hours, unpackaged standard silica single mode fibers lost almost all of their mechanical strength. It is certain that silica fibers experience severe mechanical degradation in the oxidizing atmosphere at high temperature. The silica fibers become extremely brittle and any subsequent handling of the fiber is not possible after the test [38].

Single crystal sapphire fiber or bulk is a more successful sensing element used for extreme temperature sensing applications that have a melting temperature ~ 2050°C [37]. Most sapphire fiber sensors are based on Fabry-Perot structures within the fiber generating broad-band interference fringe pattern that can be monitored as a function of temperature [102]. Sapphire-based sensors have been fabricated and demonstrated for high-temperature measurements in laboratory tests [93], [112]. These sensors will still have to survive the difficult reactor environment, and the fundamental uncertainties of temperature measurement in a gasifier will remain [78]. A well-controlled dopant density is important for accurate measurement performance, which puts strict requirements on its fabrication process and increases the cost. It has been difficult to achieve high-quality measurement results, since the interference signal from the fabry-perot cavity are degraded by the multimode electromagnetic fields in multimode sapphire fibers. These systems during industrial service are prone to mechanical failure due to CTE mismatch between optical fibers and sensing elements.

1.3 Organization

The research of this dissertation illustrates that the development of a novel noninvasive technique using ultrasound measurements of segmental temperature distribution (US-MSTD) method can potentially offer excellent resolution for solving challenging direct temperature distribution monitoring problems on coal and biomass gasifiers.

Chapter 2 will discuss the fundamental physical basis of temperature measurement based on ultrasound methods, and the essential concept of ultrasound measurements of a segmental temperature distribution system. Chapter 3 will demonstrate the development of an ultrasound system for low temperature measurements with cementitious waveguide. In Chapter 4 of this dissertation, the ultrasound system using engineered alumina waveguide for laboratory-scale high temperature tests will be discussed. Chapter 5 will describe a robust signal processing method based on the combination of cross-correlation of envelope of waveform and anisotropic diffusion methods. The validation of the developed US-MSTD system in a pilot-scale downflow oxyfuel combustor will be presented in Chapter 6. Chapter 7 provides improvement of the hybrid US system on waveguide material selections. Finally, the conclusion of this research and possibly future research on this topic will be given in Chapter 8. Chapter 2 and 3 correspond to paper [51], Chapter 5 corresponds to paper [52].

CHAPTER 2

NONINVASIVE ULTRASOUND MEASUREMENTS OF SEGMENTAL TEMPERATURE DISTRIBUTION[1]

2.1 Ultrasound

Ultrasound (US), because of its high sensitivity, high penetrating power, fast time response, great accuracy, and noninvasive operation, has become a potential approach for noninvasive temperature measurement. It became a subject of interest to researchers during World War I, but its use in industry did not grow to proportions worthy of note until World War II. Traditional ultrasonic applications have been used almost exclusively for nondestructive testing (NDT), such as macroscopic flaw detection/evaluation and dimensional measurements; material characterization, such as microstructures and associated mechanical properties assessment [89]. Development and perfection of ultrasonic nondestructive evaluation techniques are capable of monitoring and controlling the material's production process; the material's stability during transport, storage, and fabrication; and the rate of degradation during the material's in-service life [36]. The application of ultrasound in medicine began in the 1950s, and includes diagnosis, commonly called sonography, and therapy [18], [63]. Sonography is used for evaluating the condition of internal organs and tissues, commonly for neonatal fetuses, heart imaging, and blood flow measurement. Therapy is provided by high intensity waves which heat tissues to provide massage treatment or break stones [30], [73].

---

[1]This chapter is adapted with permission from (Jia, Yunlu, et al. "Ultrasound Measurements of Temperature Profile Across Gasifier Refractories: Method and Initial Validation." Energy & Fuels 27.8 (2013): 4270-4277.). Copyright (2013) American Chemical Society

Ultrasound works with vibratory waves at frequencies above those within the hearing range of the average person at frequencies above 20 kHz. Ultrasonic waves are stress waves. Therefore, they can exist only within substance, such as gases, liquids, and solids [29]. The behavior of ultrasound propagation is given as [98]

$$y(x,t) = y_0 \cos\left(\omega t - \frac{2\pi x}{\lambda}\right), \tag{2.1}$$

where y is the particle displacement of the propagating sound wave with respect to distance, x, and time, t, y_0 is the amplitude of the wave, ω is the angular wave frequency, and λ is the wavelength. ω and λ are constants defined by the medium in which the sound is traveling, which are defined as

$$c = f \cdot \lambda, \tag{2.2}$$

$$\omega = 2\pi f, \tag{2.3}$$

where c is the ultrasound propagating speed (the speed of sound, SOS) within an elastic medium and f is the frequency.

2.1.1 Basic Instrumentation

Figure 2.1 shows a block diagram of a basic ultrasonic measurement system used to generate and detect ultrasonic waves in a solid specimen. The synchronization generator gives trigger signals with high repetition rate to the pulser. The pulser provides electrical voltage to the transducer so that the transducer excites ultrasonic

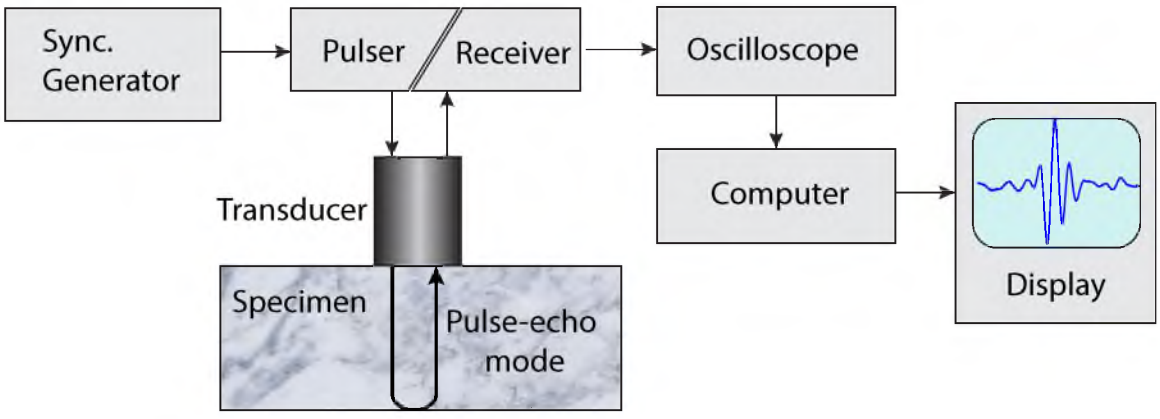

Figure 2.1: Block diagram of basic components of an ultrasonic measurement system to generate and detect ultrasonic waves.

waves at the same repetition rate. The reflected ultrasonic waves through the specimen are received by the same transducer (called pulser-echo mode) and the resulting voltage of the received signal goes to the display through oscilloscope. The computer is used to collect and analyze the acquired ultrasonic waveforms.

2.1.2 Ultrasound Propagation Speed

Considering a sample of a solid material with known thickness L maintained at a uniform temperature, assuming a pulse-echo method (transducer/receiver is the same device), by measuring the time it takes an ultrasonic signal to travel the distance L, the so-called the time of flight (TOF), the speed of sound may be calculated as

$$c = \frac{2L}{t_{of}}. \tag{2.4}$$

The speed of sound and its propagation mode are directly dependent on the physical composition of the transmitting medium. In solids, the SOS depends upon the type of pulse wave, the elastic properties, the density of the medium, and the frequency in some cases [23]. The ratio of applied stress (force/area) to axial strain (extension/length) is called the elastic modulus, or Young's modulus. A piezoelectric transducer can generate both longitudinal/compression, also known as primary wave/p-wave, and shear waves (s-wave), but one type of mode will be dominant depending on the particular transducer's piezoelectric properties.

The relationship between longitudinal SOS and the elastic modulus in an isotropic solid, in which the particle motion is parallel to the axis of the ultrasound propagation, is given by

$$c_{longitudinal} = \sqrt{\frac{K + \frac{4}{3}G}{\rho}} = \sqrt{\frac{E(1-\nu)}{\rho(1+\nu)(1-2\nu)}}. \tag{2.5}$$

When the particle motion in the wave is normal to the direction of propagation, the relationship results in the following equation for shear SOS

$$c_{shear} = \sqrt{\frac{G}{\rho}}, \tag{2.6}$$

where K and G are the bulk modulus and shear modulus of the elastic materials, respectively. E is the Young's modulus, ρ is the density, and ν is the Poisson's

ratio, while Young's modulus and Poisson's ratio have a relationship of $E = 3K(1 - 2\nu)$. The SOS of longitudinal waves depends both on the compression and shear resistance properties of the material, while the speed of shear waves depends on the shear properties only.

For a long, thin rod, where its diameter is much smaller than its length, the SOS of longitudinal waves may be simplified and given by:

$$c_{rod} = \sqrt{\frac{E}{\rho}}. \tag{2.7}$$

Liquids and gases cannot resist shear stresses. The SOS in fluids is expressed as

$$c_{liquid} = \sqrt{\frac{K}{\rho}} = \sqrt{\frac{1}{\beta\rho}}, \tag{2.8}$$

where $\beta = 1/K$ is the compressibility of liquid. For an "ideal gas," the SOS can be shown to be

$$c_{gas} = \sqrt{\frac{\gamma P}{\rho}} = \sqrt{\gamma RT}, \tag{2.9}$$

where γ is the adiabatic index, which is the ratio of specific heats of a gas at a constant-pressure to a gas at a constant-volume(C_p/C_v), P is the ambient pressure, and R is the molar gas constant.

Young's modulus of elasticity is sensitive to most of the common microstructural evolutions and damage (microcracking, densification, phase transition, etc.). The quantitative assessment of microstructural changes can be carried out through the measurement of ultrasound properties.

2.1.3 Impedance and Attenuation

Acoustic impedance, another major characteristic to describe ultrasonic properties of material, is the quantification of the resistance of ultrasound propagation in a medium [22], [55]

$$Z = \rho \cdot c. \tag{2.10}$$

An ultrasound propagating through a material has its acoustic energy loss. The reduction in the amplitude of a ultrasonic waveform is attenuation [55], [63],

expressed as the logarithm of the ratio of the magnitudes of the original to the attenuated pressure amplitudes, a and a_0, measured in decibels (dB):

$$A(dB) = 20log_{10}(\frac{a}{a_0}). \tag{2.11}$$

Two types of process affect the attenuation of ultrasound propagating waveform, which involve material responses and wave interaction. Material repose processes include geometric attenuation, such as beam spreading or focusing, energy absorption, dispersion, and nonlinearity. Transmission across interfaces, scattering by material variation, inhomogeneities of grains, grain boundaries, pores, and more, and the Doppler effect are three main aspects of wave interaction processes that cause acoustic attenuation and defects [14], [74].

Scattering is the primary mechanism by which ultrasonic energy is lost during propagation, which also affects the feasibility and effectiveness of engineered waveguides used for proposed temperature measurement. Scattering is the redirection of an ultrasonic wave, as a result of the interaction between a primary ultrasonic propagating wave and the anisotropic grains (inhomogeneities) inside of the medium [58]. If their physical properties such as density or elasticity are different from those of the surrounding medium, it causes a discontinuity in ultrasound propagating speed at each grain boundary, which leads to the reflection at the grain boundaries denoted by scattered wave and energy loss. The magnitude of scattering depends on the particles per volume, size, acoustic impedance, and frequency [41]. A scattering is created at a single grain if the dimensions of the heterogeneities are smaller than the wavelength, as $D <= \lambda$, where $\lambda = c/f$, f is ultrasound propagating central frequency. This scattering problem of sound was first solved by Lord Rayleigh and is therefore called Rayleigh scattering [84]. There are a number of causes of ultrasonic energy loss in solids, and Rayleigh scattering is one of the main reasons [13]. The process of energy loss usually refers to the changes of ultrasonic energy into heat. The presence of microscopic structural defects, such as point defects and dislocations and macroscopic defects, affects the degree of hardness and the elastic properties of the material and gives rise to absorption that occurs in both metals and nonmetals.

2.1.4 Reflection and Transmission

When an ultrasonic wave encounters an interface, several phenomena may occur, including reflection, transmission, refraction, and mode conversion. These interactions are the phenomena upon which our proposed ultrasound method relies.

Ultrasonic waves are reflected at the interface of two media if there is a difference in acoustic impedances (Z) of the materials on each side of the interface. This difference in Z is commonly referred to as the impedance mismatch [29]. Assuming the incident is normal to the interface, the fraction of the incident wave intensity that is reflected can be derived because particle velocity and local particle pressures must be continuous across the boundary, which is calculated from the acoustic impedances of the materials on both sides of the interface:

$$Re = \left(\frac{z_2 - z_1}{z_2 + z_1}\right)^2, \tag{2.12}$$

where z_1 and z_2 are acoustic impedances of media 1 and 2. The value produced by Equation 2.12 is known as the reflection coefficient, while the transmission coefficient is calculated by

$$Tr = \frac{4z_1 z_2}{(z_2 + z_1)^2}, \tag{2.13}$$

or from $Re + Tr = 1$.

The reflection and transmission coefficients represent the percentage of acoustic energy which is either reflected or transmitted at a boundary. The greater the impedance mismatch, the greater the percentage of energy that will be reflected at the interface. In addition, the preceding equations for reflection and transmission apply to ideal interfaces that have no thickness.

2.2 Physical Basis of the US-MSTD Method

The physical basis of the proposed noninvasive ultrasound approach for temperature measurement is temperature dependence of the speed of sound in gas, liquid, and solid:

$$c = f(T). \tag{2.14}$$

If relationship 2.14 is known, either from theoretical considerations or empirical correlations, the measured t_{of} can be used to obtain the uniform temperature of material of interest as:

$$T = f^{-1}\left(\frac{2L}{t_{of}}\right), \tag{2.15}$$

assuming that the inversion of 2.14 is unique. In addition to the TOF measurements emphasized in this research, other ultrasonic characteristics, such as a phase change of echoes produced by a tone burst excitation, may be used to define temperature-dependent variations in the SOS [67].

The application of this idea to measure the temperature in gases is known as acoustic pyrometry and is well established [34], [53] and commercially used in many high-temperature applications, such as the cement industry, combustion, and incineration industries [15], [57], [106]. The advantage of the approach is the ability to obtain real-time temperature measurements over an extremely large range of temperatures (from 0 to 3500 °F), which makes it applicable to process monitoring from a cold start up to normal high-temperature operation. Disadvantages include significant measurement uncertainties when temperature along the propagation path between the transducer and the receiver varies significantly and unknown changes in the adiabatic constant due to variability in the gas composition. The utilized acoustic frequency range is low (typically, ≤3kHz) because higher frequency ultrasound does not propagate well through gases. The consequence of low excitation frequencies is interference from combustion instabilities, sounds produced by a turbulent flow, and other disturbances, collectively known as a passive acoustic signature. Such low frequencies also limit the achievable spatial resolution of measurements when multiple transducers-receivers are used in order to measure the temperature distribution inside of a containment [48]. In addition, acoustic thermometry has been used to detect temperature changes in the ocean by receiving low-frequency ultrasound (< 100 kHz) transmitted across an ocean basin [31].

Ultrasonic method offers a powerful noninvasive or minimally invasive alternative for temperature measurement in solids. However, very little work has been

done in this area. Techniques like this are particularly useful for applications such as when:

a) insertion of temperature probes is undesirable, difficult, or impossible;

b) extreme environments affect longevity of conventional sensors, as is the case for many energy conversion processes; and

c) optical line-of-sight measurements are not practical because the medium is opaque or optically dissipative.

The dependence of the speed of sound on the temperature, $c = f(T)$, obtained experimentally or theoretically, would then allow us to estimate the temperature of the sample. Several notable examples using acoustic thermometry to measure temperature have been shown in microelectronic and medical applications. Most conventional ultrasonic remote temperature sensing methods rely on an assumption of constant temperature along the propagation path in the solid. Lee et al. [61] reported the development of an acoustical temperature measurement system which uses the TOF measurements of an acoustic wave introduced into the wafer through an excitation quartz rod. The wave, partially reflected from the quartz-silicon interface, travels through the wafer until reaching a second quartz rod through which the wave reaches the receiver. The difference between an arrival time of the reflected wave and the wave reaching the receiver through the second rod gives the time of flight through the wafer, which is used to estimate the wafer temperature. Lee et al. reported that $\pm$ 5°C accuracy was achieved in the range from room temperature to 1000°C (with a proposed use up to approximately 1800°C [2]). Arthur et al. [1] investigated the use of backscattered ultrasound energy in temperature measurements to monitor and control noninvasive thermal therapies of tumors. Using a 7 MHz linear ultrasound phased array transducer, they demonstrated temperature measurements in ex vivo phantom tissue from 37 to 50°C in 0.5°C steps. The project did not progress towards in vivo testing because the quality of temperature measurements was severely affected by subject motion, unavoidable in subjects due to breathing and other disturbance. Simon et al. [94] developed a 2D temperature estimation method based on the detection of shifts in echo location of the backscattered ultrasound from a tissue undergoing thermal

therapy. They suggested that 0.5°C accuracy is possible. Another example of high-temperature application of the US method is in metallurgy. Balasubramaniam et al. [3] used an ultrasonic sensor to measure viscosity and temperature of molten material up to 1000°C with the temperature resolution of 5°C.

However, when temperature distribution of the sample $T(z)$ along the propagation path is nonuniform, the overall TOF depends on the temperature in a complex and unknown way

$$t_{of} = 2\int_0^L \frac{1}{f(T(z))}dz \tag{2.16}$$

and there are many arbitrary temperature distributions $T(z)$ that will result in the estimated TOF matching the measured value.

The lack of unique dependence of the measured t_{of} on the temperature distribution may be resolved by adding constraints on the feasible solution so that an estimation of fixed temperature distribution based on TOF measurements in the integral form (2.16) becomes possible. The first approach is to have the problem regularized by imposing additional constraints on the temperature distribution. This has an effect of parameterizing the "admissible" temperature distribution by prescribing a functional form that depends on one or more unknown parameters, which are then found from ultrasound and, perhaps, other unrelated measurements. Parameterizations may include an assumption that the temperature along the US propagation is constant and given by Equation 2.15; the temperature distribution is linear with the slope and intercept found from t_{of} and at least one additional independent measurement; and the requirement that $T(z)$ satisfies a heat transfer model with appropriately selected parameters (such as thermal conductivity) and boundary conditions. In the case of the linear parametrization, a slope and intercept are needed to determine the parameterization. However, both parameters cannot be determined from a single measurement of t_{of}. At least one additional measurement, such as the thermocouple measurement of the temperature at the location of the transducer, is required to determine both unknowns.

If assumption of a constant temperature T_a is used across the ultrasound propagation path, 2.15 calculated from using the measurement of t_{of} may only

the suitable for small temperature gradient cases. The relationship between the calculated average T_a and the unknown temperature distribution $T(z)$ is given by the following equation:

$$\int_0^L \frac{1}{f(T(z))} dz = \frac{L}{f(T_a)}. \tag{2.17}$$

When strong thermal gradients are present, using Equation 2.17 to approximate the temperature distribution across the containment of extreme environments, such as refractories of the gasifier and other energy conversion processes, would result in less accurate temperature estimation.

The TOF measurements alone are not sufficient to reconstruct the parameterized temperature distribution with more than a single unknown. Reducing the number of unknowns for temperature distribution determination is to devise an approach that provides more data than a single measurement of the TOF. This can be achieved by using multiple transducers and receivers to measure transmit and echo delay times along different ultrasound propagation paths, followed by the simultaneous interpretation of the measurements to reconstruct the temperature distribution (e.g., [35], [48], [80]). This approach shares common features with X-ray computer tomography, which reconstructs the density (attenuation) distribution inside the sample and other noninvasive measurement modalities in which the acquired data depend on the spatial integral of the property of interest [111].

Model-based temperature estimation using TOF measurements is another approach and is found the most in literature. Takahashi and Ihara [47], [96] tested a 30 mm steel plate, with a single side heated at 300°C and 700°C at steady state. The temperature at the transducer location was independently measured. A linear relationship between SOS and the temperature 2.14 was assumed. In addition, they assumed a 1D heat transfer model for temperature estimation along the length of ultrasound propagation direction. Thus, the hot face temperature was assumed to predict the temperature distribution $T(z)$ along the propagation path and the corresponding model prediction of the TOF from the model. The unknown distal temperature was then estimated as the value that minimizes the difference between the TOF predication given by Equation 2.16 and its measured value. An approach developed by Schmidt et al. [91] also uses a 1D heat transport model to obtain

$T(z)$, but it adjusts a different single parameter, the boundary heat flux at the distal end of the ultrasound propagation path, to match the measured and the predicted values of t_{of}.

Heyman et al. [42] invented their dynamic acoustic thermometer to measure the temperature at a remote location by relating the measured change in integrated acoustic delay to the remote location temperature with a combined 1D thermal-acoustic model. The integrated acoustic delay is determined from the measurements of phase change between points of interest and reference location, at which a constant frequency is applied. The combined model relates temperature to acoustic propagation speed of sound along the path. The experiment of measuring steel rod temperature using this system in a nonstirring water tank showed a temperature resolution of better than 6 μK at room temperature and a 110 μK resolution for a 60 rpm magnetic stirring test. The experiments also showed a faster response to the thermal energy change, long before the thermal wave had propagated from the heat source to the sensor location. Yuhas et al. [108] designed an apparatus for determining local temperatures of inaccessible surface heat fluxes based on measured propagation time using ultrasound pulse-echo mode. They also used 1D thermal model approach and assumed that the dependence of SOS on temperature is linear. The temperature at the point of interest may be not calculated to estimate its heat flux as a step-wise constant function of time. The relationship between SOS and temperature was calibrated with known constant heat flux. The verification experiment was carried with a naval ship gun barrel Mark 45 Navel Gun with thickness of 0.0635 m during a firing regimen using three assumed heat flux profiles. Their tests showed that the estimated maximum heat flux is underestimated by no more than 6%, but the maximum measured temperature has an over 150°C error.

The third distinct approach is to devise ways to extract more information from the response of each ultrasound transducer-receiver other than a single time of flight measurement. This is possible if the ultrasound pulse produces multiple ultrasound reflections, caused by echogenic features encountered as the excitation propagates through a waveguide, which has been presented in optical fiber Bragg

grating to measure temperature [83]. Hanscombe and Richardson in Schlumberger [40] proposed a method in which an ultrasound waveguide is engineered to have a number of randomly spaced notches formed by arbitrary grating length. The dominant frequency reflected at each notch is different, which is determined by grating dimensions, which would change due to temperature changes through thermal expansion. Multiple frequency-separated echoes propagate along the waveguide; the cross-talk between overlapping echoes is reduced and causes the SOS of the waves within the notches to change because the temperature variations are encoded by the changes in echoes' frequency content. The described innovative approach apparently has not been tested in experiments, leaving many unanswered questions. For example, it is not clear how long each grated zone should be to ensure narrow frequency content of each echo. The achievable accuracy as a function of grating design remains unknown. Furthermore, the accuracy of temperature measurements when thermal gradients are present within each grated zone, leading to a wider frequency band of each echo, has not been quantified.

2.3 Method

Our proposed ultrasound measurements of the segmental temperature distribution method are shown in Figure 2.2. The overall system for measuring temperature distribution across refractory and other aggressive process containments consists of:

(a) the engineered ultrasound propagation path with echogenic features creating partial reflections from known locations, either embedded as an insert or incorporated into the refractory to provide partial ultrasound reflections;

(b) an ultrasound transducer and receiver, which can be implemented as single or distinct components ;

(c) the analog and digital ultrasound instrumentation used to generate the excitation pulse and then acquire and amplify the return echoes;

(d) the signal processing system that accurately determines the TOF for each echo and then uses this information to calculate the SOS or its change in the corresponding segment of the refractory;

(e) the relationship between the SOS and the temperature; and

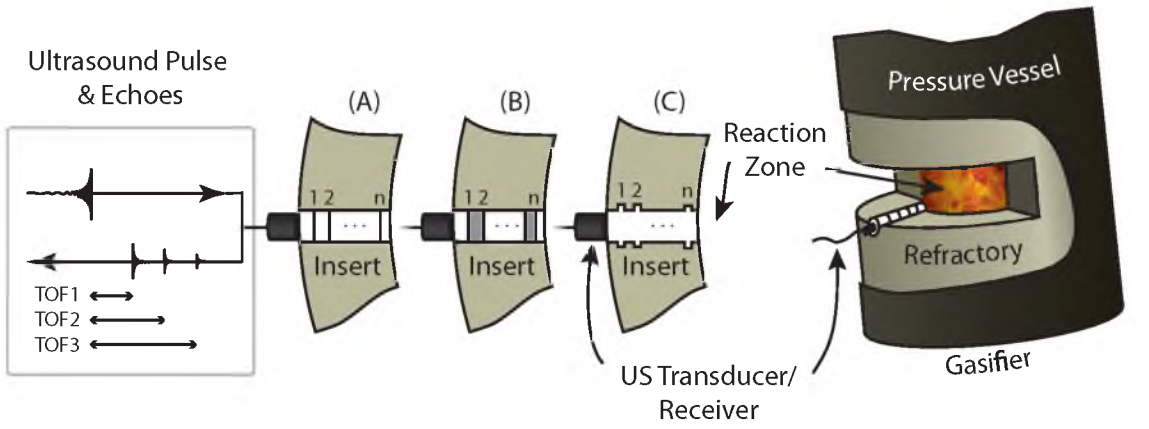

Figure 2.2: Ultrasound measurements of temperature distribution in the refractory. (A) Refractory material contains embedded planes of scattering material. (B) Layered refractory. (C) Refractory insert with geometric changes in the ultrasound propagation path creates partial back scattering. *Left panel* shows an ultrasound excitation pulse and the train of partial echoes produced by internal partial ultrasound reflectors. *Right panel* illustrates an engineered ultrasound waveguide/insert — with internal back scatterers, layers structure, or geometrical changes — embedded into the gasifier refractory.

(f) the method to translate the segmental SOS into the temperature distribution such that the predicted TOF, according to Equation 2.16, matches the measurement values. Each of the components will be discussed in more detail in the following chapters.

In the described approach, the sensitive electronic components are kept away from harsh gasification environments and it is only required that the US transducer be acoustically coupled to the cold side of the refractory, representing minimal modifications to the gasifier.

2.3.1 Structure US Propagation Path

The central idea of the US-MSTD method is to create an ultrasound propagation path inside the refractory (or material of interest) which incorporates partial ultrasound reflectors (back scatters) at known locations that redirect a portion of US energy of the excitation pulse back to the transducer as multiple echoes.

Figure 2.2 illustrates three different alternatives to creating such ultrasound backscattering. In this illustration, it is assumed that the same element serves as a transducer and receiver; modification for the case of a separate transducer and

receiver and an angled US beam are straightforward. In Figure 2.2(A), partial US reflections are created by planes of scattering material embedded into the refractory. The second option is depicted in Figure 2.2(B), where the refractory material is layered, with slightly different acoustical impedance in each layer. Figure 2.2(C) shows an embodiment in which partial reflections are created by geometric changes in the US propagation path through an embedded refractory insert. Such an insert can have a geometry (e.g., as shown in Figure 2.2(C)), designed to produce distinct US reflections at predetermined spatial positions, or layered properties, as in the case of Figure 2.2(A) and 2.2(B). Separately produced inserts can be introduced into the refractory during its replacement, service, or relining, as illustrated in the right panel of Figure 2.2.

2.3.2 Acquisition of Echo Waveforms

A measurement of the temperature distribution begins with a US pulse, generated by an ultrasound transducer. This pulse will be partially reflected from each scatterer in the insert and return to the receiver as a train of partial echoes at time $TOF1$, $TOF2$, $TOF3$, ..., as shown conceptually in Figure 2.2 (left panel).

The time of flight $t_{of}^{z_i}$ of the echo produced by a feature located at z_i is equal to

$$t_{of}^{z_i} = 2\int_0^{z_i} \frac{1}{f(T(z))} dz. \tag{2.18}$$

The temperature distribution in the i-th segment of the propagation path is inferred from the difference in the time of flight, t_{of_i}, between consecutive echoes produced by echogenic features which bound the segment at locations z_{i-1} and z_i:

$$t_{of_i} = t_{of}^{z_i} - t_{of}^{z_{i-1}} = 2\int_{z_{i-1}}^{z_i} \frac{1}{f(T(z))} dz, \tag{2.19}$$

where $(z_i - z_{i-1})$ is the segment's length. The TOF of the first echo gives an indication on the temperatures in the 1st zone of the refractory, between the cold surface and the first scatterer based on information specific to the temperature distribution with that segment. The next return echo will originate from the second scatterer. By subtracting the TOF of the second and the first echoes, the temperatures between Scatterers 1 and 2 can be estimated, and so on until the estimate of the temperature

distribution throughout the refractory is obtained. With that distribution known, the last echo, reflected from the refractory-reactor zone surface, can be used to determine the temperature of the refractory's interior hot surface. The first segment between the transducer and the first scatterer is often used as a delay line and references the time of flight of all subsequent echoes to the arrival time of the first echo. Then the difference in the TOF between the second and the first echoes gives the information on the temperature distribution in the second segment, and so on.

2.3.3 Signal Processing

Since the speed of sound is calculated as the distance traveled by an ultrasound pulse divided by the time of propagation (or time of flight, TOF), a method for precise measurements of the time of flight is essential to accurate measurements of temperature distribution. The simplest approach to the measurements of the TOF and its changes is to use temporal location of a single-point waveform feature, such as the first zero crossing or the peak value of the waveform. Though standard, these timing techniques are sensitive to measurement noises. Furthermore, when broad-band excitations are used, the timing accuracy of single-feature methods deteriorates further due to waveform distortions and broadening caused by stronger attenuation of higher-frequency content of ultrasound pulses.

More robust and accurate measurements of t_{of} and t_{of_i} may be achieved when the entire shape of the waveform is utilized in timing. In this case, both amplitude and phase information are taken into account [45], which makes timing results less sensitive to measurement noises and shape distortions. Mathematically, the cross-correlation between two signal $f(t)$ and $g(t)$ is represented as:

$$\varphi_{fg} = f \star g(\tau) = \int_{-\infty}^{+\infty} f^*(t)g(t+\tau)dt, \tag{2.20}$$

where f^* is the complex conjugate of f and τ is the lag time between two signals. The temporal shift τ needed to obtain the best match between the waveforms may be found by maximizing their cross-correlation φ_{fg} [24], minimizing l_1 and l_2 norms of their difference [50], [75], [101], or by maximum likelihood [20]. Figure 2.3 shows that ΔTOF between two echoes is obtained by finding the best match of the entire normalized shape of the two waveforms as based on both phase and

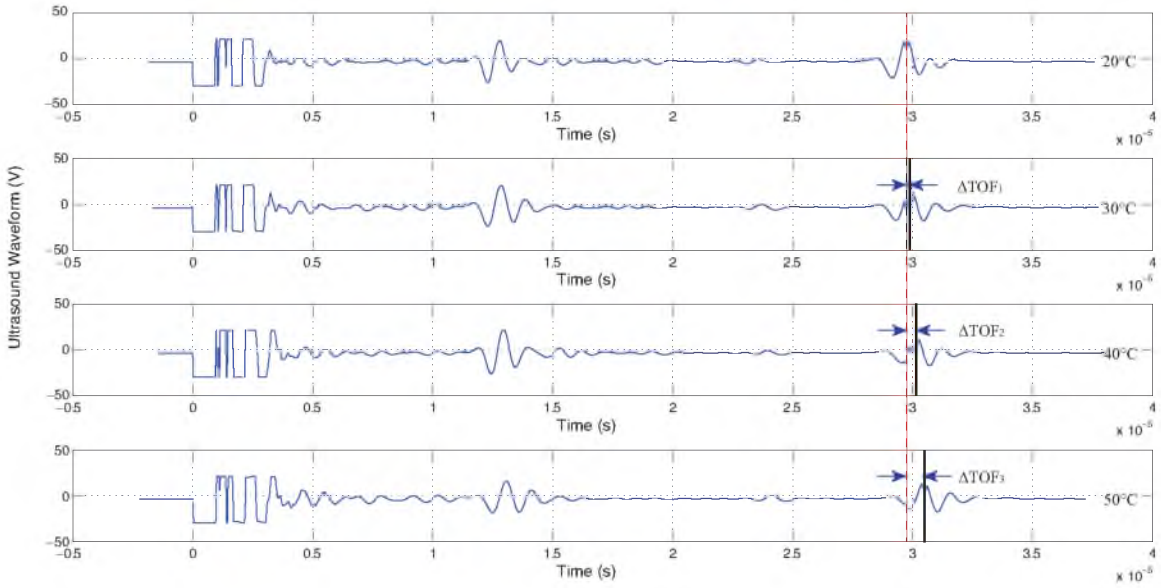

Figure 2.3: The ΔTOF between echo waveforms at different temperatures is calculated by cross-correlation with a reference waveform acquired at 20°C.

amplitude information, which makes timing results less sensitive to noises and shape distortions.

Though cross-correlation and other shape-matching methods perform better than single-point timing, the results may still be unacceptable when significant distortion of ultrasound waveforms occurs, as is often the case when the pulse propagates through attenuating and dissipative materials. It was suggested by Le [59] that for waveform distorting samples, a higher precision can be achieved if the envelopes of the waveforms are used in timing. The analytic signal, $s_a(t)$, of the waveform, $s(t)$, is the following complex function:

$$s_a(t) = s(t) + j\hat{s}(t), \tag{2.21}$$

where $j^2 = -1$ and $\hat{s}(t)$ is the Hilbert transform of $s(t)$:

$$\hat{s}(t) = -\frac{1}{\pi}\lim_{\varepsilon\to 0}\int_{\varepsilon}^{\infty}\frac{s(t+\tau)-s(t-\tau)}{\tau}d\tau. \tag{2.22}$$

The envelope of the waveform $s(t)$ is then calculated at the amplitude of its analytic signal:

$$A(t) = |s_a(t)| = \sqrt{s^2(t)+\hat{s}^2(t)}. \tag{2.23}$$

We have found [52] that further improvements in timing accuracy can be achieved by iteratively applying a nonlinear anisotropic diffusion filter to the envelopes of the echo waveforms, which will be discussed in a later chapter.

2.3.4 Temperature Dependence of the Ultrasound TOF

The unknown temperature distribution is estimated from the measurements of the time of fight of ultrasound echoes. The SOS and length of the propagation path both change with the temperature of the waveguide and thus affect the echoes' TOF. It is possible to separate their contributions to the changes in the TOF. However, as long as the calibration curve 2.14 is obtained without differentiating between the two phenomena, there is no practical need to distinguish the contribution of each one. The subsequent discussion assumes that the correlation between the SOS vs. temperature, Equation 2.14, was not corrected for the thermal expansion. This simplifies the method, as it becomes unnecessary to adjust the length of the propagation path in Equations 2.16 and 2.18 for the thermal expansion.

2.3.5 The Temperature Distribution Estimation

The measurements of the segmental time of flight t_{of_i} encode the information on the temperature distribution within i-th segment. As before, additional assumptions are needed to estimate the segmental temperature distribution from the measurement model 2.18. All parametrization options discussed in the context of deconvoluting model Equation 2.16 may be used for this purpose, and are discussed below.

2.3.5.1 Piecewise Constant Distribution

This distribution is obtained by assuming constant speed of sound within each segment. Using this assumption in Equation 2.18, the constant SOS in the i-th segment of the waveguide is obtained as

$$c_i = \frac{2(z_i - z_{i-1})}{t_{of_i}}, \tag{2.24}$$

and the corresponding constant temperature is obtained by inverting the correlation 2.14. After repeating the process for all segments, the entire temperature distribution along the waveguide is approximated as a piecewise constant function. The

infeasible temperature discontinuity at the locations of the echogenic features is an undesirable feature of such approximation. By using a larger number of echogenic features and the correspondently finer segmentation, this approximation can be further improved.

2.3.5.2 Piecewise Linear Distribution

Assuming that the temperature changes linearly within each segment significantly enforce temperature continuity. For a segmental sample with several echogenic features, the temperature at the transducer location, $z = 0$, is measured independently and equal to $T(0) = n_1$. By using the measured TOF of the first echo and the linear temperature distribution in Equation 2.19, the following equation is obtained

$$t_{of_1} = 2\int_{z_1}^{z_2} \frac{1}{f(m_1 z + n_1)} dz, \tag{2.25}$$

from which the unknown slope of the distribution, m_1, can be found. Similarly for the i-th segment, the unknown slope m_i and intercept n_i are obtained from the solution of the following two equations:

$$t_{of_i} = 2\int_{z_{i-1}}^{z_i} \frac{1}{f(m_i z + n_i)} dz \tag{2.26}$$

and

$$n_i = (m_{i-1} - m_i) z_{i-1} + n_{i-1}, \tag{2.27}$$

where t_{of_i} is the difference in the TOF of the i and $i-1$ echoes, and Equation 2.27 enforces the continuity of the temperature at $z = z_{i-1}$. The process continues for all remaining segments until the piecewise linear approximation of the temperature distribution over the entire sample is obtained.

2.3.6 Estimation of Heat Flux

The measurement of conductive heat fluxes through a solid is commonly obtained by attaching a flux sensor to the surface to the sample. It is therefore capable of estimating only a localized heat flux in the immediate proximity of the flux sensor. The approach proposed in this dissertation can be used to profile the temperature distribution over a significant distance away form the surface.

Thus, it can be used to noninvasively profile conductive heat fluxes through the sample, at a considerable distance from its surface. Specifically, by differentiating the estimated temperature distribution $T(z)$, the conductive heat flux, q, across the sample is estimated as:

$$q(z) = -k\frac{dT}{dz}. \tag{2.28}$$

For the case of piecewise constant temperature profile,

$$\frac{dT}{dz} \approx \frac{T_i - T_{i-1}}{z_i - z_{i-1}}. \tag{2.29}$$

The piecewise linear temperature distribution will result in a piecewise constant estimation of the heat flux distribution in the direction normal to the plane of the ultrasound transducer. An even more detailed estimation is possible when the heat flux is calculated based on the temperature profile that satisfies the heat conduction model.

2.3.7 Parametrization with Thermal Conductivity Model

The temperature parameterization by a one-dimensional heat conduction models was usually adapted. When temperature of the distal end T_h is to be determined, the temperature at the location of the transducer T_c is independently measured, and the temperature distribution $T(z)$ can be estimated by adjusting a single boundary condition in order to match the predicted and the measured TOF of an echo produced by a reflection of the excitation pulse from the distal end of the ultrasound propagation path:

$$\rho C\frac{\partial T}{\partial t} = \frac{1}{r}\frac{\partial}{\partial r}k\left(r\frac{\partial}{\partial r}\right)T, \tag{2.30}$$

where ρ, C, and k are refractory density, heat capacity, and thermal conductivity, respectively.

When a 2D or 3D model is needed to provide an adequately accurate description of the temperature distribution in the sample, additional measurements will be required to reconstruct the temperature distribution. For example, consider the case of a cylindrical waveguide with the transducer, used to launch an excitation pulse in the axial direction, coupled to one of its ends. Assuming the radial symmetry of the temperature distribution, constant density ρ, heat conductivity k,

and capacity C_p, the temperature distribution inside the sample must satisfy the following 2D heat transport model in the cylindrical coordinates:

$$\rho C_p \frac{\partial T}{\partial t} = k\left(\frac{1}{r}\frac{\partial}{\partial r} r \frac{\partial T}{\partial r}\right) + \frac{\partial^2 T}{\partial z^2}, \tag{2.31}$$

where r is the radial position relative to the centerline of the sample. To completely define the problem, three boundary conditions—at the proximal, distal, and cylindrical surfaces of the waveguide—are required. If the waveguide is unstructured, only a single US echo will be produced by a reflection from a distal end of the sample, and measurement of its TOF will allow us to estimate only one of the three needed boundary conditions. The other two boundary conditions must be obtained from independent measurements. For example, if the temperatures of the distal and proximal ends of the waveguide are independently measured, then the measured Δt_{of} can be used to estimate the overall heat transfer coefficient h and define the remaining boundary condition given as the heat flux through the cylindrical boundary of the waveguide:

$$q = h(T_e - T), \tag{2.32}$$

where T_e is the ambient temperature of the environment. The time of flight of multiple echoes received when the excitation pulse propagates through a structured waveguide provide sufficient data to estimate all required boundary conditions without the need for the additional independent measurements. When such independent measurements are available, they can still be incorporated into the US-MSTD method and may help improve the accuracy and the robustness of the estimated temperature distribution.

CHAPTER 3

LOW TEMPERATURE LABORATORY EXPERIMENTS[1]

The feasibility of the proposed approach hinges on two questions:

1. Is it possible to create partial internal reflections along the path of the ultrasound propagation and what are the methods that can be used to create such reflections?

2. Is the speed of ultrasound propagation in the refractory temperature-dependent?

3.1 Cementitious Waveguide Partial Reflector Structures

Creating partial internal ultrasound reflections from known spatial locations inside the sample is the key prerequisite for the proposed approach to work. Two solutions, illustrated in Figures 2.2(A) and 2.2(B), were investigated. Figure 3.1(A) compares the ultrasound echo waveforms from two similar 4 cm long cementitious samples, one of which (waveforms in red) contains a few 0.5 mm steel shots placed in the middle of the sample during its casting.

The result clearly shows a partial echo from inside of the sample created by embedded scatterers, confirming the viability of the concept depicted in Figure 2.2(A). The range of other material has been investigated in order to find the most appropriate selection for internal scatterers. An ideal choice for partial reflectors would be a material with identical thermal expansion, and chemical and mechanical resistances similar to that of the surrounding refractory material; steel clearly does not satisfy these specifications.

---

[1]This chapter is adapted with permission from (Jia, Yunlu, et al. "Ultrasound Measurements of Temperature Profile Across Gasifier Refractories: Method and Initial Validation." Energy & Fuels 27.8 (2013): 4270-4277.). Copyright (2013) American Chemical Society

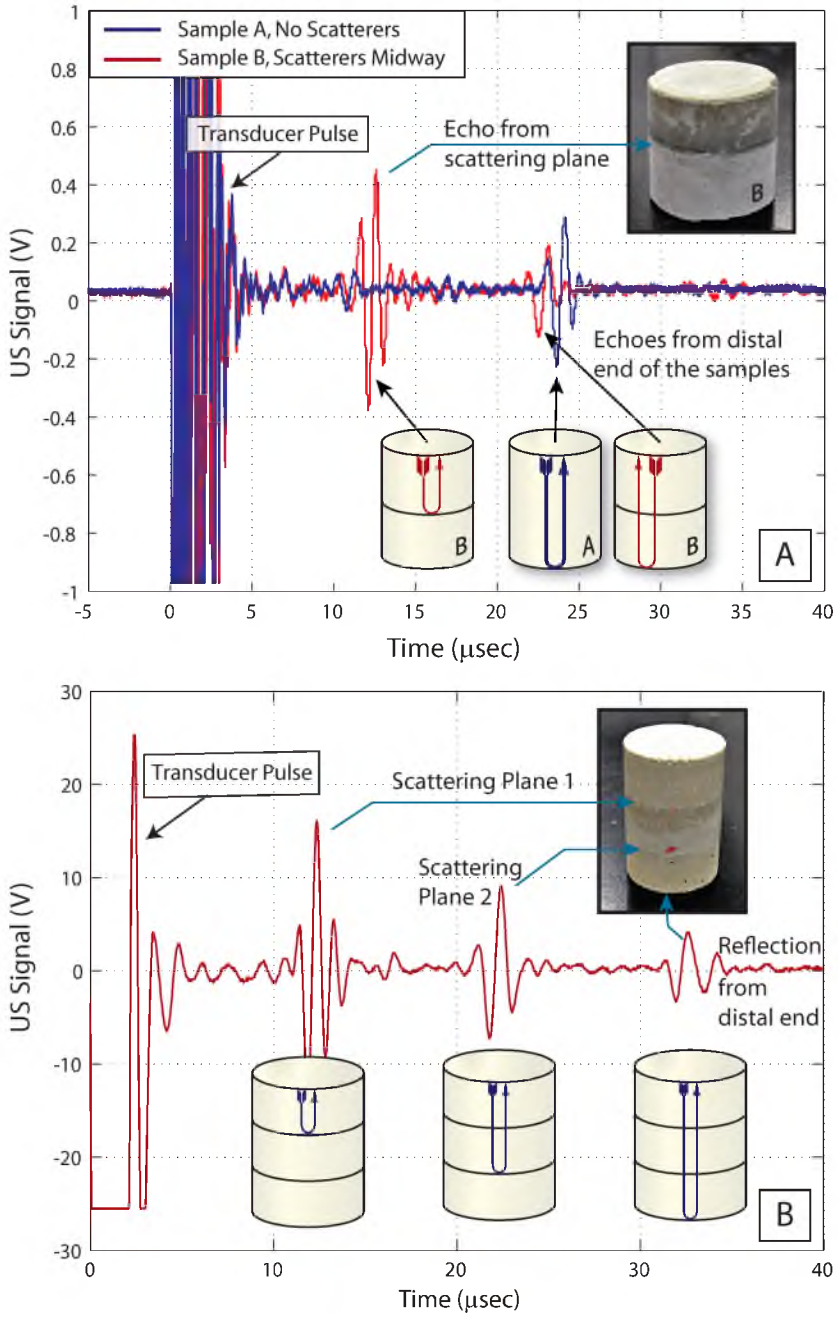

Figure 3.1: Ultrasound pulse-echo response for the samples with internal interfaces. (A) The pulse-echo ultrasound response of two samples fabricated from the identical cementitious material. One of the samples (Sample B; shown in inserted photograph) contains embedded ultrasound scatterers at the midpoint of ultrasound propagation path, which produces partial reflection (red line). (B) Ultrasound pulse-echo response for the sample with two internal interfaces obtained by sequentially casting three layers of identical formulation and allowing time for a partial cure to occur prior to pouring the next layer.

We, therefore, investigated if the concept depicted in Figure 2.2(B) can be implemented by using small variations in the composition of the layered cementitious materials, creating partial internal reflections at the interface between the layers. This indeed was found to be the case. In fact, it was found that by casting multiple layers of the *same* composition and allowing for a partial curing before casting the next layer, enough variation in acoustic impedance is introduced to create partial US reflections at the interface. Such implementation of the refractory with an embedded partial internal ultrasound reflector is particularly appealing since each layer will have essentially identical thermal, chemical and mechanical properties. Figure 3.1(B) illustrates this approach. It depicts the results obtained with the cementitious sample (shown in the insert) obtained by casting three 1-inch thick layers of identical cement mixture and allowing for a partial cure before the next layer is cast. Note three distinct echoes, produced at the two internal interfaces and the distal end of the sample.

To determine the conditions needed to create detectable partial internal reflections from the interfaces corresponding to consecutively cast layers, three groups of cementitious samples were made by layered casting using Portland type I/II cement. Two inches of I.D. PVC tubing was cut in lengths of 2, 3 and 4 inches and used as a mold. Water-cement mixture was poured into the vertically oriented PVC mold in several layers approximately 1 inch thick, altering the duration (cure time) between the previous and the subsequent pours. To help with uniform setting of each layer and removing of air bubbles, the mold was vibrated by high speed vibrator on the outside surface; alternative vibration methods are currently being tried. The curing time for different layers varied from 15 minutes to days. Fresh cementitious mixtures of identical composition were prepared right before the casting of each new layer. The water-cement ratio by weight also changed which was found to have a significant effect on the outcome. All samples were cured in air and at least one week was allowed after the casting of the final layer before ultrasound testing; this long cure eliminated short-term aging effects. The ultrasound tests of cementitious samples were carried out using a Panametrics pulser/receiver (model 5072PR) and a Panametrics immersion transducer with a

central frequency of 1 MHz (model V302), coupled to a sample using ultrasound gel. The data were acquired using a Tektronix oscilloscope (model MSO 2024) interfaced to a computer.

3.1.1 High Water-Cement Ratio Sample with Various Curing Times

The water-cement ratio used for this group of cementitious samples was 0.5, which is the highest water portion from manufacture's recommendation. With this ratio, the mix can be easily and uniformly poured into PVC molds. With two pours, each 1 inch thick, two layer samples are created that have a single internal interface.

To investigate the effect of the cementitious curing time, several samples were created in which we varied the time the first layer was allowed to cure prior to completing the sample with the second pour. The curing time for the first cementitious layer was set to 15, 30, 45 minutes or 1 hour for different samples.

The results of ultrasound tests show that the clearest partial internal reflections are observed with samples in which the first cementitious layer was allowed to cure for 1 hour (Figure 3.2).

The reflections from the internal interface are less clearly defined when the curing time was 45 minutes, indicating a smaller change in acoustic impedance between the layers that were cast with little delay (Figure 3.3(A)). Further reduction in time allowed for the first layer to cure makes the two layers even less distinguishable to ultrasound testing, indicating a very small change in ultrasound impedance between the layers under these circumstances. For the samples cured for only 15 minutes, we did notice the change in the ultrasound signature depending on the position of the ultrasound transducer relative to the center axis of the mold (Figure 3.3(B)). The signature is smaller closer to the center of the mold. We speculate that this may be due to the difference in temperature with radial position, caused by the cementitious curing (which is an exothermic hydration reaction), resulting in different curing rates in different spatial position. Apparently, the rate of curing is higher close to the mold. Pouring the second layer after 15 minutes of curing results in a situation where the center of the first layer is less cured, allowing partial mixing with the newly poured second layer, which results in a minimal variation

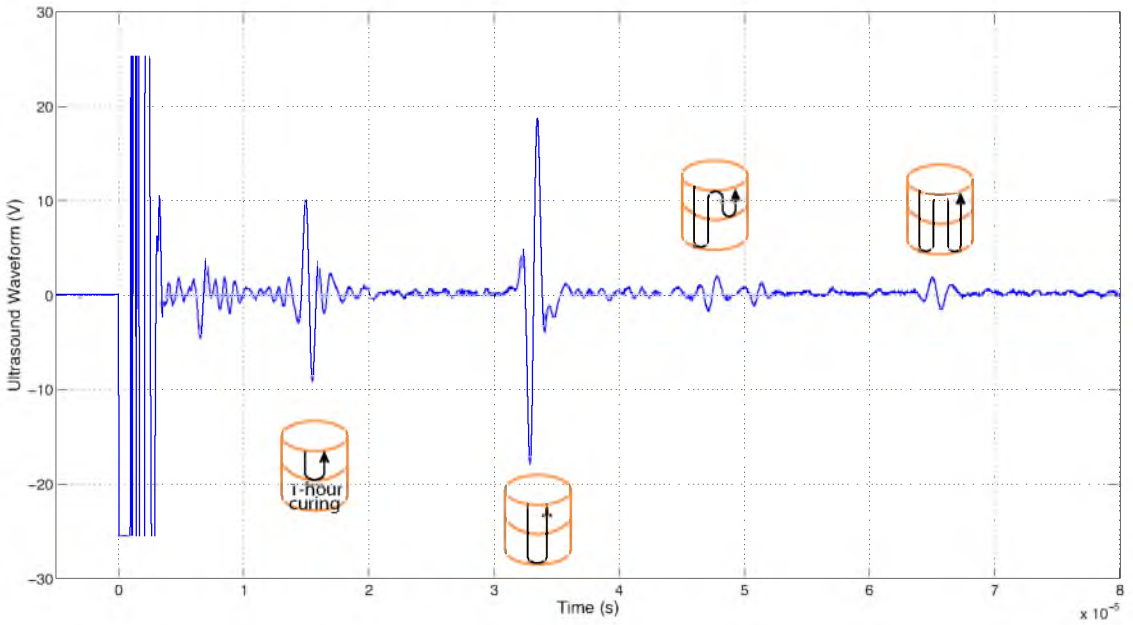

Figure 3.2: Ultrasound response for samples with the single internal interface obtained by allowing the first cementitious layer to cure for 1 hour. Inserts schematically depict the locations creating the acquired echoes: The first echo is the partial internal reflection from the interface of the two layers; the second echo is from the end of the sample. Round-trip echoes from partial internal reflection and the end are also shown.

in the ultrasound impedance of the two layers in the center of the sample.

3.1.2 Low Water-Cement Ratio Sample with Various Curing Times

This group of samples were cast with two internal interfaces obtained by sequentially casting three cementitious layers, 1 inch thick, using the water-cement ratio of 0.36, which was selected to be as small as possible while still allowing for layered casting of the sample with minimal air entrapment. The cure time for the first cementitious layer was also set to 15, 30, 45 or 60 minutes for different samples before pouring the second layer. The final, third layer was poured after the sample was allowed to dry for one day.

The ultrasound tests showed that all cementitious samples made according to this recipe exhibit partial internal reflections from each of two internal interfaces, even with short curing time of 15 minutes (Figure 3.4). However, the test also showed the signal-to-noise ratio (SNR) in this group (Figures 3.4, 3.5) is high, likely

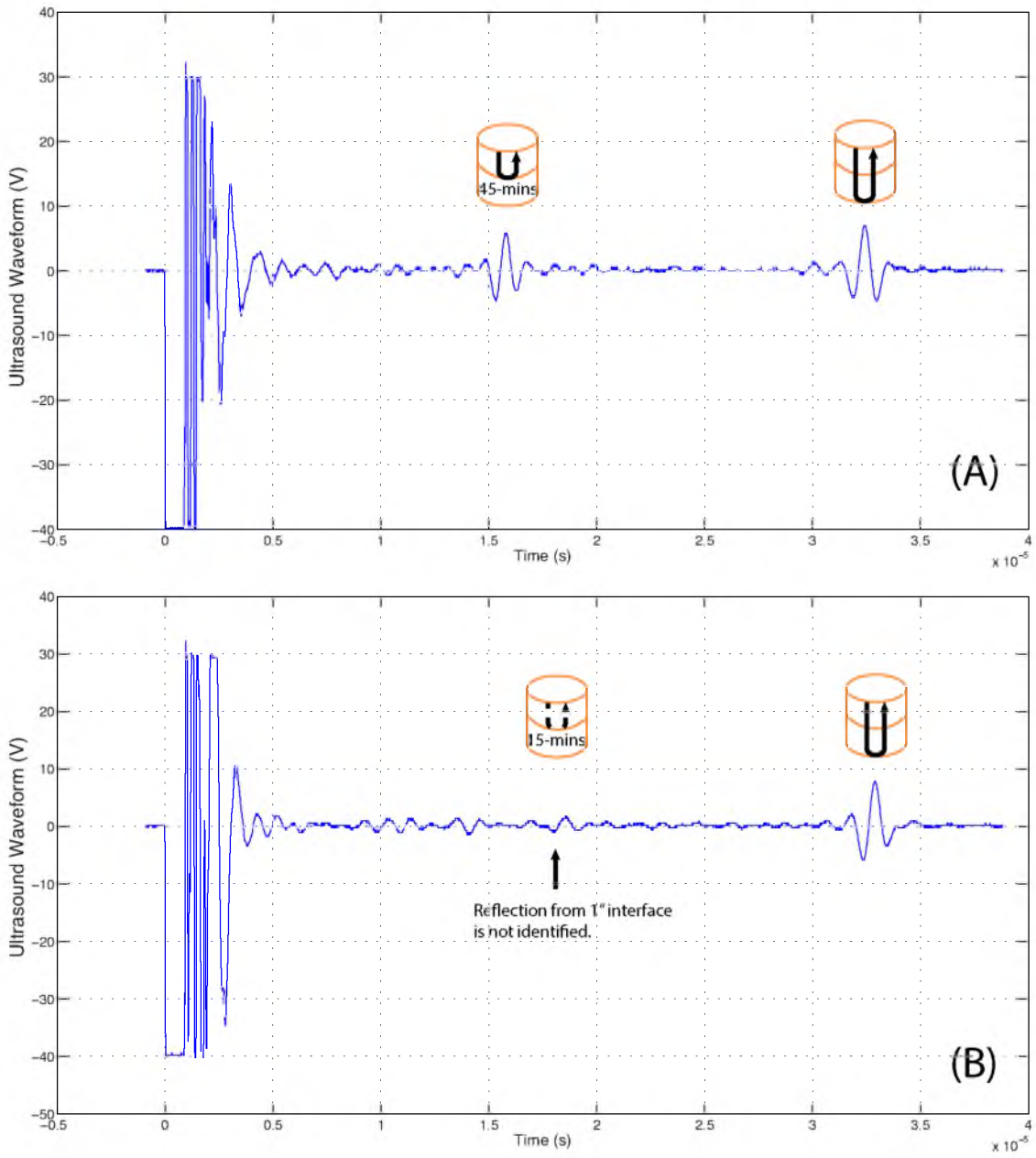

Figure 3.3: Ultrasound response for samples with the single internal interface obtained by allowing the first cementitious layer to cure for 45 minutes (A) and 15 minutes (B). Inserts schematically depict the locations creating the acquired echoes in (A) both the partial internal reflection and the end of the sample. The reflection from the interface is not well defined and varies with the change in the transducer position in (B).

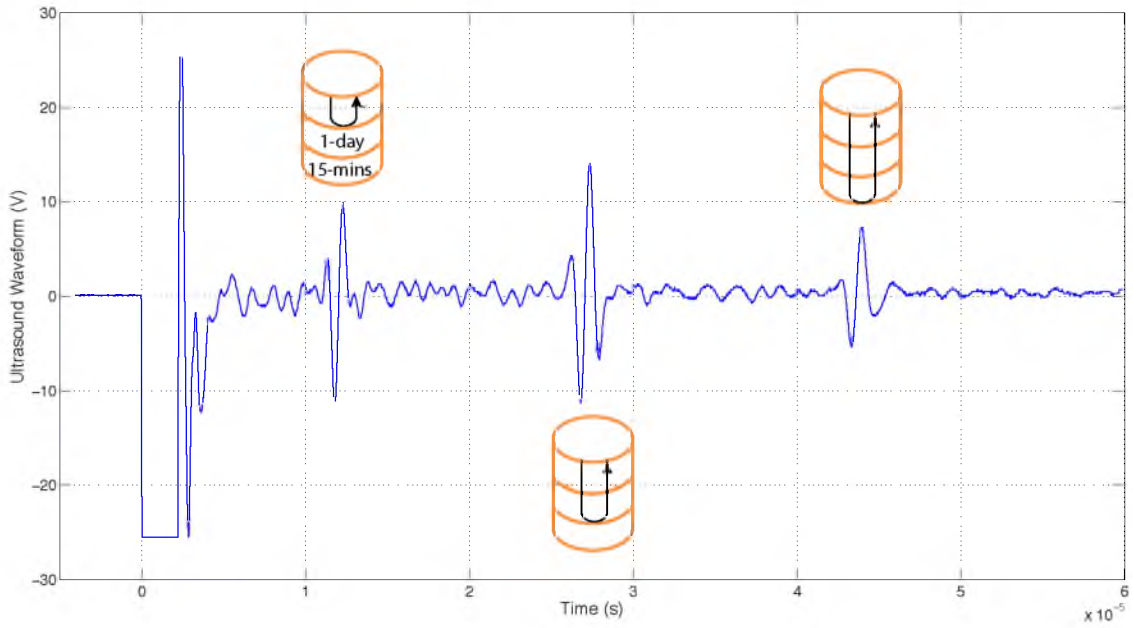

Figure 3.4: Ultrasound response for samples with the two internal interfaces obtained by allowing the first cementitious layer to cure for 15 minutes, 1 day for the second layer, and at least 1 day for the final third layer. Water-cement ratio equal to 0.36 was used. Inserts schematically depict the location creating the acquired echoes. Three echoes are clearly visible, of which the first two are from the internal interfaces created by multiple layers cast sequentially.

due to air entrapment during multiple castings of this mixture with a relatively low water content.

3.1.3 Medium Water-Cement Ratio Sample with Long Curing Time

The water-cement ratio equal to 0.44 was used to make the next series of samples. This ratio was chosen to be roughly an average of 0.36 and 0.5 values used with the already described samples. Our goal is to find the composition that gives an optimal trade-off between the ease of casting air free layers, which is easier to achieve with large ratios, without sacrificing the hardened strength of cementitious after curing, observed with high water content in the mixture.

The maximum of three layers were cast to make samples. Each layer was equal to or less than 1 inch in thickness. The purpose of these samples was to obtain initial experimental evidence on the shortest spacing between the interfaces, introduced to create internal ultrasound reflections, without overlap in consecutive echoes. By

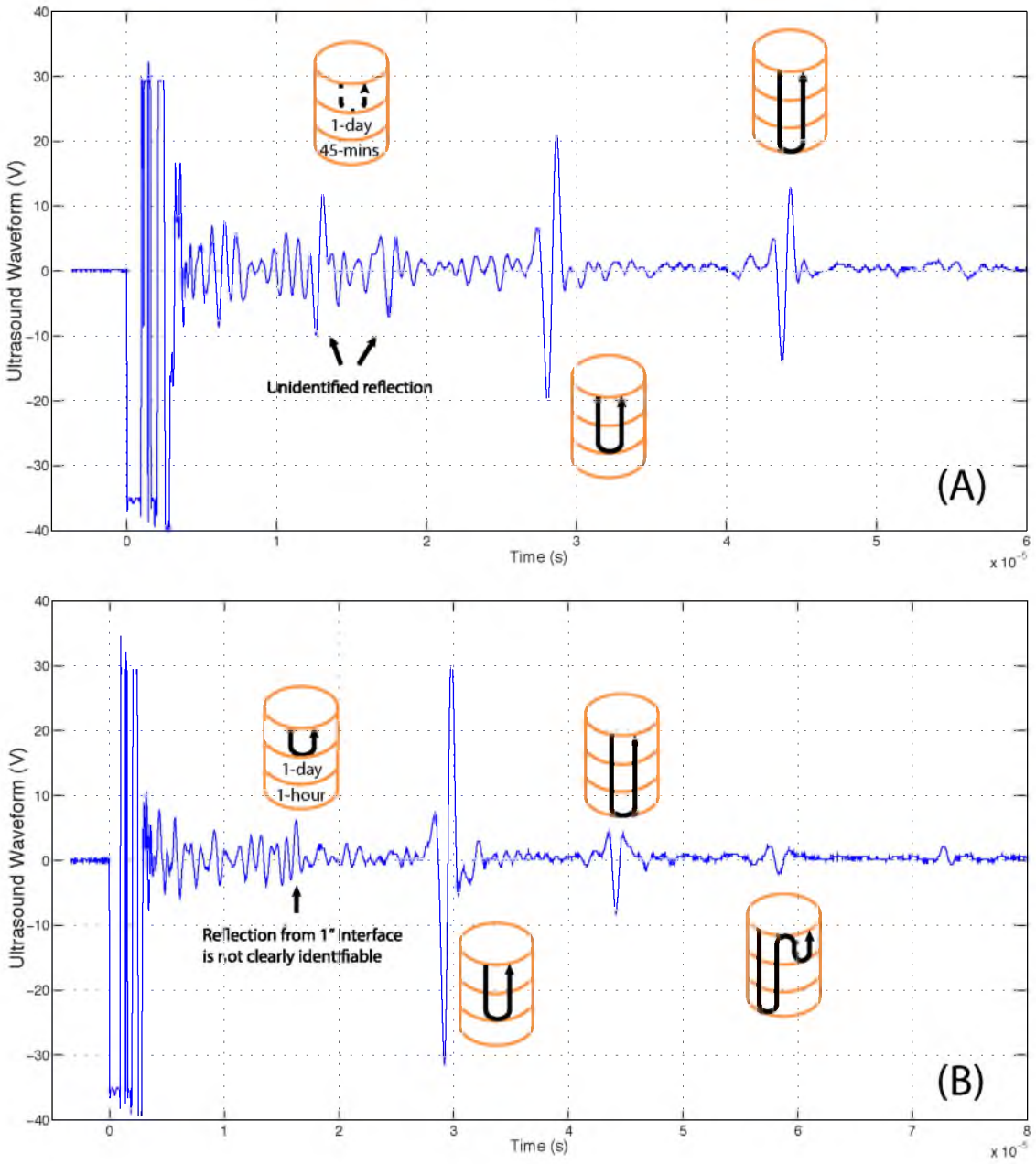

Figure 3.5: Ultrasound response for samples with the two internal interfaces obtained by allowing the first cementitious layer to cure for 45 minutes (A) and 1 hour (B), both 1 day for the second layer, and at least 1 day for the final third layer. Water-cement ratio equal to 0.36 was used. Echoes from the second interface and the end of the sample are clearly visible. However, the signal from the first interface is rather complex, likely indicating entrapment of air at the interface.

avoiding such overlap the signal analysis and the measurements of the ultrasound TOF are simplified. Each layer of prepared samples in this batch was allowed to cure for a long time that varied from one day to several days before the next layer was poured.

The ultrasound testing revealed that all samples in this group produce clear partial internal reflections from each interface. The reflections are clear without waveform overlap for 3-layered samples (Figure 3.6). This suggests that 1 inch or better spatial resolution of the ultrasound measurements of temperature distribution may be achieved with the proposed approach. The signal distortions in this and other samples prepared following this recipe (such as the two-layer samples for which the results are shown in Figures 3.7) are small, which is important for the precise measurements of the ultrasound time of flight.

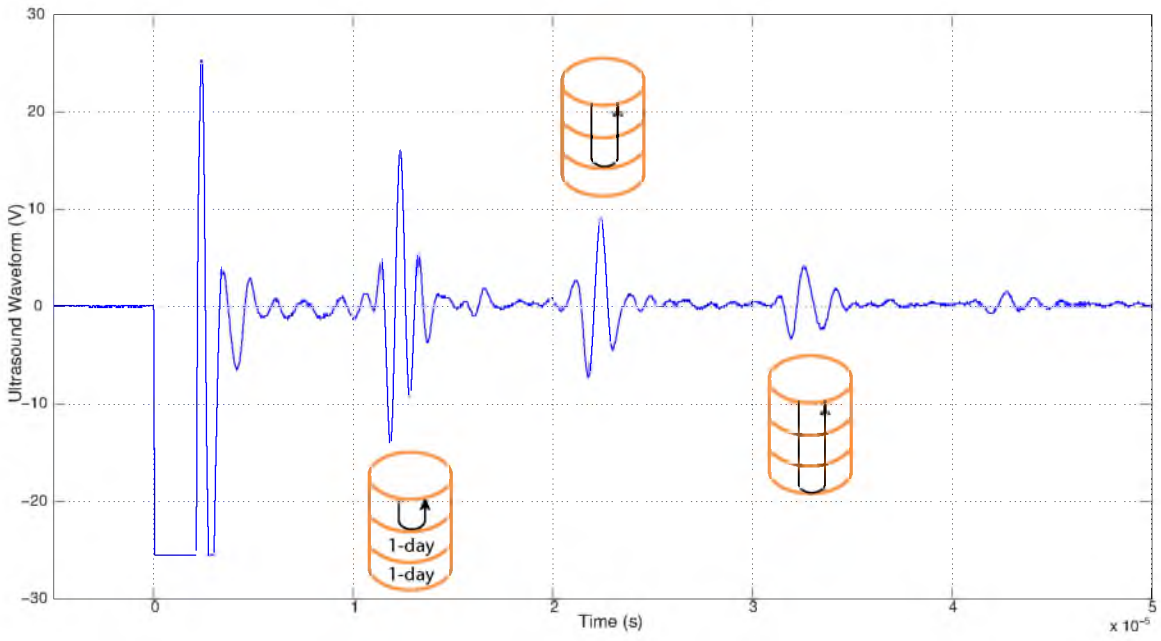

Figure 3.6: Ultrasound response for samples with the two internal interfaces obtained by allowing the two initial cementitious layers to cure for 1 day each. The last layer was cured for at least 1 day. Water-cement ratio equal to 0.44 was used. Echoes from both interfaces are well defined, with relatively high SNR.

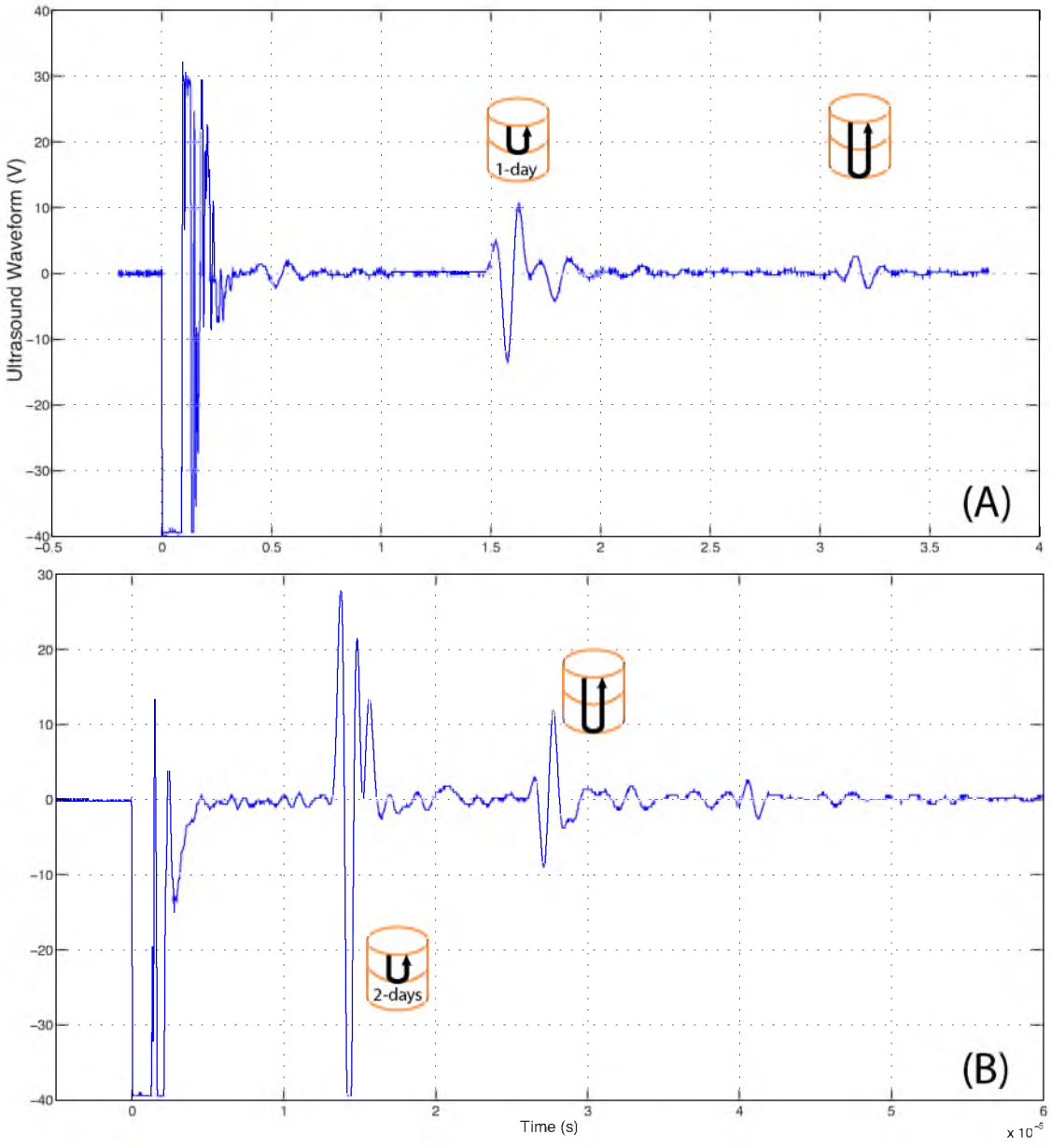

Figure 3.7: Ultrasound response for a sample with a single internal interface obtained by allowing the first cementitious layer to cure for 1 day (A) and 2 days (B). Water-cement ratio equal to 0.44 was used. Echoes from the interface and the end of the sample are well defined, with a relatively high SNR.

3.1.4 Summary of Partial Internal Reflection Structures

3.1.4.1 Composition

It was found that the Portland cement that was used produces samples that often cracked at the interface after soaking in water. Two new cement formulations were then examined to obtain a more stable model of the refractory.

1. In the first case, a fortifier was added to the Portland cement mixture to increase strength of the samples, adhesion between multiple layers and reduce permeability to water. In the following, samples prepared with this modifier are designated as PF (Portland Fortified samples).

2. Rapid Set® concrete mixture is the second formulation that we tested. It produced fast setting, high strength samples, with excellent bond between layers and crack resistance. Samples prepared using Rapid Set mix are designated as RS.

Samples prepared according to these two formulations have higher strength and less water permeability than samples prepared with the traditional Portland cement mix. The Rapid Set concrete samples were found to be much denser than other concrete samples. Their ultrasound waveforms are shown in Figure 3.8.

3.1.4.2 Water-Cement Ratio

Higher water-cement ratios, such as samples produced using the ratio equal to 0.44 and 0.5, lead to better defined partial internal reflections of the ultrasound test pulse and the measurements are characterized by higher SNRs. This is most likely due to reduced trapping of air bubbles in samples with higher moisture content and more planar interfaces obtained by casting of more "fluid" cementitious mixtures. Typically, higher water content is associated with the reduced mechanical strength of cementitious samples. For a particular cementitious mix used by us, it is recommended that the water-cement ratio should not exceed 0.5. A lower water-cement ratio is known to lead to higher strength and durability, but may make casting of uniform layers more difficult. For a particular cement mixture used by us, a minimum of 0.25 of water-cement ratio is required for cementitious mix to harden. A mix with too much water would result in internal cracks and fractures which will reduce the final strength. A maximum of 0.5 of water-cement

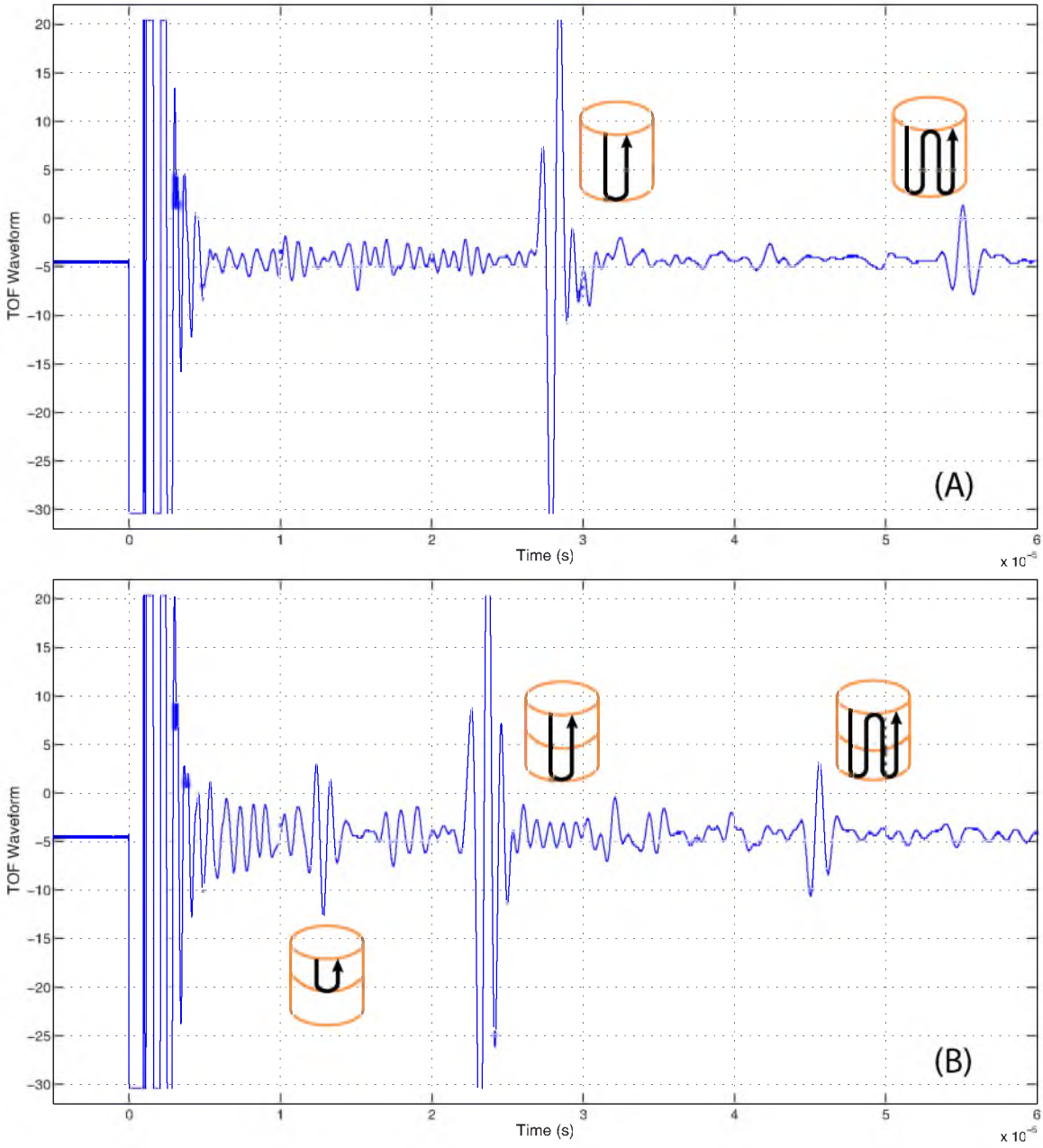

Figure 3.8: Ultrasound waveform collected for samples with a single internal interface obtained using Portland Fortified (A) and Rapid Set® cast (B). Echoes from the interface and the end of the sample are well defined, with a relatively high SNR.

ratio was used for making cementitious samples—the ratio that is still within the recommended range.

3.1.4.3 Air Bubbles

Vibration on freshly poured cementitious layers helps to reduce the amount of trapped air bubbles significantly. The presence of trapped air has a very significant negative influence on the quality of the required echoes. At the same time, vibrating samples prior to setting of the previously cast layers (short cure time of 15 minutes or less) likely contributes to the lack or poor quality of the measured echo signals. To vibrate the samples immediately following the pour of the newly prepared cementitious mixtures, we used a Fisher Sonic Dismembrator (Model 300) which provides high-frequency vibrations (on the order of 20 kHz).

3.1.4.4 The Partial Curing Time

For samples with water-cement ratio equal to 0.5 (the maximum value in the recommended range of the Portland cement mixture used by us), the curing time of less than 1 hour produced complex reflection patterns which suggest a diffused interface between sequentially cast layers. It was found that better defined reflections can only be observed on the edge of a cylindrical sample but not in the samples' center. To ensure the reflection can be observed everywhere on the sample surface, each layer curing time of at least 1 hour was found to be necessary. However, curing interlayers over days significantly reduced the bond effectiveness and sample strength at the interfaces.

3.1.4.5 Number and Spacing of Partial Reflections

We have demonstrated the acquisition of partial internal reflections from two interfaces inside the samples obtained by a sequential casting of three cement layers, allowing some time to cure each layer. At this time, we have shown that with the central frequency of 1 MHz, the echoes do not overlap when interfaces are spaced 1 inch apart. The distance between the features (interfaces between layers, in this case) that produce partial reflections determines the achievable spatial resolution of the temperature distribution measurements. Though a 1 inch spacing was

demonstrated so far, a closer spacing of partial reflectors may be possible with higher frequency of excitation, the sharper defined changes in acoustic impedance and the more advanced signal analysis techniques that can handle overlapping echoes.

3.1.4.6 Sample Length

We have demonstrated that with the current ultrasound pulser used in the pulse-echo mode, it is possible to characterize samples 2–4 inches long and obtain clear measurements of partial internal reflections from, at least, two internal interfaces. Longer samples (over 4 inches) can be characterized in transmission mode in which a separate transducer is used to generate the test pulse and the second transducer acquires the ultrasound signature after the excitation has propagated through the sample.

3.1.4.7 Consistency of Sample Properties

Consistency of the sample properties prepared following the same recipe was tested with RS samples. Three 2-inch samples were obtained in a single casting and had no internal ultrasound reflectors. The other three samples in the group were 3 inches long and had a single partial internal reflector created by casting two cement layers of identical mixture and allowing for a partial cure between consecutive layers. All samples were prepared and made at the same condition, from the same mixture ratio.

The speed of sound measurements for the two groups of samples were carried out, both in the water bath and the air. All samples were tested in the following order: (1) in air, (2) fully immerged in water and saturated, (3) in air again, after one week drying at room temperature. The time of flight was measured as a time delay between two echoes from the distal end of the sample produced by an ultrasound pulse acquired after a single or two round trips. SOS was determined as: $c = 2L/t_{of}$, where the length of the sample, L, was measured with a micrometer. The results for all six samples are shown in Figure 3.9. The solid and hollow shapes represent the SOS results from three 2-inch and three 3-inch samples, respectively, presented by the primary y-axis. The secondary y-axis shows the densities of all

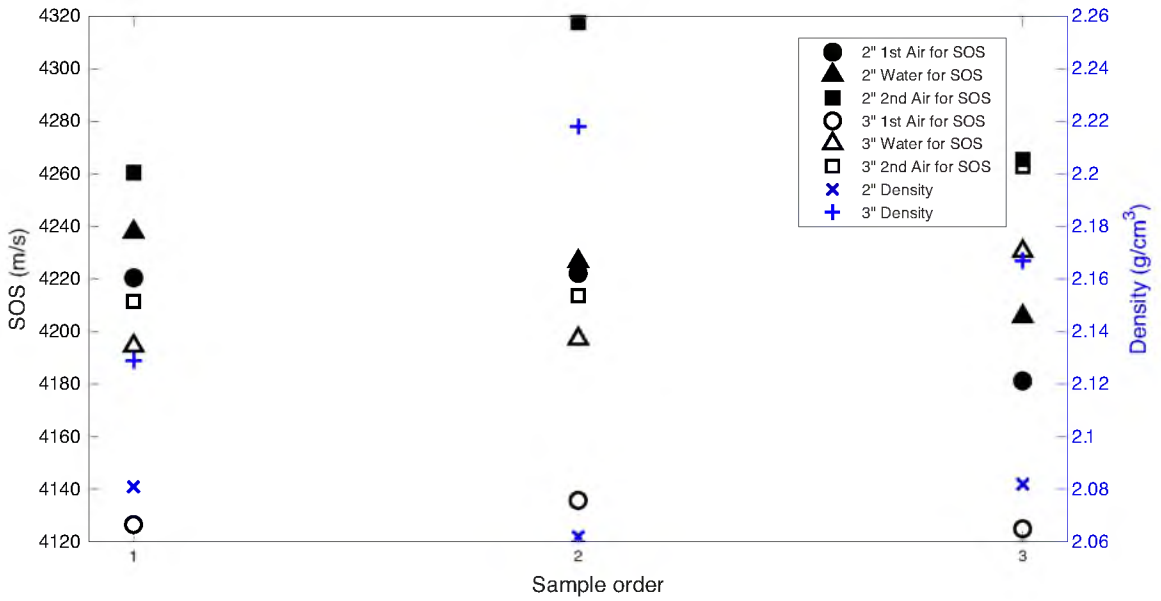

Figure 3.9: Two groups of RS samples tested in the water bath and air show great variability in both the SOS versus temperature relationships and density measurements.

samples. The results indicate some variability between samples in the same group, like significant SOS increments when sample is saturated, and higher variabilities between different groups, both in the SOS and the density.

3.2 Experiments of Temperature Measurements

3.2.1 Structured Cementitious Waveguide

In this study, a cementitious sample obtained by casting of Portland Type I/II cement was selected as a model of castable refractory. A 2-inch I.D. PVC tubing was used as a mold and a 4-inch sample was created by sequentially casting four layers (each 1 inch thick) of cement mixture and allowing 30 minutes curing time between consecutive layers. The mold was vibrated by an external vibrator after each pouring to ensure uniform setting of each layer and to remove air bubbles. The samples were cured and aged at ambient temperature until their ultrasound properties stabilized.

The ultrasound tests of cementitious samples were carried out using a Panametrics pulser/receiver (model 5072PR) and a Panametrics immersion transducer with a central frequency of 1 MHz (model V302), coupled to a sample using ultrasound

gel. The data were acquired using a Tektronix oscilloscope (model MSO 2024) interfaced to a computer.

3.2.2 TOF Acquisition from Ultrasound Waveform

The other essential prior condition to apply the proposed ultrasound method is the SOS dependence on the temperature. Figure 3.10 illustrates typical ultrasound waveforms acquired in this configuration from the same sample maintained at different uniform temperatures. The echoes are produced at the distal end of the sample. The first echo seen in the figure corresponds to the ultrasound pulse that traveled the length of the sample and back (a single round trip), while the second measured echo corresponds to the same pulse after it made the second round trip through the sample. The direct inspection of waveforms in Figure 3.10 indicates that the speed of sound in the model refractory indeed depends on temperature, decreasing as the temperature goes up, leading to longer time of flight of ultrasound pulse at higher temperatures.

To establish the correlation between the speed of sound and temperature, the 4-

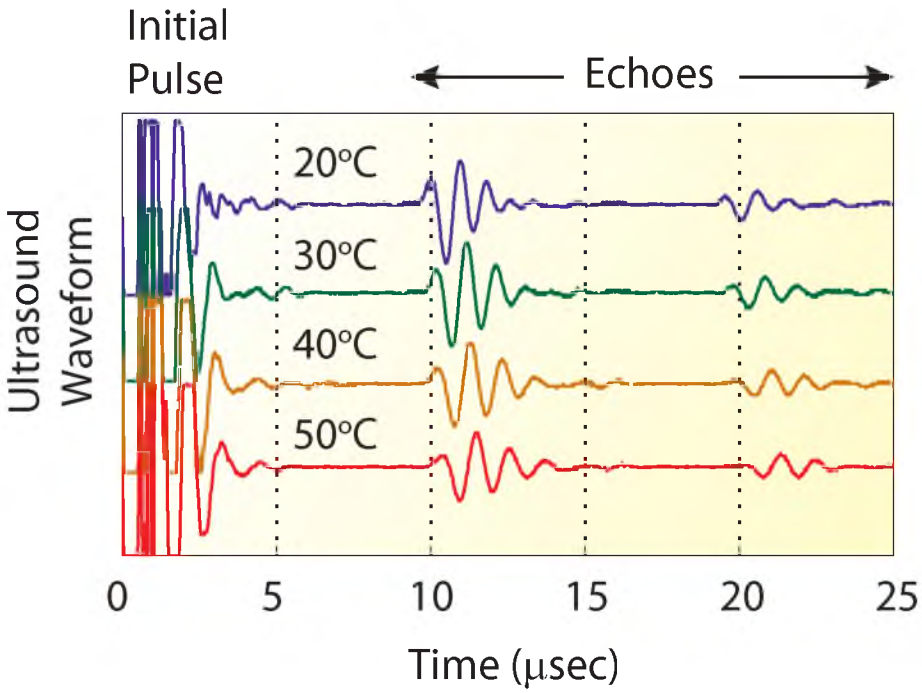

Figure 3.10: Ultrasound waveforms acquired at different temperatures illustrate the TOF shift with temperature.

inch sample was placed inside the fabricated heating fixture depicted in Figure 3.11, which consisted of a thermally insulated steel container and an internal heating blanket (silicon rubber blanket by BriskHeat®) that tightly surrounded the sample. The temperature of the blanket was measured by a thermocouple and controlled by a PID controller. The surface temperature of the sample was measured by four Omega Precision Fine Wire Thermocouples attached with high-temperature adhesive tape in the middle of each layer of the model refractory. Two additional thermocouples of the same type were used to measure the temperature of the top and bottom surfaces of the sample.

The ultrasound transducer was coupled to the surface of the top layer of the sample (Layer 1, $L1$). To prevent damage to the transducer, the top surface of

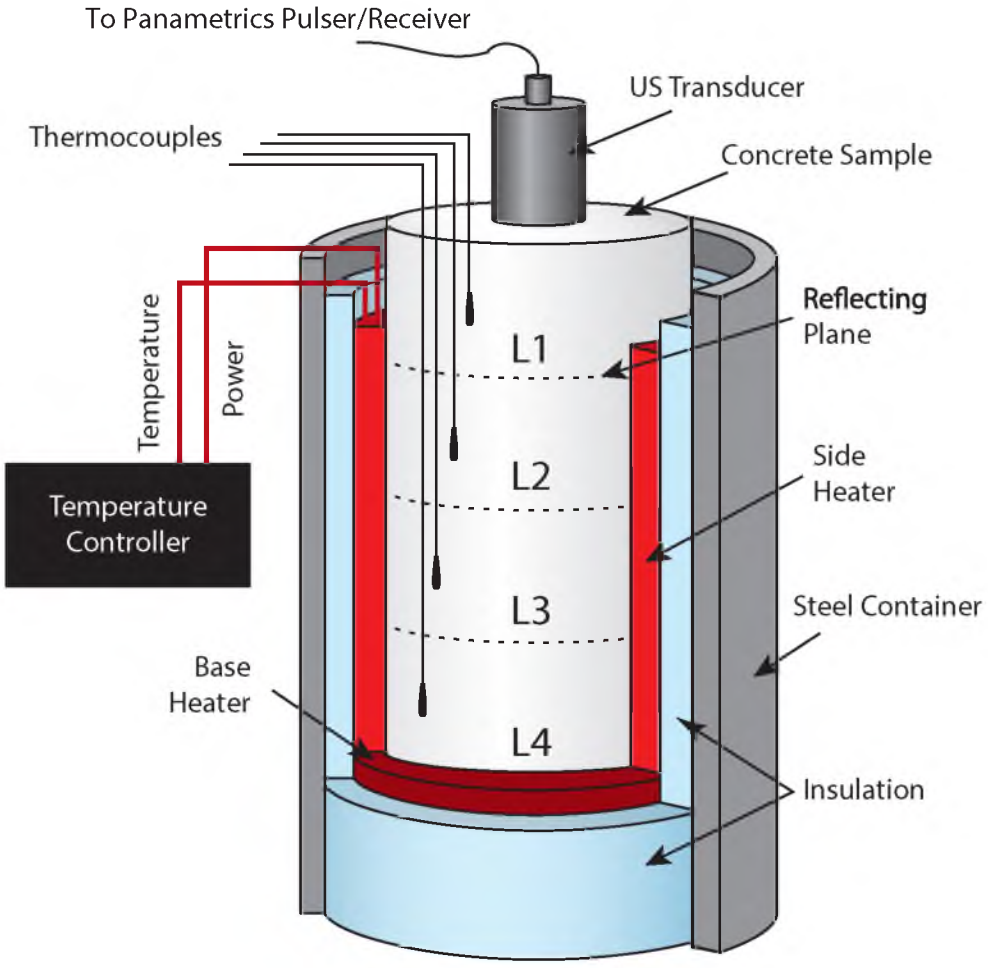

Figure 3.11: Experimental setup of 4 inches, 4 segments cementitious sample for low temperature measurements.

Layer 1 extended above the fixture to allow for partial cooling of the sample; in this arrangement, Layer 1 is effectively used as a delay line. The test temperatures were changed in 10°C increments and spanned from 20 to 100°C in this study. After each temperature change, sufficient time was allowed for thermal equilibration to occur before attempting the time of flight measurements. The sequence of temperatures for which the SOS measurements were conducted was randomized. The randomization included all repeat experiments for each temperature. Such randomization avoids measurement potential bias introduced when temperatures always changed in one direction (either an increasing or decreasing temperature) and by a fixed increment of temperatures from one experiment to the next. We noticed that the interface between the consecutive layers is not entirely flat or smooth (a consequence of coning, partial penetration and/or mixing between layers). To account for unevenness of the interfaces, during the repeat experiments the positioning of the transducer was slightly shifted relative to the centerline of the sample and kept at the same location for all the tests.

3.2.3 Signal Processing

Several methods for determining the TOF from the waveforms typified in Figures 3.10 were investigated. Our initial approach was to use a delay line and the echo signal from sample-delay interface as a reference "zero time" from which the time of flight is calculated. The time of flight is then calculated by matching single-point features (e.g., peak value or zero crossing) in the reference waveform from the sample-delay interface and the waveform of the reflection produced by internal interfaces and the end of the sample. Though this approach is standard, we encountered difficulties in its applications. Cementitious refractory materials are dissipative and have higher absorption of higher frequency components of the ultrasound wave, which leads to distortion and broadening of the echo waveform and thus errors in determining the time of flight based on a single-point feature matching. We therefore opted to use the cross-correlation between the echo waveforms obtained at different temperatures to determine the difference in the time of flight at two different temperatures, ΔTOF.

For dissipative samples higher accuracy may be obtained if cross-correlation is performed between the analytical envelopes of the waveforms, rather than the waveforms themselves [59]. To test the potential improvements, we implemented the envelope cross-correlation method and compared its performance with the TOF measurements based on the waveform cross-correlation. A numerical procedure based on the Hilbert Transform is applied to the waveform in the time domain to create an envelope of the waveform. This is a representation of the amplitude modulation on the carrier wave frequency. The procedure also creates a time-domain phase function which has application to interpreting dispersion. Figure 3.12 shows the comparison of results obtained using the cross-correlation between the waveforms (left 2 columns) and the envelopes of the waveforms. The offsets (ΔTOF) between the reference waveform and its envelope (green lines) and the waveforms and their envelopes of the echo signals acquired when the sample was maintained at different temperatures (blue lines) are listed for each subfigure. The two methods give a similar trend of increasing time of flight with temperature but differ in values of ΔTOF. In further analysis, the envelope cross-correlation method is used as an approach less sensitive to the waveform distortion.

The envelope of the echo waveforms in Figure 3.13A (collected when the sample was maintained at the uniform reference temperature of 20°C) is shown as the top

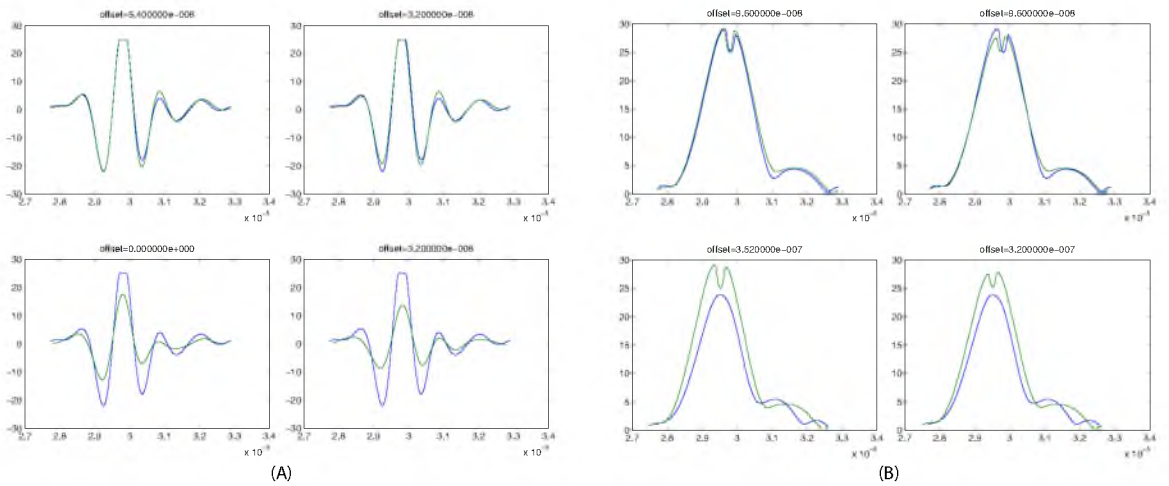

Figure 3.12: Comparison of the estimated ΔTOF (offsets) at different temperatures obtained by cross-correlating the waveforms (panel (A)) or envelopes of the waveforms (panel (B)).

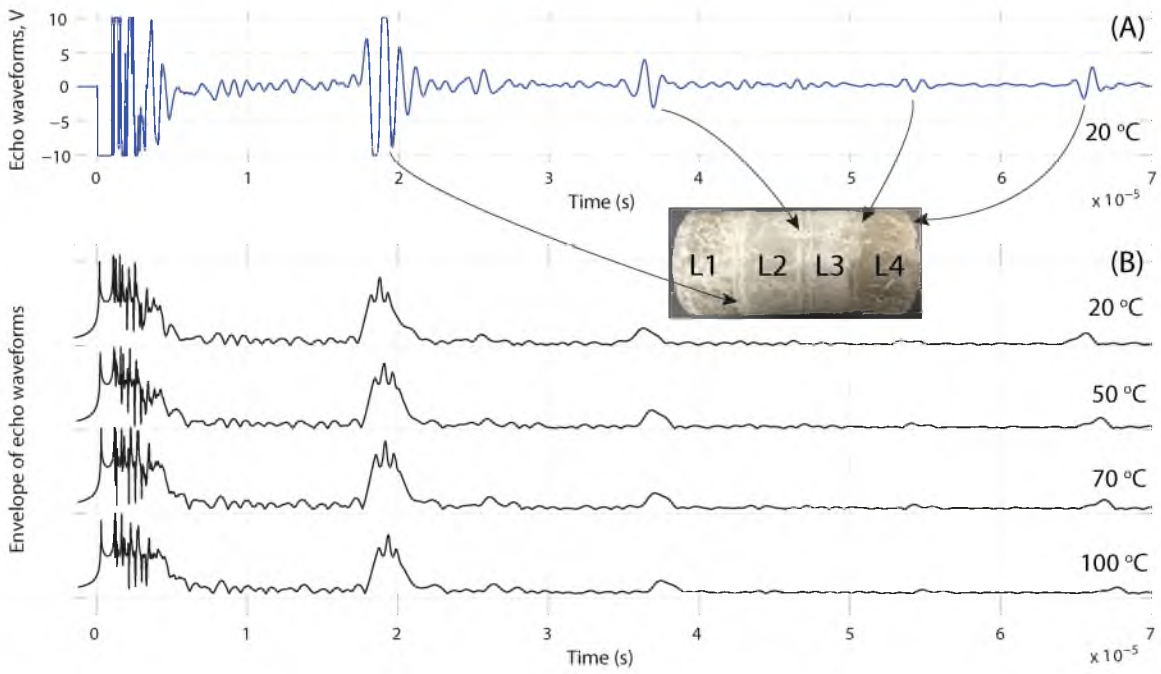

Figure 3.13: (A) Typical waveforms of ultrasound echoes created by the interface between different layers *Li* of the cementitious sample (insert) and the sample-air interface at its distal end. The measurements were acquired at the reference temperature of 20 °C. (B) Envelopes of echo waveforms collected at different temperatures.

graph in Figure 3.13B. The remaining graphs in Figure 3.13B show the envelopes of the waveforms collected during the calibration experiments when the sample was maintained at the elevated uniform temperatures (results for 50, 70 and 100 °C are shown). Visual comparison of the envelopes indicates a distinct trend towards an increased TOF as the temperature increases, and therefore the reduction in the speed of sound c through the sample at elevated temperatures.

The overall procedure for the data analysis using the envelope cross-correlation method and the speed of sound calculation is summarized in the following steps:

1. The reference zero time (or trigger) is maintained the same for all measurements.

2. The reference waveforms, which include 4 echoes from the three internal interfaces and the distal end of the sample, are acquired at the reference temperature, selected to be 20 °C.

3. The temperature tests are conducted in random order, with at least 6 repeats

for each temperature. During each test, 20 waveform sequences are collected and averaged.

4. The envelope cross-correlation between the reference and the averaged waveforms is applied to find ΔTOF at a given temperature relative to the reference temperature of 20 °C.

The change in the time of flight of an echo produced by i-th internal interface relative to the TOF at the reference temperature T_{20} is equal to

$$\Delta t_{of}^{z_i}(T) = t_{of}^{z_i}(T_{20}) - t_{of}^{z_i}(T) = 2\left[\frac{z_i}{c(T_{20})} - \frac{z_i}{c(T)}\right]. \tag{3.1}$$

To quantify $\Delta t_{of}^{z_i}(T)$ from the ultrasound measurements, we used the cross-correlation of the waveform envelope, A_T, of an echo obtained at the temperature T with the corresponding echo acquired at the reference temperature, T_{20}:

$$A_{T_{20}} \star A_T = \int_{-\infty}^{+\infty} A_{T_{20}}(t) A_T(t+\tau) dt. \tag{3.2}$$

The temperature-induced change in the TOF is then obtained as a delay (shift) τ between $A_{T_{20}}$ and A_T needed to maximize their cross-correlation. Formally, for i-th echo we find $\Delta t_{of}^{z_i}(T)$ as the solution of the following problem:

$$\Delta t_{of}^{z_i}(T) = \operatorname{argmax}_\tau \int_{-\infty}^{+\infty} A_{T_{20}}(t) A_T(t+\tau) dt. \tag{3.3}$$

5. The speed of sound $c_1, \ldots, c_4$ in each layer of the sample is calculated at each temperature:

$$c_1 = \frac{2L_1}{\left(t_{of_1}(T_{20})\right) + \left(\Delta t_{of}^{L_1}(T)\right)}, \tag{3.4}$$

$$c_2 = \frac{2L_2}{\left(t_{of_2}(T_{20}) - t_{of_1}(T_{20})\right) + \left(\Delta t_{of}^{L_2}(T) - \Delta t_{of}^{L_1}(T)\right)}, \tag{3.5}$$

$$c_3 = \frac{2L_3}{\left(t_{of_3}(T_{20}) - t_{of_2}(T_{20})\right) + \left(\Delta t_{of}^{L_3}(T) - \Delta t_{of}^{L_2}(T)\right)}, \tag{3.6}$$

$$c_4 = \frac{2L_4}{\left(t_{of_4}(T_{20}) - t_{of_3}(T_{20})\right) + \left(\Delta t_{of}^{L_4}(T) - \Delta t_{of}^{L_3}(T)\right)}, \tag{3.7}$$

where $L_1 \ldots, L_4$ are the thicknesses of each layer; $t_{of_1}(T_{20}), \ldots, t_{of_4}(T_{20})$ are the times of flight of reference echoes originating from the three internal interfaces and the

distal end of the sample; $\Delta t_{of}^{L_1}(T), \ldots, \left(\Delta t_{of}^{L_4}(T) - \Delta t_{of}^{L_3}(T)\right)$ are the differences between time of flights at reference and test temperatures. The overall length of the sample, $L = \sum_{i=1}^{4} L_i$, was measured using a micrometer, and the speed of sound at the reference temperature was calculated using Equation 2.4, where TOF is equal to $t_{of_4}(T_{20})$ which is the time of flight of the echo produced at the distal end of the sample. With known speed of sound at the reference conditions, the thicknesses of each layer L_i were calculated using the measurements of $t_{of_1}(T_{20}), \ldots, t_{of_4}(T_{20})$.

3.3 Results

3.3.1 The Calibration the SOS and Temperature

The speed of sound versus temperature calibration results for all four layers of the sample, obtained using the described procedure, are shown in Figure 3.14. The obtained SOS on the vertical axis is plotted as a function of the temperature measured by thermocouple attached at the center of each segment's surface of the model refractory sample. The data for all four layers were used to obtain a linear fit of the speed of sound as a function of temperature, which is expressed as

$$c = f(T) = -1.06T + 3240.3, \quad 20\,^{\circ}\mathrm{C} \leq T \leq 100\,^{\circ}\mathrm{C}. \tag{3.8}$$

The obtained correlation is plotted with the 95% confidence interval, shown as the shaded area.

3.3.2 Nonuniform Temperature Distribution

The proposed method for measuring nonuniform temperature distribution in the cementitious sample was tested. The sample was placed inside the fixture shown in Figure 3.11 and was heated using the base heater only. After the temperature measurements provided by surface thermocouples stabilized at constant values, an ultrasound excitation pulse was applied to the sample and the four return echoes were acquired. Using the envelope cross-correlation method, the TOF of each echo was determined, and the result was used to estimate the apparent speed of sound in each layer needed to produce the observed time of flight for each echo. Based on the calibration data, thus obtained SOS of each layer provided the corresponding temperature of each layer.

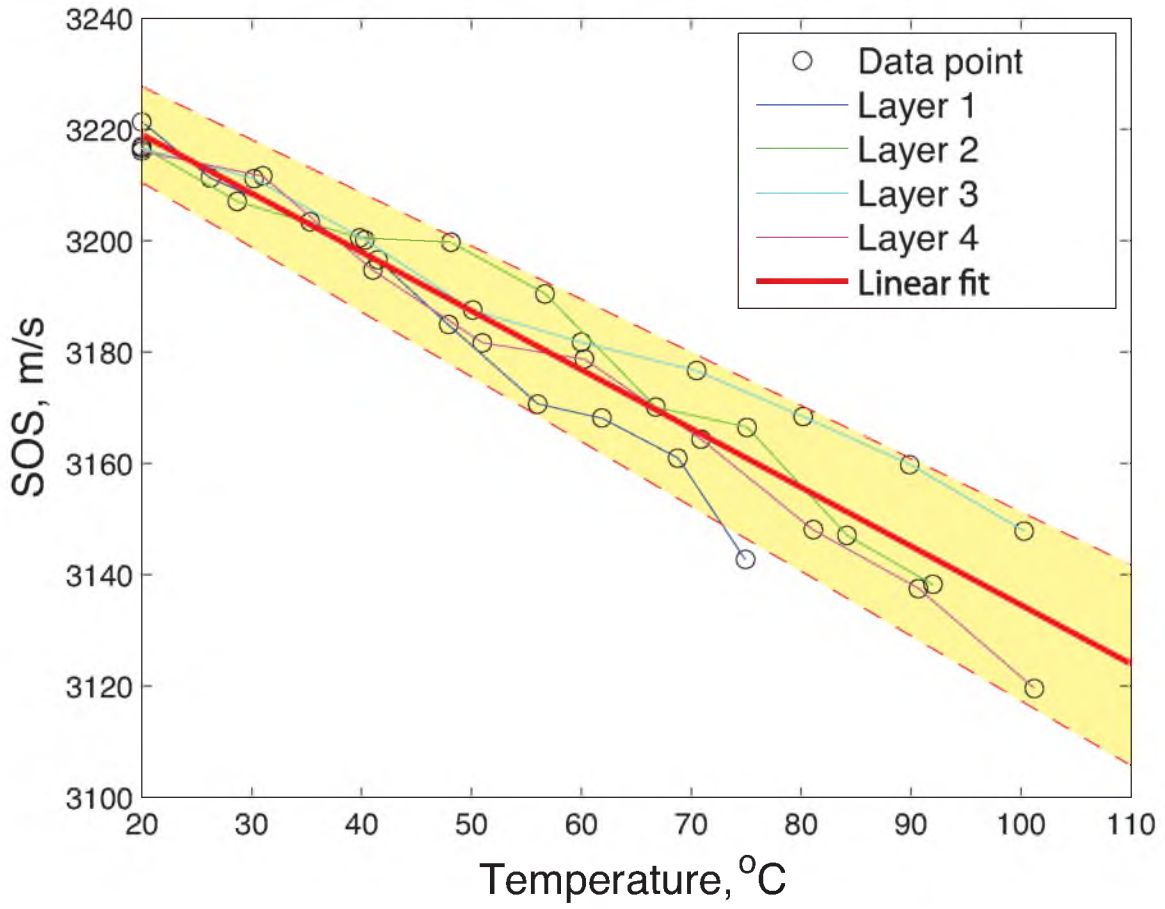

Figure 3.14: The calibration curves for the SOS as a function of temperature for all four layers of the sample were obtained using envelope cross-correlation data analysis methods. The shown linear fit $SOS = f(T)$ is based on data for all four layers. The shaded areas show the 95% confidence interval for the obtained linear fit.

When the temperature in the i-th segment is nonuniform, the obtained values of $t_{of_i}(T_{ref})$ and $t_{of_{i-1}}(T_{ref})$ used in Equation 2.19 give the following equation:

$$t_{of_i}(T) = \left(t_{of_i}(T_{ref}) - t_{of_{i-1}}(T_{ref})\right) + \left(\Delta t_{of}^{z_i}(T) - \Delta t_{of}^{z_{i-1}}(T)\right) = 2\int_{z_{i-1}}^{z_i} \frac{1}{f(T(z))} dz, \qquad (3.9)$$

from which an unknown temperature distribution $T(z)$ within the segment must be found by using the discussed options for the temperature parametrization.

3.3.2.1 Piecewise Constant Distribution

The assumption of constant temperature in each segment coupled with the calibration Equation 3.8 give the piecewise constant estimation of T(z), with the

temperature in the i-th segment equal to

$$T_i = 3056.89 - \frac{1.89(z_i - z_{i-1})}{t_{of_i}}. \tag{3.10}$$

This piecewise constant parametrization was previously used in [51], and is included in Figure 3.15(A), for comparison. The thermocouple measurements of the surface temperature in the middle of each segment are also shown. Though the simplest possible parametrization that leads to a discontinuous change in the estimated temperature at the location of echogenic features, it was still able to capture the correct trend in the temperature distribution along the sample.

3.3.2.2 Piecewise Linear Distribution

The assumption of temperature in each segment changing linearly parametrizes the temperature distribution in the i-th segment as

$$T_i(z) = m_i z + n_i, \tag{3.11}$$

where m_i and n_i are unknowns. Coupled with the linear relationship in Equation 3.8 between the speed of sound and the temperature, this parametrization used in

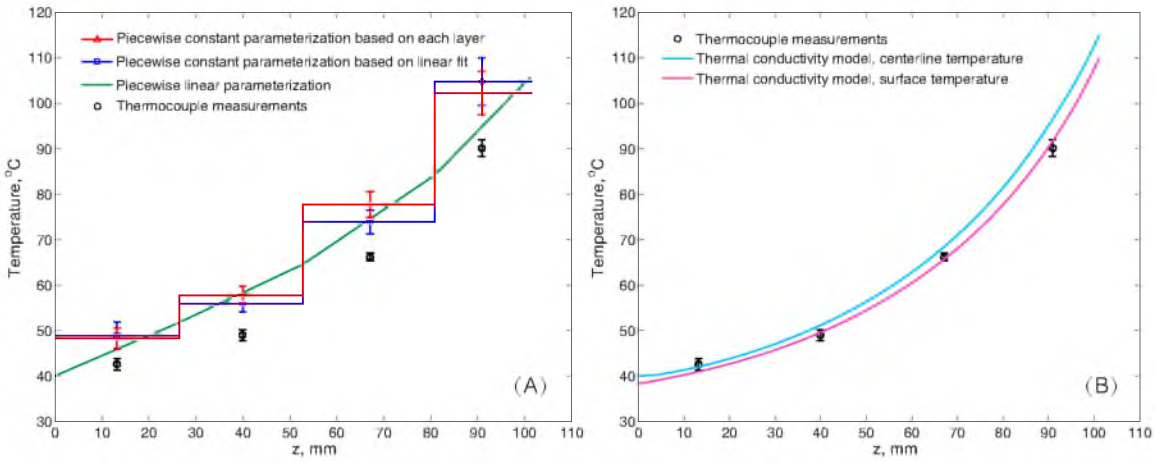

Figure 3.15: Temperature distributions from ultrasound and thermal model parameterizations compared with thermocouple measurements. (A) Estimated temperature distributions based on piecewise constant and piecewise linear parameterizations are compared with the measurements of the surface temperature obtained with thermocouples attached in the middle of each segment. (B) The parametrization based on 2D thermal conductivity model can be used to estimate the temperature distribution along the centerline and the surface of the waveguide.

Equation 2.19 gives:

$$t_{of_i} = 2\int_{z_{i-1}}^{z_i} \frac{1}{a(m_i z + n_i) + b} dz, \tag{3.12}$$

where a and b are from Equation 3.8. After performing the integration and requiring that the temperature remain continuous at the interface of the two segments, the following two equations are obtained in an unknown slope and intercept appearing in Equation 3.11:

$$t_{of_i} = \frac{2}{am_i} \ln\left[a(m_i z + n_i) + b\right]_{z_i}^{z_{i+1}}, \tag{3.13}$$

$$m_i z_{i-1} + n_i = m_{i-1} z_{i-1} + n_{i-1}. \tag{3.14}$$

By combining Equation 3.13 and 3.14 for all segments of the waveguide, and $n_1 = T(0)$ from the first segment by using independent (thermocouple) measurements of $T(0)$, which is the temperature at the transducer location, we have a sufficient number of conditions to find the piecewise linear temperature distribution across the entire waveguide.

For the four segments of the waveguide used in our experiments, the estimated piecewise linear temperature distribution is shown in Figure 3.15(A). Though an improvement over the piecewise constant distribution, a substantial difference ($\sim 10\,^{\circ}\mathrm{C}$ at $z = 10$ mm) with the thermocouple measurements is still apparent.

Both ultrasound and thermocouple results show a similar trend in temperature distribution. Two factors likely contribute to the observed difference in the measured temperature. First, it is reasonable to expect that the surface temperatures of the sample are indeed lower than the internal temperature measured noninvasively by the ultrasound, explaining some of the observed differences. Second, the thermocouples provide essentially point-wise measurements of temperature, while the ultrasound measurements depend on temperature distribution along the entire sample.

3.3.3 Parametrization with 2D Thermal Conductivity Model

A much more accurate estimate of the temperature distribution will be obtained if a more realistic "subgrid" parameterization is used. For example, we expect that by requiring that the temperature distribution satisfy the realistic heat transport model (e.g., the conduction model of Equation 3.15 supplemented with

the boundary temperature condition at the transducer's location), the accuracy of the temperature distribution based on ultrasound measurement and the estimation of the hot boundary temperature will improve.

The heat conduction model was developed in COMSOL Multiphysics. The temperature distribution inside the sample must satisfy the following 2D heat transport model in the cylindrical coordinates:

$$\rho C_p \frac{\partial T}{\partial t} = k\left(\frac{1}{r}\frac{\partial}{\partial r} r \frac{\partial T}{\partial r}\right) + \frac{\partial^2 T}{\partial z^2}. \tag{3.15}$$

Constant values of ρ, C_p and k were assumed, which were 1200 kg/m^3 (from lab measurement), 1.55 kJ/kg·K (from dry cement properties) and $26.91 - 0.25T + 8.61 \times 10^{-4}T^2 - 1.00 \times 10^{-6}T^3$ W/m·K (from Comsol Toolbox), respectively. The temperature of the proximal and distal ends of the waveguide and the heat flux through its cylindrical surface were used as the three boundary conditions needed to completely define the model. Temperature distributions on both end surfaces of the waveguide were assumed to decrease linearly from the centerline ($r = 0$) to its cylindrical edge ($r = 25.4$ mm). The thermal image of the transducer coupled with the proximal end of the waveguide ($z = 0$, Figure 3.16(A)) was acquired with an infrared camera (FLIR Model T300). The centerline and the edge temperatures of the cold surface were found to be $T(0,0) = 40\,°C$ and $T(0,25.4) = 38.73\,°C$ based on three repeat tests. The thermal image of the hot end (in contact with the based heater, Figure 3.11) was taken right after the hot face was quickly removed from the test fixture (Figure 3.16(B)). Based on three repeat experiments, it was found that $T(101.6,0) = 115\,°C$ and $T(101.6,25.4) = 109.92\,°C$. The estimated centerline temperature of the hot end was verified by the thermocouple measurements, and was found to be in good agreement with the image results.

The heat transfer coefficient h in the third boundary condition, Equation 2.32, was selected to match the measured TOFs and the surface temperatures acquired by four thermocouples shown in Figure 3.11. Figure 3.16(C) shows the temperature distribution in the waveguide obtained with $h = 14$ W/(m^2·K). The centerline temperature distribution, $T(z,0)$, was used in the measurement Equation 3.12 to calculate the overall and segmental time of flights of ultrasound echoes. The

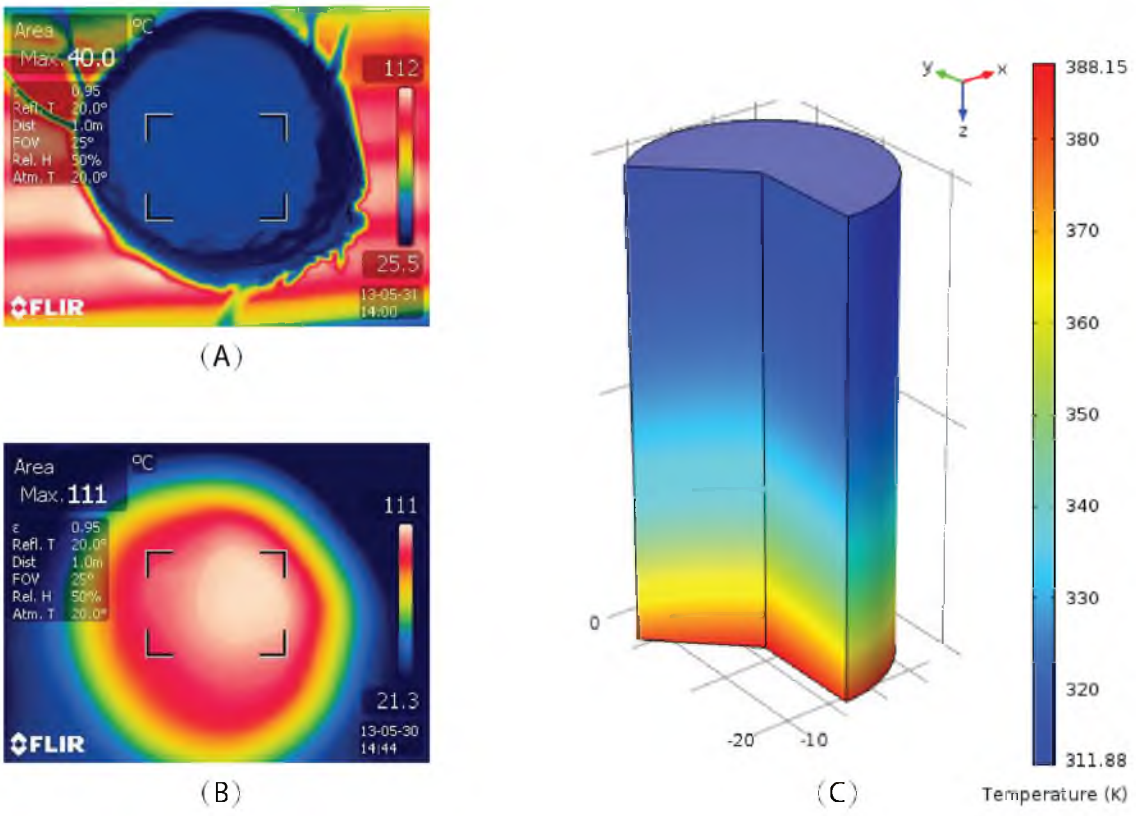

Figure 3.16: Comparison of thermocouple and ultrasound measurements of temperature distribution in the sample heated from the bottom.

comparison of the predictions with the measured values shows less than 1% relative difference for all TOFs. Figure 3.15(B) compares the centerline and surface temperature distributions, $T(z,0)$ and $T(z,25.4)$, with the thermocouple measurements of the surface temperatures. The results show that the centerline temperature is indeed higher than the surface temperature by as much as 7°C, and the difference between the estimated surface temperature and the TC measurements is less than 2°C.

3.4 More Cementitious Samples SOS Measurements

The six cementitious samples that were tested in a temperature controlled water bath for relationship between SOS versus temperature from 20 to 50°C with 5°C increment are summarized in Table 3.1.

During the experiments, all 2-inch samples were fully soaked in water, while

Table 3.1: Summary of cementitious samples for SOS tests

Sample	Height	Cement type	Numbers of interfaces	Curing time for interface (mins)
1	2	Portland I/II	1	15
2	2	Portland I/II	1	60
3	2	Portland I/II + fortifier	1	60
4	2	Rapid Set	1	60
5	3	Portland I/II	2	30
6	4	Portland I/II	3	60

3-inch and 4-inch samples were protruding above the water surface. Only time of flight measurements corresponding to the two sections immersed under water were used to obtain the calibration curve. The echoes from the first and second partial internal reflectors, respectively, were used as delay line reference to measure the time of flight from the immersed sections.

Six sets of randomized tests for samples 1, 2, 5 and 6, and 3 sets for samples 3 and 4 were obtained for determining SOS versus temperature calibration. Figure 3.17 summarizes the speed of sound as a function of temperature results for all samples obtained using the integrated delay line method. The speed of sound of the denser Rapid Set sample is noticeably higher. Overall, as temperature changes from 20 to 50 °C, the speed of sound in all samples linearly decreases by less than 5%, from 2.23% decrease in RS sample to 4.32% decrease in PF sample.

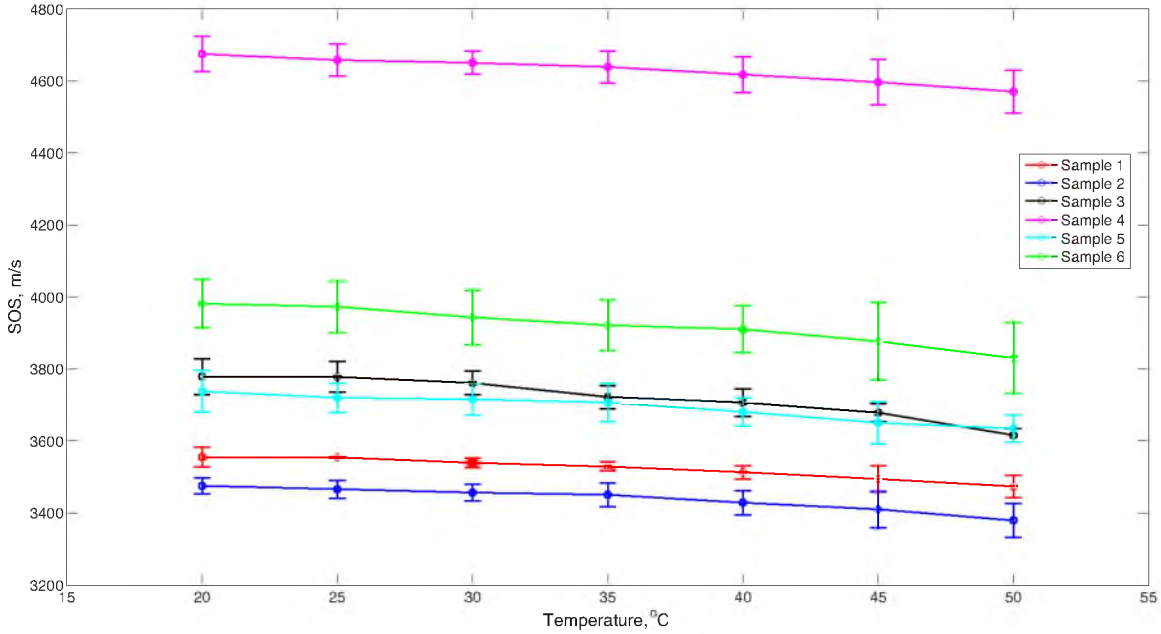

Figure 3.17: The SOS as function of temperature for all six cementitious samples shows linear correlations.

CHAPTER 4

HIGH-TEMPERATURE LABORATORY EXPERIMENTS

4.1 Alumina Refractories

The ultrasound studies with the cementitious sample proved the feasibility of the ultrasound measurements of the segmental temperature distribution method. However, due to the temperature limitation of cementitious material, advanced ceramic that is more resistant to corrosive environment, suitable for elevated temperature application, is required.

Alumina (Al_2O_3) is one of the most widely used general purpose technical ceramics. Alumina ceramic is hard, wear resistant, and has high compressive strength, even at very high temperatures (up to 1750°C). Compared to other oxide ceramics at high temperatures, alumina (Al_2O_3) provides better corrosion protection. Aluminas are also excellent electrical insulators, and can be fabricated with very low porosity and gas tight. Dopants, such as MgO and CaO, may be added to improve its performance characteristics. The result is that the combination of properties exceeds the toughness of pure alumina and improves hardness, strength, and thermal properties that are maintained at high temperatures. These added dopants also slow the growth of alumina grains which is desirable in ultrasound applications.

4.1.1 Castable Alumina

Several castable alumina candidates were tested. GREENCAST®-94 PLUS is a high alumina, low silica castable ceramic, produced by APGreen. Its major ingredients are alumina (94.1% Al_2O_3) and lime (5.1% CaO). This material may be used at a temperature up to 1870°C. We continued to use our vibrating system to help the mixture flow and settle in the molds with minimum voids. However,

the limited liquidity of this mixture caused inevitable air bubbles trapped inside and at the surface of the cured sample. Several issues were encountered with this ceramic. First, the lime appears as small size gravel, about 2–4 mm diameter. These particles scatter and dissipate the ultrasound signal. Second, the ceramic contains fibers, often clumped together, which are normally added to increase the crack resistance, elongation, and thermal shock resistance in ceramic applications. However, clusters of this fibrous material absorb the US energy and limit the length of the ultrasound preparation to below 2 inches under the conditions of our experiments.

To get a better ultrasound signal for this type of ceramic sample, we sieved the large clumps of fiber out of the ceramic mix and crushed down bulky grains. Tests showed that ultrasound signal improved for the modified sample. We were able to measure reflection (return echoes) from 3-inch long samples. Still, the strength of the reflected signal was weak and distorted.

We proceeded to test high-temperature ceramics from Cotronics, Corp. that do not contain fibers or large grains, such as zirconium oxide and alumina oxide castable ceramics. We tried to use the same method to create partial reflection as we used with cementitious materials by cascading ceramic at multiple times with a partial cure allowed after each layer was cast. However, a significant number of air bubbles left inside after drying distorted and weakened the ultrasound echo even after experimenting with different ways of vibrating the mixture.

One example of an ultrasound waveform from 4-inch and 5-inch lab cascade alumina ceramic samples tested using a 1 MHz transducer (Panametrics V302) is shown as Figures 4.1. Because the length of the refractory inserted into the gasifier would be between 4 to 10 inches, we continued to search for the right ceramic material and the proper method to create strong and clear partial reflections.

4.1.2 Machinable Alumina

Recognizing the limitations of our casting process likely contribute to poor quality of samples, the waveguide material that we finally chose was precast, pressure formed, machinable alumina ceramics Rescor 960 with dimensions of 1 inch in diameter and 12 inches in length from Cotronics, Corp. that can be

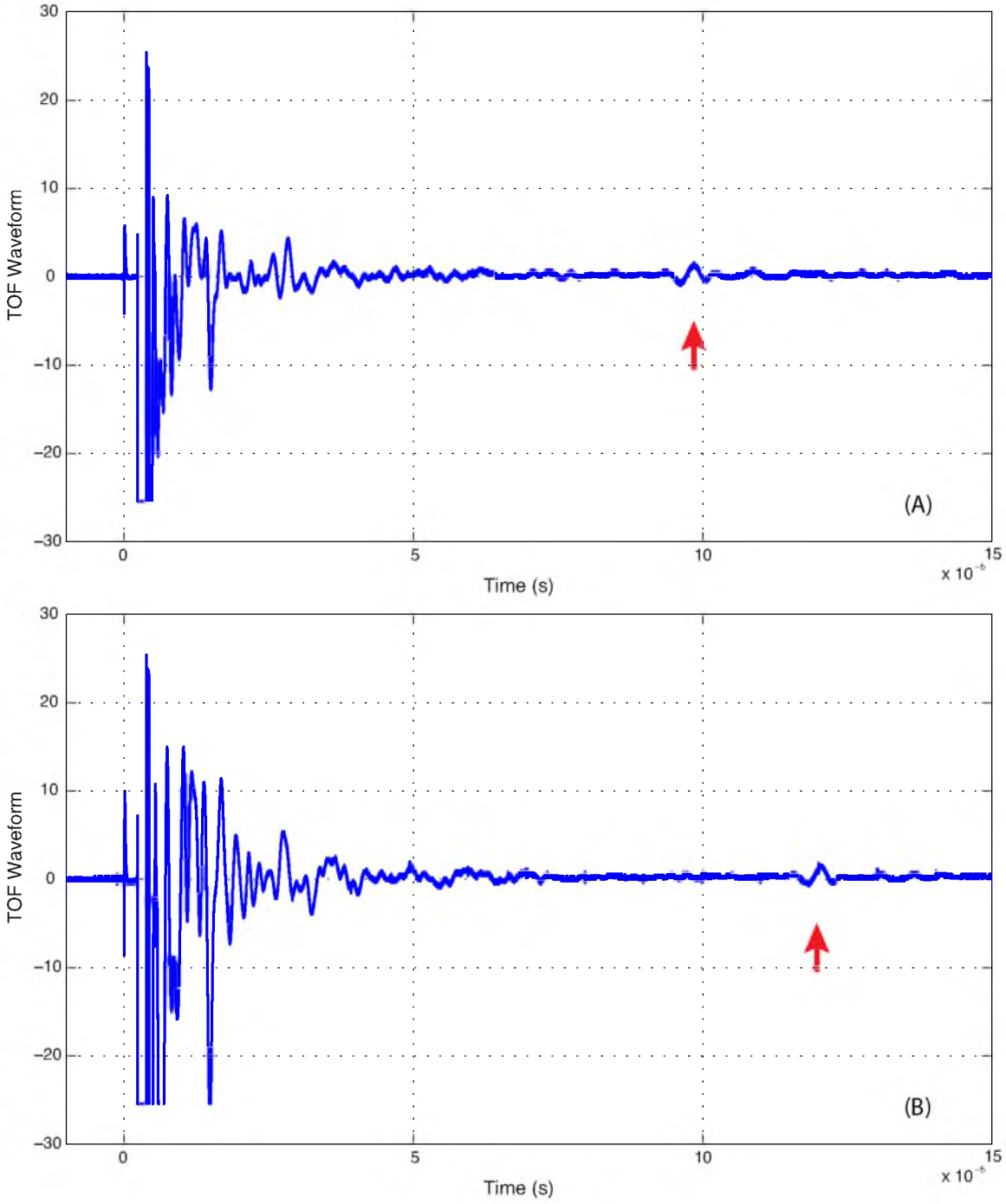

Figure 4.1: The ultrasound waveforms acquired from 4-inch and 5-inch alumina samples. Echo signals are seen at approximately 10 and 12 microseconds.

continuously used at temperatures up to 3000°F (1649°C). This alumina ceramic is particularly suited for our high-temperature ultrasound application due to its low attenuation.

Figure 4.2 shows the ultrasound waveform of the ceramic rod without internal reflectors. The echo from its distal end appears between 140 and 160 μs, followed by multiple echoes. The likely cause of these equally spaced multiple echo signals is multiple internal refractions of the ultrasound signal from the cylindrical surface of the rod, as illustrated in Figure 4.3. This only happens in a cylindrical rod with length significantly larger than its diameter. The reflection at the lateral surface may lead to a small percentage of mode conversion from longitudinal waves to shear waves [13]. Mode conversion of longitudinal to shear waves holds an advantage when the direct introduction of a shear wave is not possible.

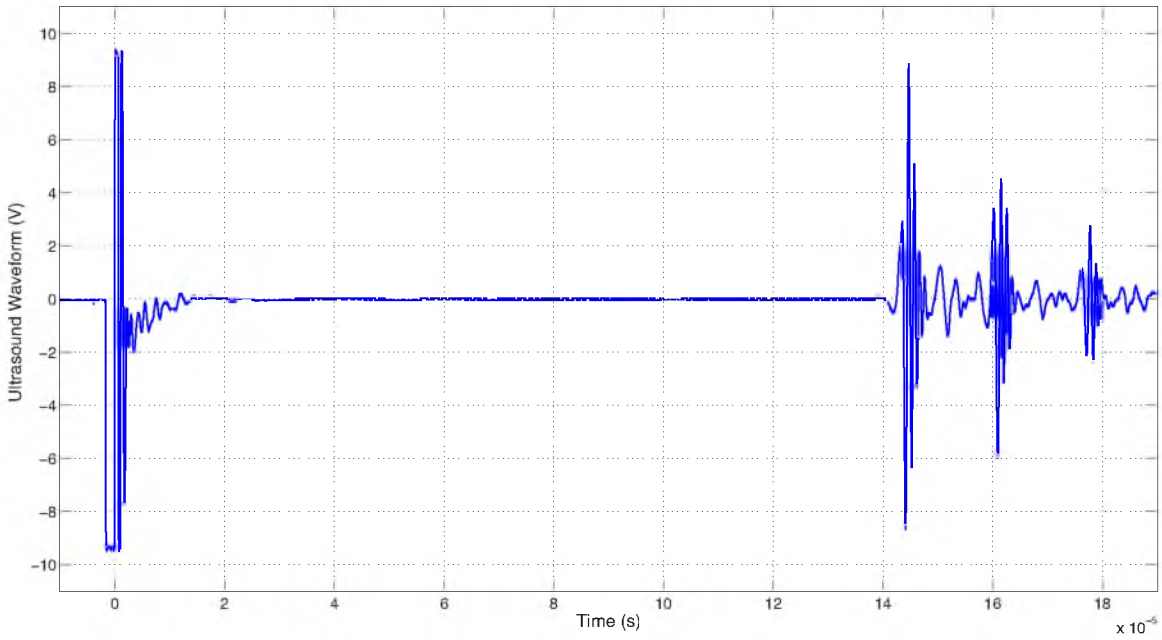

Figure 4.2: The ultrasound waveform for 1-inch × 12-inch alumina rod collected by transducer with frequency 1 MHz. The distal end echo shows between 140 and 160 μs, followed with two more echoes.

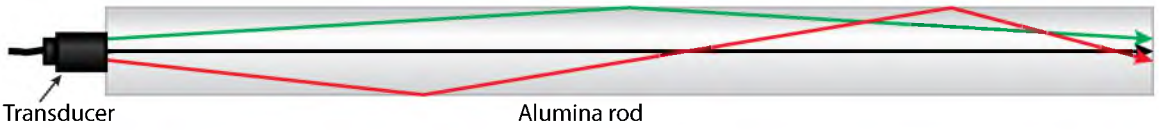

Figure 4.3: Possible modes from longitudinal waves at the lateral surface in the long cylindrical rod of alumina.

4.2 Experiments

4.2.1 Partial Reflectors Structures

After experimenting with different solutions, we found a simple method to create partial ultrasound reflectors from predetermined spatial locations inside the ceramic rod by drilling small holes along its length. To balance the strength of the return signal, which improves with larger hole size, while maintaining physical integrity of the waveguide, three 3/32-inch holes were drilled located 2, 4, and 6 inches from the distal end of the rod to create four segments on this ultrasound waveguide, shown in Figure 4.4.

For high density, high hardness alumina ceramic, ultrasonic testing showed that frequencies in the megahertz regime are necessary to generate wavelengths as small as the microstructure features [16]. We tested this alumina rod at several ultrasound frequencies, including 0.5, 1, 5, and 10 MHz. The results are shown in Figure 4.5. Since the wavelength of 0.5 MHz transducer is ~0.022 m, which is close to the diameter of a 3/32" hole, clear partial reflections from hole locations are not produced due to ultrasound diffraction. The three echoes in the center in Figure 4.5 (b)–(d) are partial reflections from the three drilled holes. The examination of the results of Figure 4.5 indicates that 1 MHz and 5 MHz transducers produced acceptable response. A 5 MHz transducer produced the cleanest echo signal with the best SNR. A 10 MHz transducer has higher spatial resolution but shows higher attenuation of the ultrasound signal.

Figure 4.4: Three 3/32-inch holes were drilled into the precast alumina rod at 2, 4, and 6 inches away from the distal end of the rod.

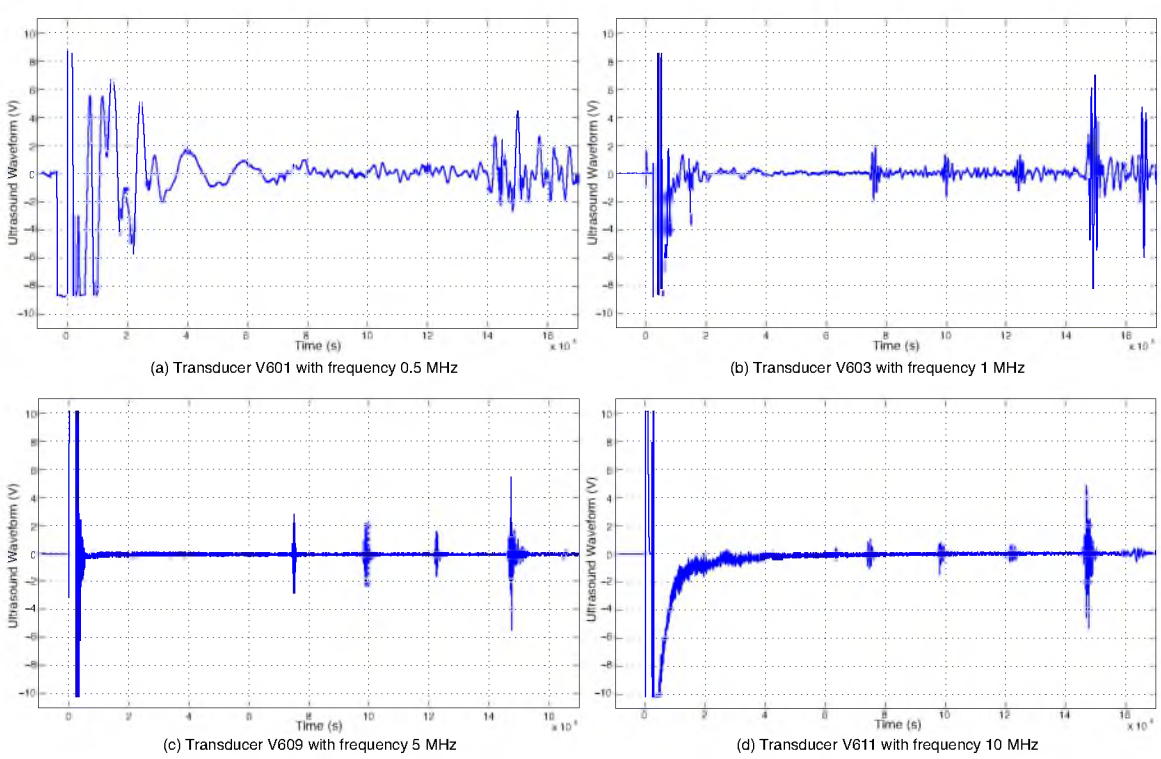

Figure 4.5: The ultrasound echo waveforms for 1 inch × 12 inches alumina rod with drilled holes to produce partial reflections. Plots show the response obtained with transducers of different central frequencies.

Our experiments show that alumina provides good ultrasound propagation at temperatures up to 800 °C for continuous use. It remains an acceptable ultrasound waveguide when temperatures exceed 1000 °C for a short term. However, the strength of the ultrasound signal degrades significantly when temperatures exceed 800 °C for a long time, as occurred during a week-long pilot-scale testing which will be discussed in detail later.

4.2.2 Experimental Setup

A Carbolite 1 & 3 Zone Wire-Wound Tube Furnace (model MTF 201) was adapted for laboratory-scale ultrasound system high-temperature tests. This furnace is capable of operating at temperatures up to 1200 °C and provides convenient observation and access to all power and temperature controls. This tube furnace incorporates low thermal mass ceramic fiber insulation for fast response times and rapid heat-up to operating temperature. Furnace controls are built into the support

base, providing convenient observation and access to all power and temperature controls. The three independently controlled heating zones of the tube furnace improve the uniformity of the maintained temperature. Despite this measure, we found that the temperature distribution inside of the heating tube is approximately parabolic, with the peak value in the center of the furnace and decreasing towards the edges. An actual setup of the lab-scale ultrasound high-temperature measurement system is shown in Figure 4.6. To improve temperature uniformity, the alumina ceramic waveguide was partially inserted into the furnace and held in place without surface contact with the heating tube. The part of the refractory rod between its distal end and the 2-inch drilled hole/partial reflector was placed in the center of the heating zone (colored in red in Figure 4.6).

During the experiments, the ultrasound transducer was attached to the proximal end of the alumina rod extending outside the furnace; this ensured that the transducer was operating below its Curie point. To reduce radiative heating affecting the transducer, an aluminum radiation shield was placed between the furnace and transducer. Independent temperature measurements were provided

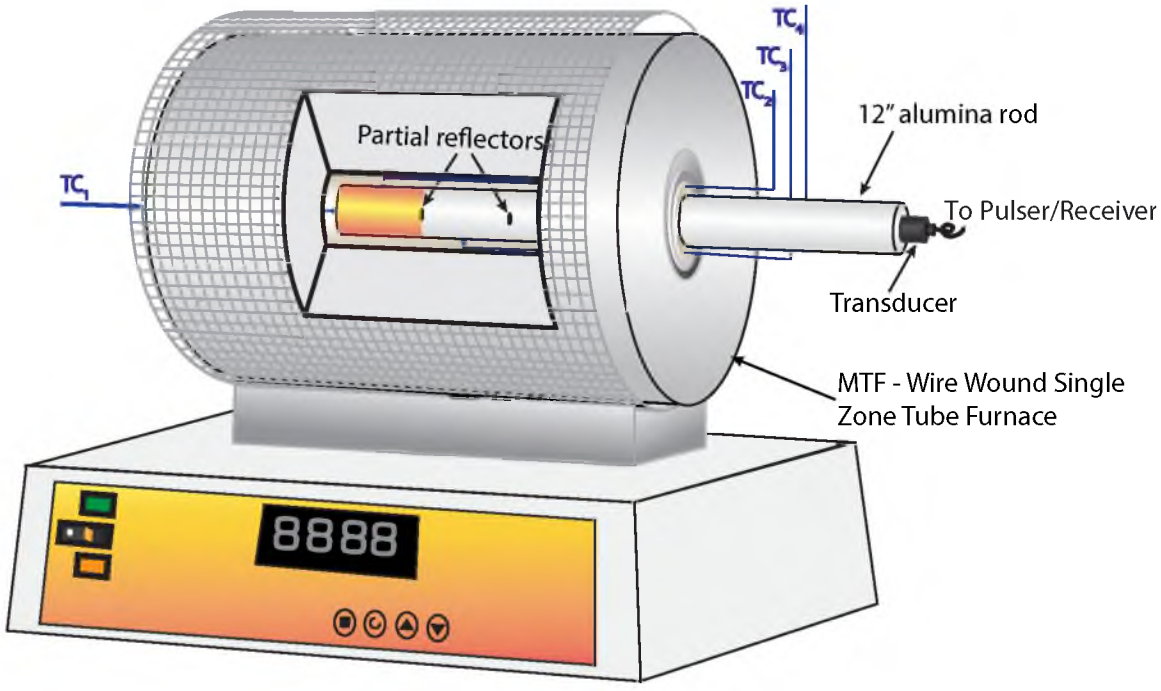

Figure 4.6: An overview of the actual lab-scale ultrasound high-temperature measurement system for SOS versus temperature calibration tests.

by OMEGA® Nextel ceramic insulated thermocouples attached to the hot distal end of the rod glued with ceramic adhesive. Three additional thermocouples were attached between the drilled holes to the side surface of the rod. The ultrasound tests were implemented using a Panametrics pulser/receiver (model 5072PR) and Panametrics transducers (models V609) with a central frequency of 5 MHz. The data were acquired using a Tektronix oscilloscope (model MSO 2024) interfaced to a computer. A customized Matlab code for data acquisition and data analysis was developed and used.

The temperature setpoints were closely spaced in 50 °C increments from 50 °C to 1150 °C and room temperature 20 °C, for the accuracy of the calibration curve. We randomized the sequence of temperatures for the TOF measurements and SOS calculation. The randomization included all 6 repeat experiments for each temperature.

After each change of the setpoint temperature, sufficient time was allowed for thermal equilibration to occur before the ultrasound measurements were performed. To ensure consistency of the TOF measurements, the experiments were repeated with the transducer placed in the same location at the distal end of the sample. To reduce the effect of measurement noises, 16 consecutively acquired ultrasound waveform traces were averaged using a built-in oscilloscope averaging option. The TOF measurements were then used to calculate the SOS for all temperatures at which the experiments were carried out and the 95% confidence interval was established for each data point.

4.3 Results

4.3.1 Signal Processing

The selected alumina ceramic refractory dissipates very little ultrasound energy in the ultrasonic propagation process. Therefore, clear and strong echo signals from the engineered partial reflectors allowed for accurate measurements of the ultrasound TOF at high temperatures. The collected ultrasound waveform for the alumina waveguide is shown in Figure 4.7(A). The echo waveform from the partial internal reflectors, labeled as z_1, z_2, and z_3, and the distal end of the refractory sample, z_{DE}, divide this waveguide to 4 segments, L_1, L_2, L_3, and L_4. The proximal

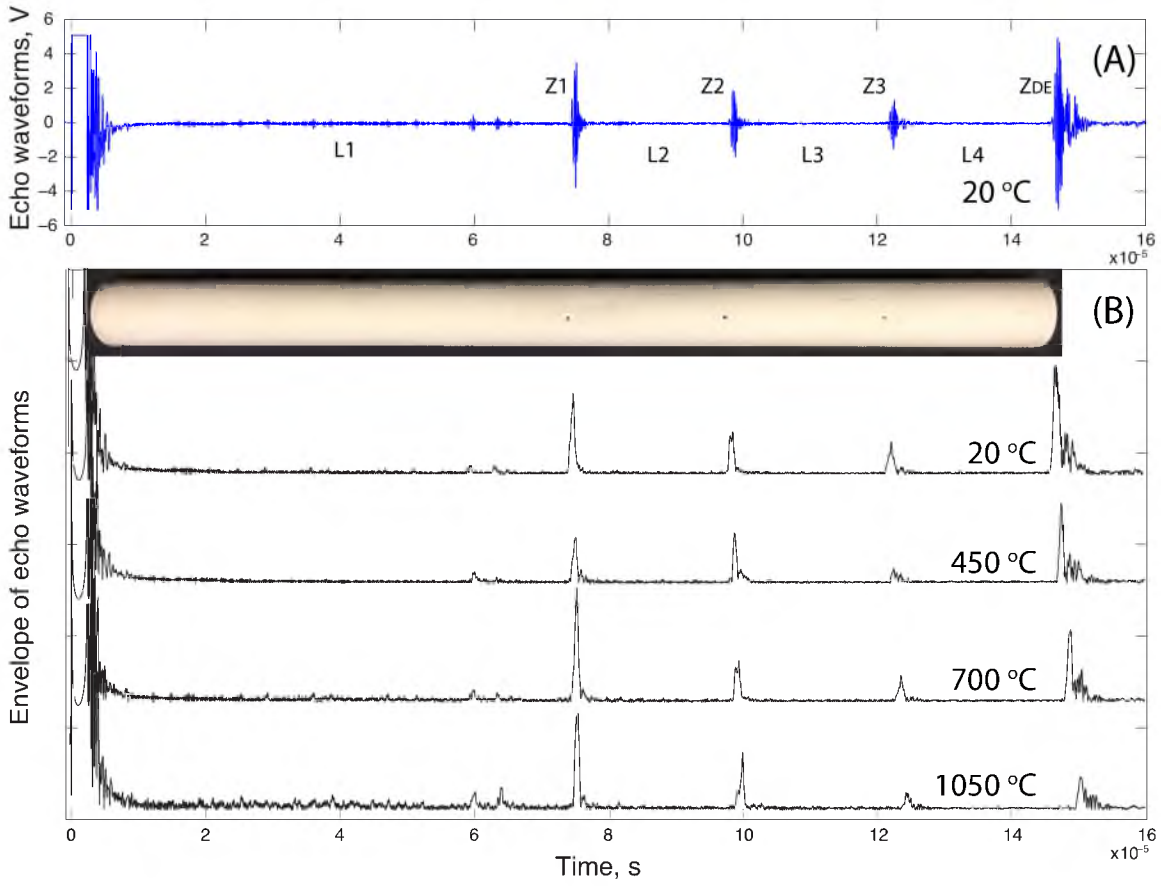

Figure 4.7: The ΔTOF as a function of temperature was calculated by envelope cross-correlation with the reference waveform acquired at 20 °C.

end of the sample, which is the interface between the transducer and the sample, produces the initial bang waveform seen in Figure 4.7 immediately following time $t = 0$. The distance between transducer and partial reflector z_1 was treated as the delay line. This figure shows echo waveforms acquired at 4 different temperatures. The first trace acquired at 20 °C was used as the reference with respect to which the change in the time of flight, ΔTOF, was measured as a function of temperature by performing envelope cross-correlation analysis between the reference waveform and the waveforms obtained at 450 °C, 700 °C, and 1050 °C in the case, shown in Figure 4.7(B). Both cross-correlation and envelope cross-correlation of collected alumina waveform provide consistent TOF measurement results.

The SOS as a function of temperature was calculated based on the measured TOF at a given temperature and the length of waveguide measured at room temperature,

$$c(T) = \frac{2L4}{t_{of_4}(T)} = \frac{2(z_{DE} - z_3)}{\left(t_{of_{DE}}(T_{ref}) - t_{of_3}(T_{ref})\right) + \left(\Delta t^{z_4}_{of_{DE}}(T) - t^{z_3}_{of_3}(T)\right)} \tag{4.1}$$

where L_4 is the distance between the interfaces z_3 and the distal end of the sample z_{DE}, which was measured by a micrometer.

The temperature significantly affects the ultrasonic attenuation. Ultrasound echos' strength at z_3 position degrades when the temperature reaches over 800°C. The high temperature can even make the solid futility for ultrasonic wave propagation. Intraparticle thermoelastic absorption is the major contributor for ultrasonic attenuation in high temperature, which is the combination of the elastic and thermal fields created by the propagation ultrasonic wave [11]. Local changes in temperature are dependent on the thermal expansion coefficient and the direction of the ultrasound propagation. At macroscale range, while regions of the material that are in compression heat up, the regions in rarefaction stay cool. This temperature difference triggers heat flow between the compressed and rarefacted regions to seek thermal equilibrium. This heat flow is irreversible which causes a loss in acoustic energy measured as acoustic attenuation. Zener [110] developed an expression which relates the frequency of maximum attenuation for a single particle to the size of the particle and its thermal properties. This relationship is used as the basis in the derivation of how much energy a single particle absorbs.

$$f = \frac{\pi k}{2\rho C_v r^2} \tag{4.2}$$

where f is frequency, r is particle diameter, k is the thermal conductivity, ρ is density, and C_v is the specific heat at constant volume.

Because of anisotropic properties of alumina grains, where two grains are in contact with each other, there exists a difference in grain orientation, and thermal and elastic properties at such interfaces. Temperature difference also exists between particles, depending on their orientation and degree of anisotropy, which causes another absorption, called interparticle thermoelastic absorption. Portune's work [79] showed that thermoelastic absorption is the dominating absorptive mechanism active in dense polycrystalline ceramics and the effect of heat flow which leads to absorption is irreversible.

4.3.2 The SOS versus Temperature Calibration

Figure 4.8(A) shows in the experimentally obtained relationship between speed of sound and temperature from 20°C to 1150°C that SOS strongly depends on temperatures. Most of the experimental points follow the same trend; only one test result shows large variance at 1150°C. The possible cause of this variance in measurements is the reduced strength of the return echoes observed at high temperatures which is discussed in last section.

The results with and without compensation of the measured SOS for thermal expansion of the rod are presented in Figure 4.8(B). About 75% of measured temperatures have uncertainties less than 1°C and others are between 1 and 2°C for the calibrated results.

The red line in Figure 4.8(B) shows the speed of sound compensated for thermal expansion of the waveguide calculated as

$$c_{TE}(T) = \frac{L_{ref}[1+\alpha(T-T_{ref})]}{t_{of}(T)}, \tag{4.3}$$

where α is the coefficient of linear thermal expansion, which is $4.3\times10^{(-6)}$/°C or $7.74\times10^{(-6)}$/°F for this alumina rod. The length of the ultrasound propagation waveguide and the SOS both change with temperature. For example, if the waveguide were heated by 1000°C, its length would only increase by 0.43%.

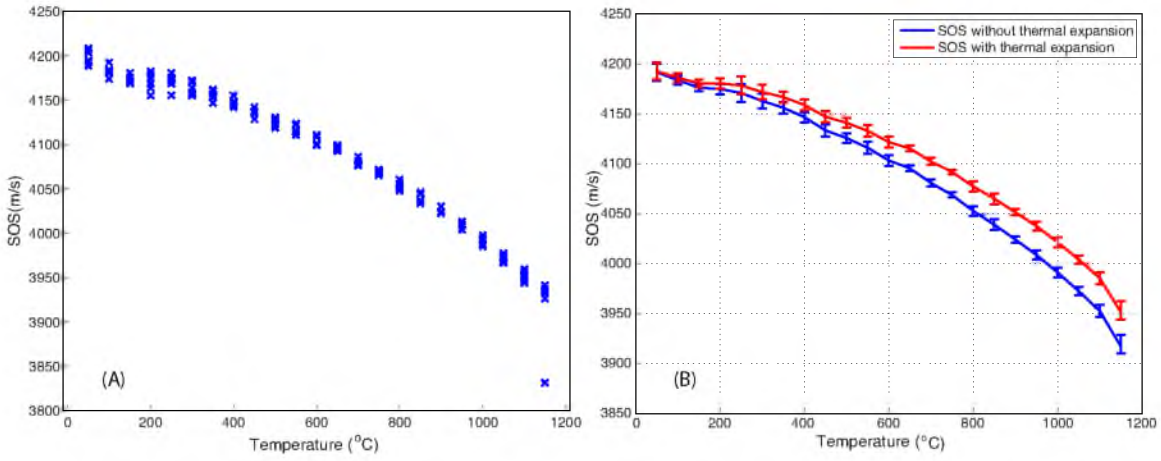

Figure 4.8: The SOS vs. temperature calibration curve obtained for all tested data points using the envelope cross-correlation method is shown in (A). The results in (B) are shown with and without corrections for the thermal expansion. The error bars indicate the 95% confidence interval for each data point.

Though small, it clearly shows the SOS difference in Figure 4.8(B), which would cause temperature error for over 100°C. However, as long as the calibration curve gives the SOS as a function of the temperature without differentiating the two phenomena, there is no practical need to distinguish the degree to which each one of them contributed to the measured change in the TOF with temperature. Therefore, the subsequent discussion will use the SOS versus temperature data without correcting for the thermal expansion.

4.3.3 Elastic Modulus

Moreover, alumina's elastic properties also affect the SOS correlation with temperature. Young's modulus E and Poisson's ratio ν are both functions of temperature. There is research on finding the relationship between Young's modulus and high temperature for ceramics. Ultrasound characterization studies of thermomechanical behavior of refractories [32] and, especially, the measurement of Young's modulus of refractories using the ultrasound [5] showed that the Young's modulus value varies nonlinearly when temperature changes. In addition, this nonlinearity is different for the continuous heating and cooling process [104].

Single grains of alumina exhibit some degree of elastic anisotropy; the ultrasound wave interacts with many differently oriented single grains. But overall, isotropic conditions can be applied and Poisson's ratio can be used. As mentioned before, in long bar mode, the velocity of propagation of the ultrasonic wave through the material is related to E by Equation 2.7, which has been used here to estimate the elastic property of the alumina waveguide. Though the alumina waveguide does not fit the description to apply this equation, in which the waveguide diameter is shorter than a propagation wavelength, the approximation of Young's modulus for our waveguide shows the feasibility of using the ultrasound method for elastic property measurements.

Thus, E may be calculated from measurements of SOS of this long alumina rod and density:

$$E(T) = c(T)^2 \cdot \rho(T) = c(T) \cdot \rho_0(1+\alpha(T))^3, \tag{4.4}$$

where ρ_0 is the density at the reference temperature, α is the coefficient of the ther-

mal expansion, and c as a function of T is given by Equation 4.8. The result of such estimate is shown in Figure 4.9(A), where the constant $\alpha = 4.3 \times 10^{-6}/°\text{F}$ (provided by the manufacturer) and the average value of the SOS at each temperature were used to estimate the Young's modulus. The other elastic properties including the Possion's ratio, shear, and bulk modulus may be obtained from Equations 2.5 and 2.7.

The study of Gault et al. [32] on Young's modulus of three industrial alumina refractories at high temperature shows the similar range of Young's modulus value as our experimental results. Their tested refractories include three, Al_2O_3-MgO castable, Al_2O_3-SiO_2-MgO sintered, and Al_2O_3-ZiO_2-SiO_2 fused-cast, which were performed as the specimen was continuously heated up from room temperature at a rate of 5°C/min. The results of three castable refractories are summarized and compared with our experimental results in Figure 4.9(A), showing a significant decreasing tendency as temperature increases, especially between 200°C and 400°C.

A number of studies on the dependence of Young's modulus on temperature of high purity sintered alumina have been performed and summarized by de Faoite et al. [23] and Wolfenden [105]. In their studies, the Young's modulus versus

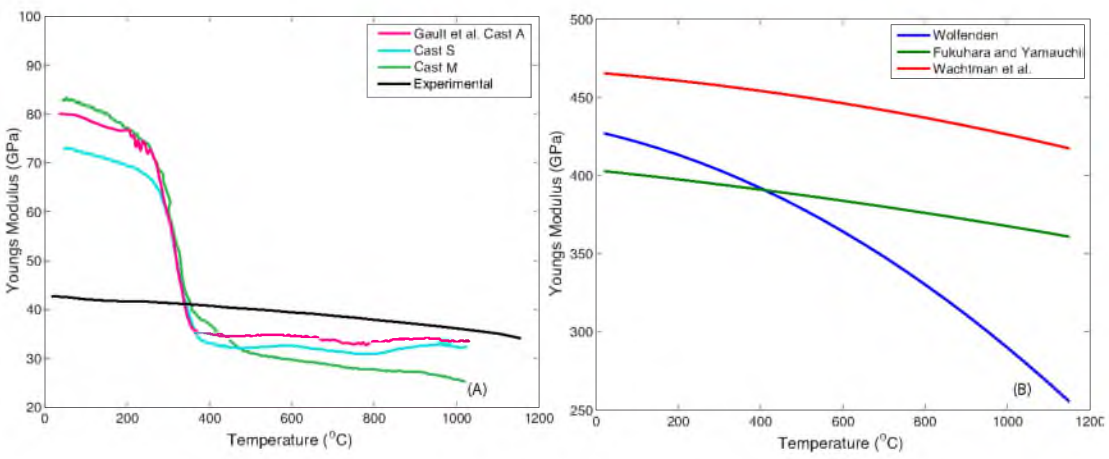

Figure 4.9: The Young's modulus as a function of temperature calculated based on our experimental data is shown in (A) and compared with the data from castable alumina refractories from the Gault et al. study [32]. The Young's modulus for sintered alumina from literature [23], [105] is shown in (B).

temperature has been characterized as a 2nd-order polynomial relationship and is shown in Figure 4.9(B).

All results present a reduction of Young's modulus when temperature increases. A great difference exists between our results and those sintered alumina studies from Gault et al. Our machinable alumina rod does not experience a typical sintering process like typical alumina ceramic. Without the elastic properties at room temperature provided or the information of the manufacturer's procedure, material composition, and grain size distribution due to it being proprietary, we cannot conclude the causes for this large difference in Young's modulus. It has been pointed out that porosity, dopants, composition of ceramic, powder size, and heat treatment method all affect the Young's modulus values for Al_2O_3 [23], [54]. Figure 4.10 reveals the evolution of Young's modulus of elasticity (normalized to room temperature value E_0) as a function of the temperature for the sintered alumina material from the literature and our experimental results. Our experimental result shows an accordant trend with the data of Fukuhara and Yamauchi and Wachtman et al., while Wolfenden's study presents a stronger dependence on

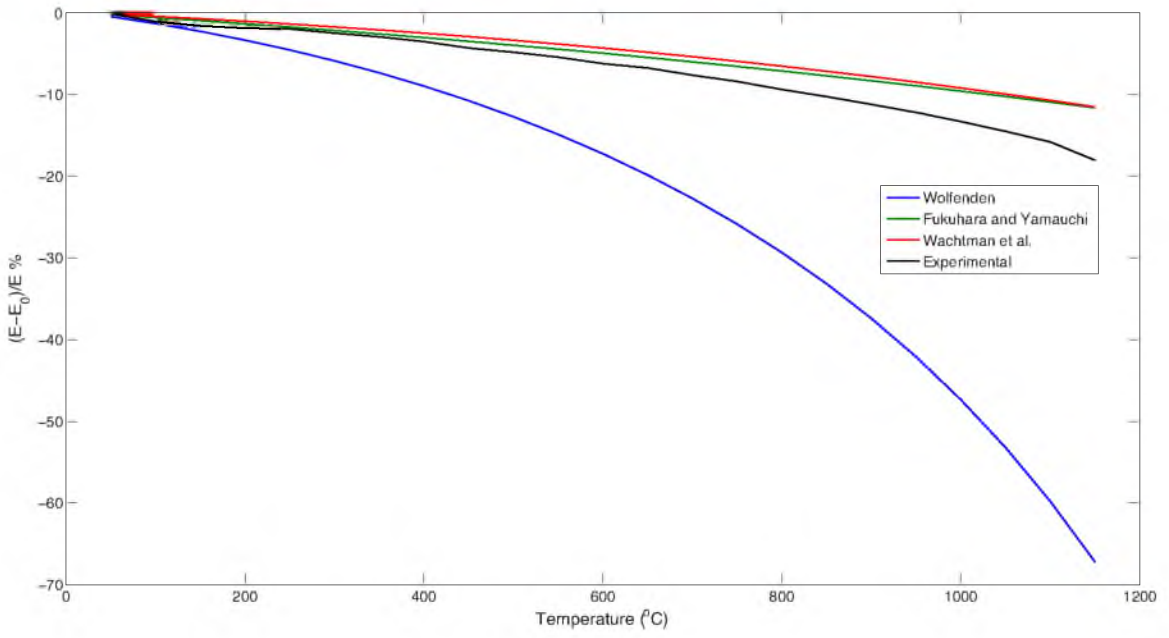

Figure 4.10: The Young's modulus of elasticity (normalized to room temperature value E_0) as a function of the temperature for our experimental results and the sintered alumina material from the literature [23], [105].

Young's modulus on temperature.

If the Young's modulus, Poisson's ratio, density, and thermal expansion are known as a function of temperature, Equation 2.5 would simplify the process of obtaining SOS versus temperature. The verification and correction of SOS can be done by applying experimental measurements as randomized temperature points.

4.3.4 Scaled Calibration

Heyman et al. [42] indicated that for different steels, it is typical to see a 1 percent decrease in the speed of sound for every 100 °C temperature increase. Using this observation, we hypothesizes that, perhaps, the equal percentage model may be an appropriate expression for the experimentally observed SOS versus temperature dependence for the alumina ceramic. Having such a model is beneficial as it would allow us to rapidly adjust our calibration results for the variability of waveguides. Thus, we selected the following functional form for the SOS versus temperature relationship:

$$\widetilde{c} = a - R^{(\widetilde{T}-b)}, \tag{4.5}$$

where a and b must be found to provide the best agreement with the experimental data, and $\widetilde{c}$ and $\widetilde{T}$ are normalized to change between 0 and 1:

$$\widetilde{c} = \frac{c(T) - c_{min}}{c_{max} - c_{min}}, \tag{4.6}$$

and

$$\widetilde{T} = \frac{T - T_{min}}{T_{max} - T_{min}}. \tag{4.7}$$

It is easy to confirm that the selected functional form indeed gives the constant percent change in $\widetilde{c}$ for the given change in $\widetilde{T}$. After obvious manipulations, we obtain that

$$c(T) = c_{min} + (a - R^{(\widetilde{T}-b)})(c_{max} - c_{min}), \tag{4.8}$$

where c_{min} and c_{max} correspond to the speed of sound at the opposite end of the experimental conditions for which the data were obtained (T_{max} and T_{min},

respectively). After the unknown coefficients a and b were found by fitting the experimental data to the selected functional form, we obtained that

$$\widetilde{c} = 1.172 - 4.907^{(\widetilde{T}-0.943)}. \tag{4.9}$$

Comparison of the obtained model with experimental results, shown in Figure 4.11, indicates an excellent agreement, with the coefficient of determination of 0.999.

We also tested how well the following quadratic model fits the data, seen in Figure 4.11

$$\widetilde{c}(T) = a\widetilde{T}^2 + b\widetilde{T} + c. \tag{4.10}$$

The coefficients of a, b, and c of the polynomial model were found using least squares regression, giving the following correlation:

$$\widetilde{c}(T) = 0.807\widetilde{T}^2 - 0.123\widetilde{T} + 0.982, \tag{4.11}$$

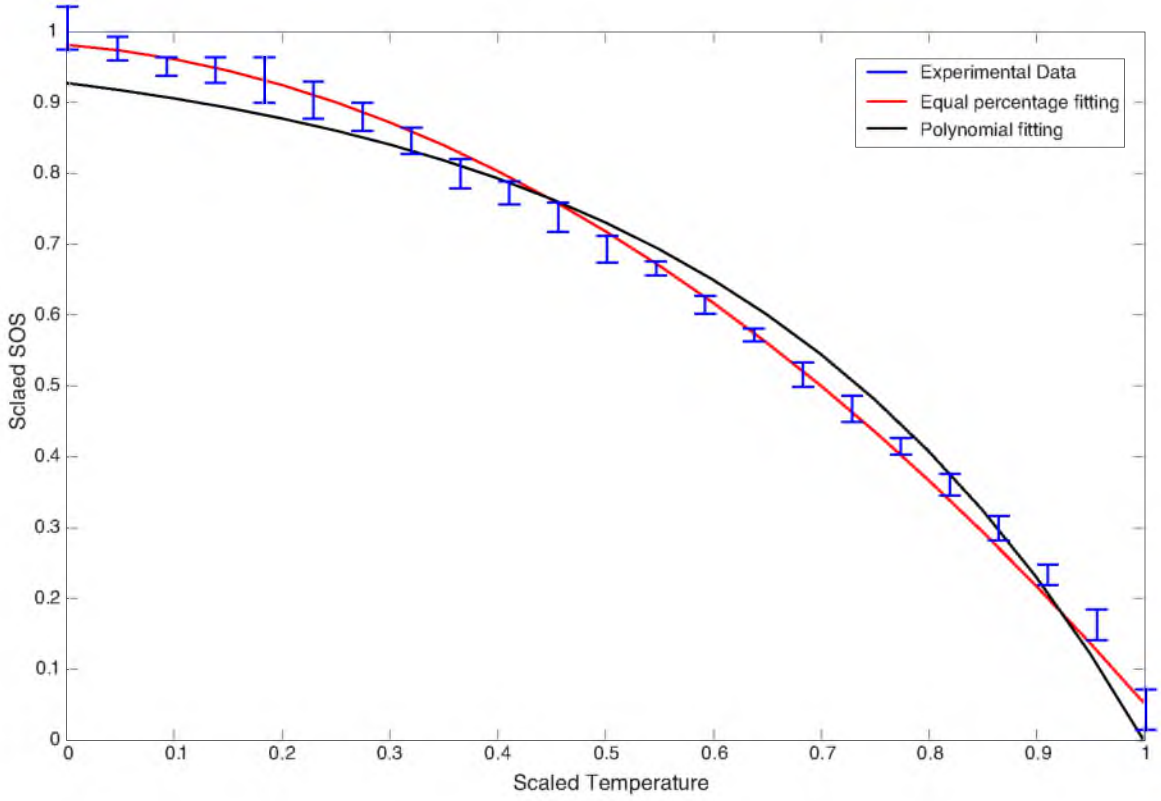

Figure 4.11: Both equal percentage and polynomial fitted results of SOS as a function of temperature in high temperature range are compared with experimental data. Equal percentage fitting has a better coefficient of determination.

with the goodness of fit characterized by $R^2 = 0.97$—a somewhat less accurate agreement than the equal percentage model. Also note that the equal percentage model depends only on two empirical parameters compared to three parameters used to fit the polynomial model.

4.3.5 Nonuniform Temperature Experiments

The overall experimental setup used during nonuniform high-temperature experiments is adjusted from the uniform temperature setup, shown in Figure 4.12. Only the part of the rod between z_3 and z_4 was placed inside of the heating zone (colored in red in Figure 4.12). The part of the ceramic rod outside of the furnace was covered with layers of fiberglass insulation to reduce the heat loss; others were kept the same as uniform temperature tests.

Thermocouples still provided independent temperature measurements attached in the middle of partial reflectors on the surface of the rod and also at the hot distal end, as depicted in Figure 4.12. A surface thermocouple was still used to ensure the temperature close to the ultrasound transducer was within the limit of its safe operation. The data acquisition and analysis system was kept the same as uniform

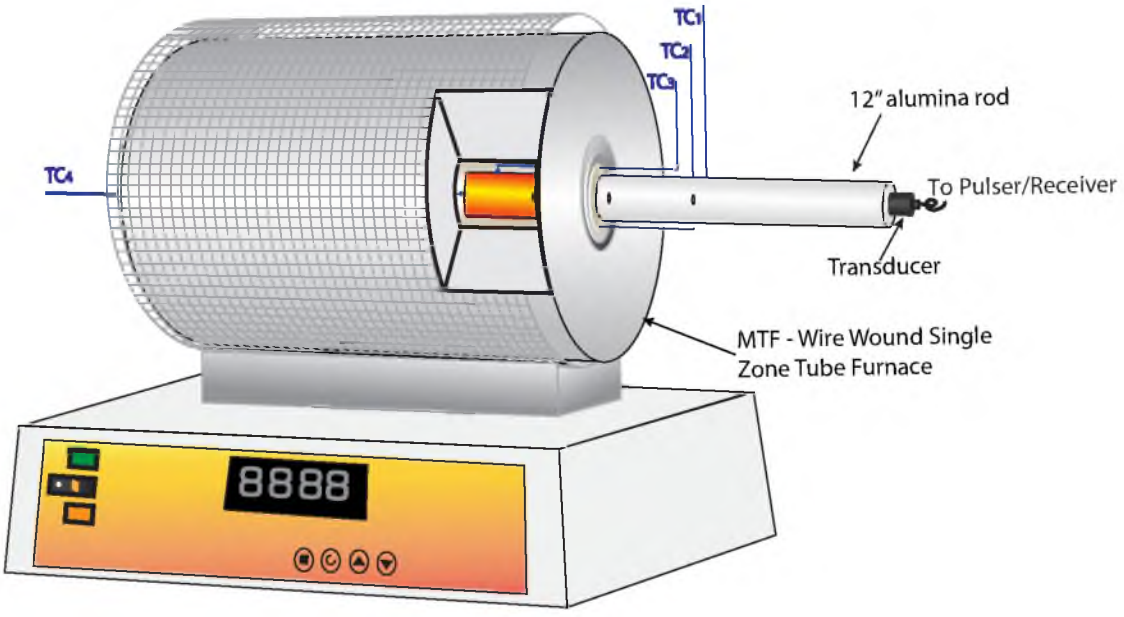

Figure 4.12: The experimental setup for nonuniform temperature distribution using US-MSTD system.

temperature tests.

Two different temperature sets of experiments were tested, 500 and 1000°C, in randomized order, with three repeats for each set temperature. All measurements were performed after the sample reached steady state temperature. The temperature measured by the thermocouple inside the oven deviated substantially from the setpoint specified to the furnace controller (~ 400°C measured versus 500°C setpoint and ~ 880°C measured versus 1000°C setpoint). To ensure consistency of the TOF measurements, the experiments were repeated with the transducer placed in the same location at the proximal end of the sample.

4.3.6 Nonuniform Temperature Results

When temperature along the ultrasound propagation path is nonuniform, the TOF in the i-th segment between the consecutive partial reflectors depending on the temperature distribution is:

$$t_{of_i} = t_{of}^{z_i} - t_{of}^{z_{i-1}} = 2\int_{z_{i-1}}^{z_i} \frac{1}{f(T(z))} dz. \tag{4.12}$$

The first segment between the z_1 and the proximal end of the waveguide was used as the "delay line". Thus, the temperature profile in this segment is not calculated. By using the delay line, we avoid difficulties of extracting the reference "zero" time from the initial bang waveform seen in Figure 4.13 immediately after $t = 0$.

As an initial attempt for the case of high temperatures and for simplicity of calculations, we assumed the piecewise constant temperature distribution for this nonuniform temperature test. This simple assumption, followed by a more realistic, piecewise linear approach was also used for temperature profile estimation.

4.3.6.1 Piecewise Constant Temperature Distribution

The time of flight of the ultrasound propagation through the i-th segment can be calculated as

$$t_{of_i}(T) = \frac{2(z_i - z_{i-1})}{c_i(T)}, \tag{4.13}$$

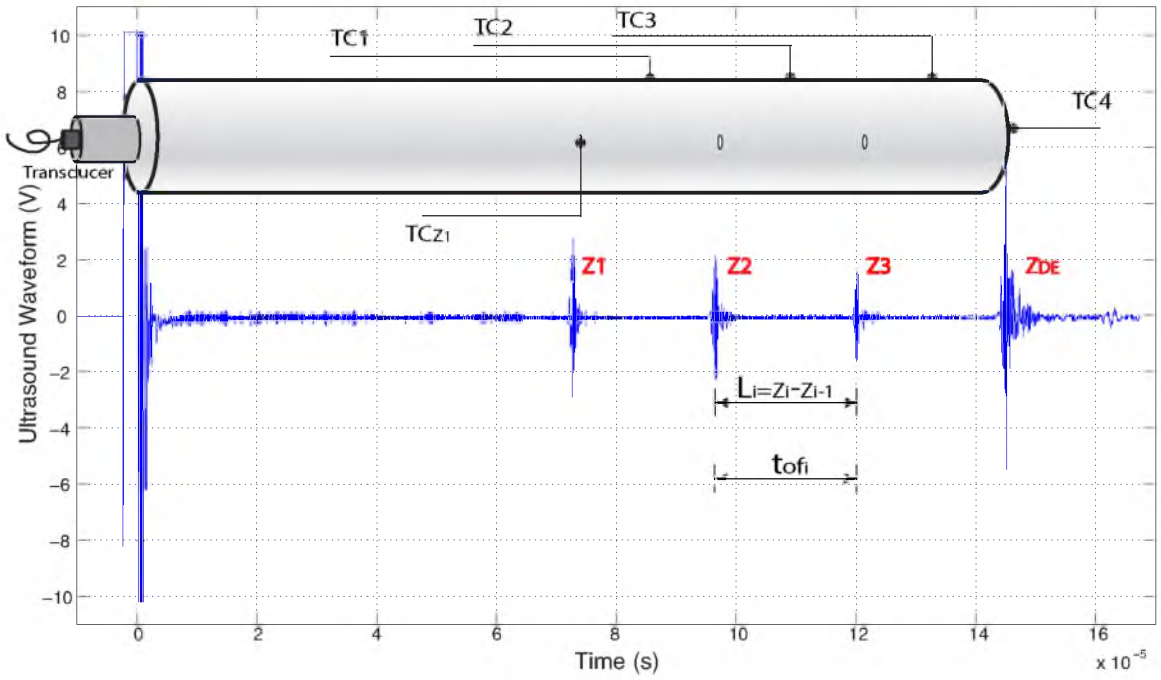

Figure 4.13: The illustration of calculation of TOF in the *i*-th segment for determination of nonuniform temperature distribution.

where distance between z_i and z_{i-1} is the length of the *i*-th segment. Using typical waveforms acquired with the selected waveguide, Figure 4.13 illustrates the calculation of the TOF in the *i*-th segment.

Based on the calibrated relationship between the speed of sound and temperature, Equation 4.5, we have the following expression for the SOS in the *i*-th segment of the waveguide:

$$c_i(T) = c_{min} + (a - R^{(\frac{T-T_{min}}{T_{max}-T_{min}} - b)})(c_{max} - c_{min}), \tag{4.14}$$

or

$$c_i(T) = c_{min}\left[1 + \alpha - \beta R^{\frac{T}{\varphi}}\right], \tag{4.15}$$

where

$$\varphi = T_{max} - T_{min}, \tag{4.16}$$

and

$$\alpha = \frac{a(c_{max} - c_{min})}{c_{min}}, \tag{4.17}$$

$$\beta = \frac{(c_{max} - c_{min})}{c_{min} R^{\left(\frac{T_{min}}{\varphi} + b\right)}}. \tag{4.18}$$

The relationship between the measured TOF of two consecutive echoes and the temperature in the piecewise constant temperature of the corresponding segments is then given as

$$\begin{aligned} t_{of_i}(T) &= \frac{2\left(z_i(T) - z_{i-1}(T)\right)}{c_i(T)} \\ &= \frac{2L_i}{c_{min}\left[1 + \alpha - \beta R^{\frac{T}{\varphi}}\right]}, \end{aligned} \tag{4.19}$$

from which, the temperature is the only unknown. Solving this equation, we have the "average" temperature at the i-th segment:

$$T_i = \varphi \frac{\ln\left(1 + \alpha - \frac{2L_i}{c_{min} t_{of_i}}\right) - \ln\beta}{\ln R}. \tag{4.20}$$

Therefore, the temperature distribution in each defined segment along the ultrasound propagation waveguide can be calculated from Equation 4.20 based on its corresponding TOF.

4.3.6.2 Piecewise Linear Temperature Distribution

For the temperature estimation with piecewise linear assumption, temperature in the i-th segment is computed as

$$t_{of_i}(T) = 2\int_{z_{i-1}}^{z_i} \frac{1}{f(T(z))} dz. \tag{4.21}$$

In addition, the temperature along the propagation waveguide has to be continuous. Thus, we have the following constraints to express the temperature profile in the i-th segment

$$T_i = m_i z_i + n_i. \tag{4.22}$$

When all three segments from L_2 to L_4 are considered simultaneously, we have a total of 6 unknown coefficients. The interface of the two consecutive segments defined by coordinates z_1, z_2, and z_3 introduces the following constraints on the values of unknown coefficients:

$$m_{i-1} z_{i-1} + n_{i-1} = m_i z_{i-1} + n_i. \tag{4.23}$$

Therefore, the TOF in any given i-th segment is calculated as

$$t_{of_i}(T) = \int_{z_{i-1}}^{z_i} \frac{2}{c_{min} + \left(a - R^{\left(\frac{m_i z + n_i - T_{min}}{T_{max} - T_{min}} - b\right)}\right)(c_{max} - c_{min})} dr \tag{4.24}$$

$$= \frac{2\left((T_{min} - T_{max})\ln\left(\left(a - R^{\left(\frac{b(T_{min} - T_{max}) - T_{min} + m_i z + n_i)}{T_{max} - T_{min}}\right)}\right)(c_{max} - c_{min}) + c_{min}\right) + m_i z \ln R\right)}{m_i \ln R(a(c_{max} - c_{min}) + c_{min})}\Bigg|_{z_{i-1}}^{z_i} \tag{4.25}$$

By using these constraints, the TOF measurements for each segment, and the thermocouple measurements of the temperature at z_1 location of the alumina waveguide, we have sufficient conditions to calculate all unknown coefficients m_i and n_i, which determine the piecewise linear temperature distribution in the sample. The calculated temperature results are shown in Figure 4.14, which provides the comparison with the estimated temperature distributions obtained with previously piecewise constant, linear parameterizations, and independent thermocouple measurements.

Ultrasound temperature measurements show a similar trend to thermocouple results. Our initial assumption that the temperature changes as a piecewise constant function, while the simplest possible, is clearly not realistic. A substantial

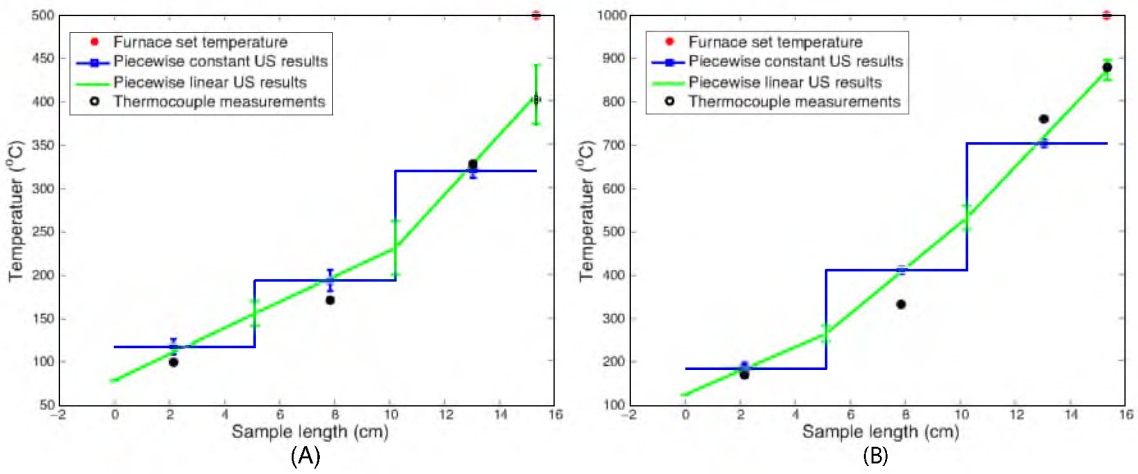

Figure 4.14: Nonuniform temperature distribution at steady state. Central temperatures from ultrasound measurement compared with thermocouple measurements at the refractory surface when furnace temperature is set to 500°C, (A) and 1000°C, (B).

improvement in the accuracy of ultrasound temperature measurements is shown when using a more pragmatic piecewise linear assumption about the temperature distribution in the waveguide. Piecewise linear results have a higher error bar than piecewise constant results, because the piecewise linear method is more sensitive to the variation of TOF values.

Though the alumina rod outside of the furnace was insulated by fiberglass insulation, unavoidable strong temperature gradients are shown for all three temperature profiles. We also notice that the temperature at segment L_3 estimated from both piecewise constant and piecewise linear assumption is higher than the results from thermocouple measurement, especially for the 1000°C setting. This is because the ultrasound method gives the temperature distribution along the centerline of the alumina propagation waveguide, while the thermocouple measurements were taken on the waveguide's surface, shown in the thermocouple measurement in Figure 4.14.

4.3.7 Real-Time Nonuniform Temperature Distribution

A continuous temperature profile monitoring test has been implemented using the US-MSTD system. We added one more hole—the same size as the other three, in the middle of z_3 and z_{DE}, and made the waveguide with temperature monitored into four segments. Four Omega Super OMEGACLAD ® thermocouples were bent at 90° and inserted into the holes, and an OMEGA® Nextel ceramic insulated thermocouple was still attached at the hot distal end to provide independent measurements. The other parts of this experimental setup were kept the same as in the previous nonuniform temperature experiment. The furnace temperature was set at 1200°C, heating from room temperature. After the waveguide temperature reached steady state, the furnace was set down to 700°C, then down to room temperature after the waveguide temperature reached to steady state at 700°C setting.

We developed a Matlab code for the data collection, storage, interpretation, and real-time temperature display. An anisotropic diffusion filter was used with envelope cross correlation method to provide de-noised, numerically stable, and accurate temperature estimation, which will be covered in the next chapter. To

ensure a high sample speed (every 5 seconds per data), assumption of a piecewise constant temperature distribution was applied for all four zones, which is an approximation that simplifies real-time calculations but implies a discontinuous change in the temperature at the interface between the zones. An additional thermocouple was added for the total of five, and their placement was changed to coincide with the location of the four echogenic features, plus a thermocouple attached to the distal end of the waveguide. The ultrasound measurements of the segmental time of flight were acquired continuously, while the thermocouple data were logged only after the setpoint values were reached.

Figure 4.15 shows this real-time nonuniform temperature distribution for all four segments between the hot distal end and first partial reflector z_1 of the alumina waveguide using ultrasound measurements of the segmental temperature distribution method. The result is consistent with the independent thermocouple measurements of the surface temperature, and demonstrates that the developed method can be effectively used to measure temperature distribution in real-time during dynamic transitions over a wide range of operating conditions. The

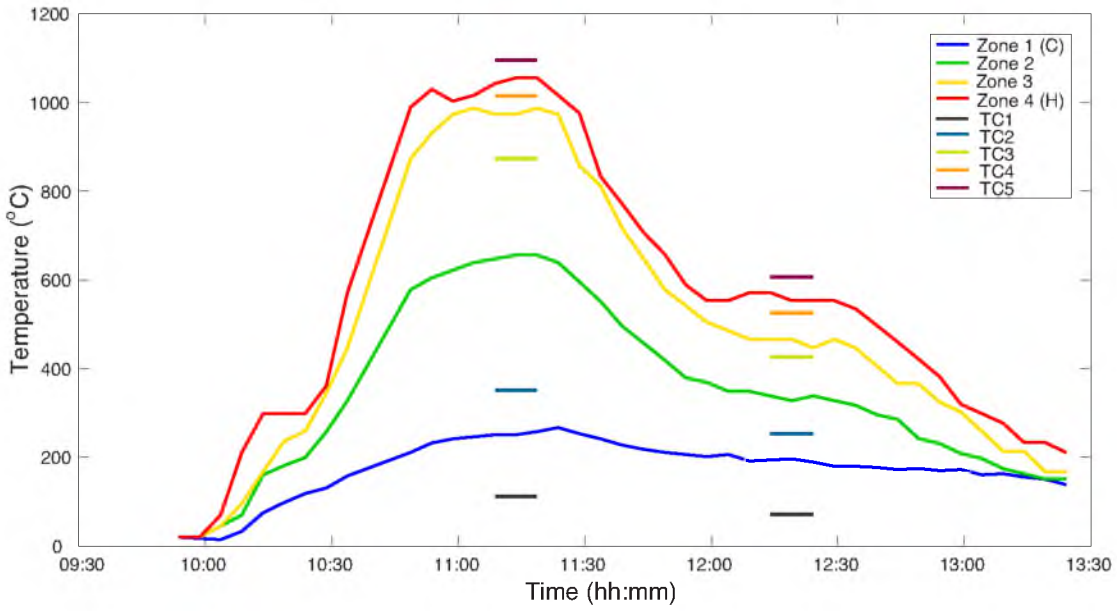

Figure 4.15: Real-time nonuniform temperature distribution monitored by US-MSTD system captured both heating and cooling process tested in lab-scale furnace setup to 1200°C.

ultrasound measurements are sensitive to the entire temperature distribution; they immediately responded to temperature changes like power fluctuations.

4.4 Refractory Degradation Laboratory Tests

We found that thermal cycling did not affect the alumina refractory sample appearance. We have not observed significant erosion of the refractory materials placed for a short time exposure in chemical baths (both base and acid treatments). Longer term refractory testing in a pilot-scale combustor or gasifier would provide additional information about refractory degradation and its effect on the ultrasound propagation. Briefly, short-term chemical degradation tests for refractory samples in laboratory include concentrated alkaline, concentrated acid, and diluted acid treatments. The sample testing in a concentrated solution lasted 24 hours and 60 hours in dilute solutions.

Both GREENCAST®-94 PLUS by APGreen and Rescor 780 by Cotronics castable samples were tested. The Contronics ceramic has a high concentration of Al_2O_3 (about 96%) while APGreen contains some fiber and a fraction of CaO, which appeared as gravels in the dry sample.

Concentrated NaOH (pH 14) and NH_4OH (pH>11) are used as alkaline solutions. The tested samples remained stable after one-day soaking in these solutions, with no surface erosion or reaction observed.

The three concentrated acids used in experiments were H_2SO_4 (98% concentration), HCl (34 38%), and HNO_3 (65%). All acids had pH less than 1. Reaction on the surface of the sample and erosion were observed with samples immersed in any of three acids. The reaction with H_2SO_4 is likely

$Al_2O_3 + 3\,H_2SO_4 \longrightarrow Al_2(SO_4)_3 + 3\,H_2O$.

At room temperature, this reaction occurred very slowly. Rapid reaction was observed when the two samples were exposed to HCl. More than 50% of the soaked APGreen sample has reacted and dissolved within a day of exposure. The likely reason is the rapid reaction of CaO in the APGreen sample with acids. The reaction between Cotronics ceramic and HCl is likely

$Al_2O_3 + 6\,HCl \longrightarrow 2\,AlCl_3 + 3\,H_2O$, and was not as rapid as in the case of APGreen. Reaction between the ceramic samples and HNO_3 was not rapid initially

but eventually consumed more than 30% of soaked samples after a day test. The possible reaction is

$$Al_2O_3 + 6\,HNO_3 \longrightarrow 2\,Al(NO_3)_3 + 3\,H_2O.$$

After testing in concentrated acids, the remaining part of the ceramic samples were tested in weaker acids. Specifically, H_2SO_4, HCl, and HNO_3 were diluted to a pH value of ~4, which is approximately the pH value of the gases inside gasifiers. With diluted samples at room temperature, the tested sample remained stable, with no erosion or reaction observed in laboratory experiments.

The pressure formed alumina ceramic rod is likely to be more stable than the castable sample tested because of its higher density and lower porosity.

CHAPTER 5

ROBUST ULTRASOUND SIGNAL PROCESSING[1]

5.1 The Time of Flight

Accurate measurements of return delays and transmission times are important in many ultrasonic applications, including flaw localization [4], structure thickness and strength measurements [82], range determination [49], measurements of fluid flow rates [69], ultrasound imaging [64], and several biomedical applications [100], [81]. For example, the accuracy of ultrasonic temperature measurements depends on our ability to precisely measure the speed of sound (SOS) in materials [51,91,96], which we usually determine by measuring the time of fight (TOF).

With focus on ultrasound measurements of temperature in this dissertation, and the relationship between the time of flight and temperature, expressed as

$$T = f^{-1}(\frac{2L}{t_{of}}) \tag{5.1}$$

for a solid with known ultrasound propagation distance, accurate TOF measurements are clearly essential for the accuracy of temperature measurements.

5.1.1 Cross-correlation of Waveform

It has been pointed out in previous chapters that the simplest and standard approach to the measurements of the TOF and its changes is to use temporal location of a single-point waveform feature, which is sensitive to measurement noises from instrumentation, environments, and the specimen itself. Our initial approach is by threshold crossing or matching the peak absolute values of the two

[1]©[2014] IEEE. This chapter is adapted, with permission, from [Yunlu Jia; Skliar, M., "Anisotropic diffusion filter for robust timing of ultrasound echoes," Ultrasonics Symposium (IUS), 2014 IEEE International, September/2014]

round-trip echoes. When this method was used to calculate the speed of sound in the aluminum sample, we obtained c_{Al} = 6481 m/s, which is very close to the handbook value. Though this approach is generally successful in low acoustic attenuation samples, we have also found that echo waveforms often tend to be distorted compared to the reference delay line waveform. These two approaches for estimating the ultrasound TOF for its partial reflector and its end of a two-layer cementitious waveguide are shown in Figure 5.1(A) and 5.1(B). The errors of TOF measurements from real values indicate that when broad-band excitations are used, further deterioration in timing accuracy of single-feature methods occurs due to waveform distortions and broadening caused by stronger attenuation of higher frequency content of ultrasound pulses.

When the entire shape of the waveform is utilized in timing, a more robust

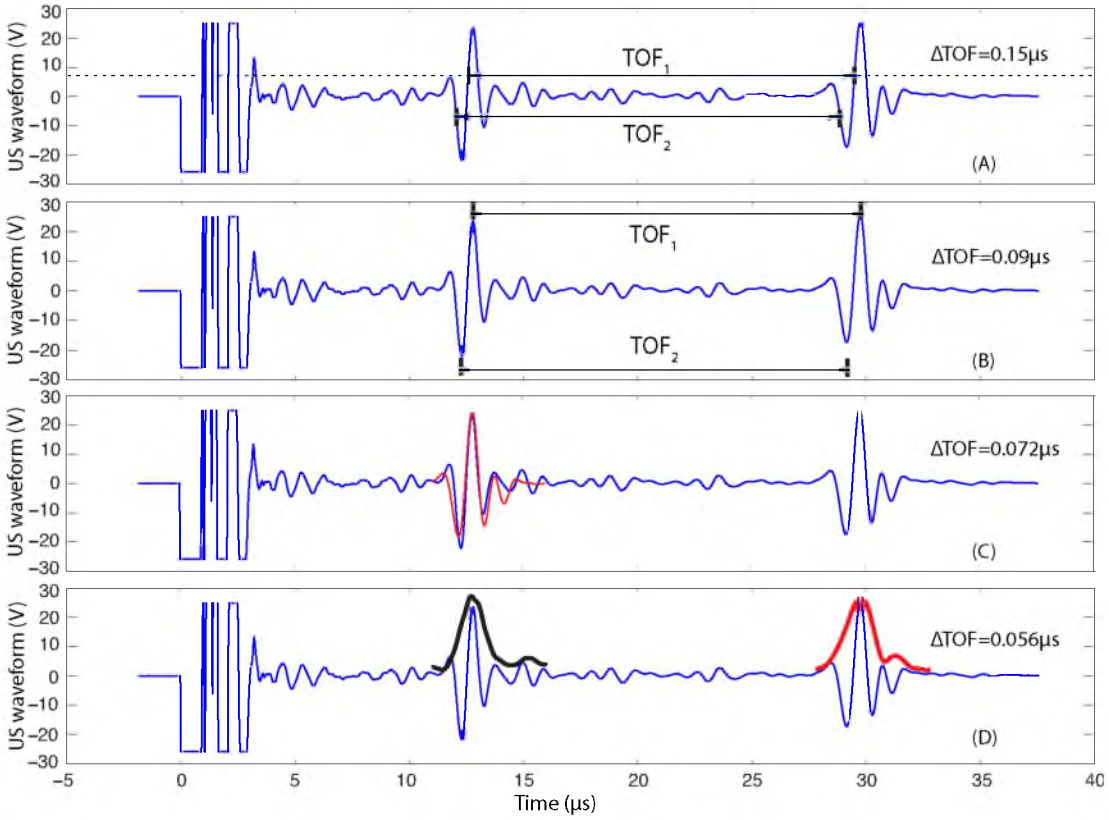

Figure 5.1: TOF estimation for two-layer cementitious sample using threshold crossing (A), peak of the signal (B), cross-correlation (C) and envelope cross-correlation of waveforms (D).

and accurate measurement of t_{of} may be achieved, such as cross-correlation, shape matching methods. In this case, both amplitude and phase information are taken into account [45], which makes timing results less sensitive to measurement noises. The temporal shift is obtained when the best match is found between the waveforms by maximizing their cross-correlation [24], minimizing ℓ_1 and ℓ_2 norms of their difference [50], [75], [101], or by maximum likelihood [20].

Mathematically, the cross-correlation between two signals $f(t)$ and $g(t)$ is represented as:

$$\varphi_{fg} = f \star g(\tau) = \int_{-\infty}^{+\infty} f^*(t)g(t+\tau)dt \tag{5.2}$$

where f^* is the complex conjugate of f and τ is the lag time between two signals. The shift time τ between two signals is determined by maximizing φ_{fg}.

The cross-correlation method for measuring TOF was initially tested with an aluminum standard. The experiments were performed in pulse-echo mode using an immersion transducer with 1 MHz central frequency (Panametrics model V302). In Figure 5.2, the collected ultrasound waveform of the aluminum sample with multiple-trip echoes shows that any round-trip echoes may be used to determine

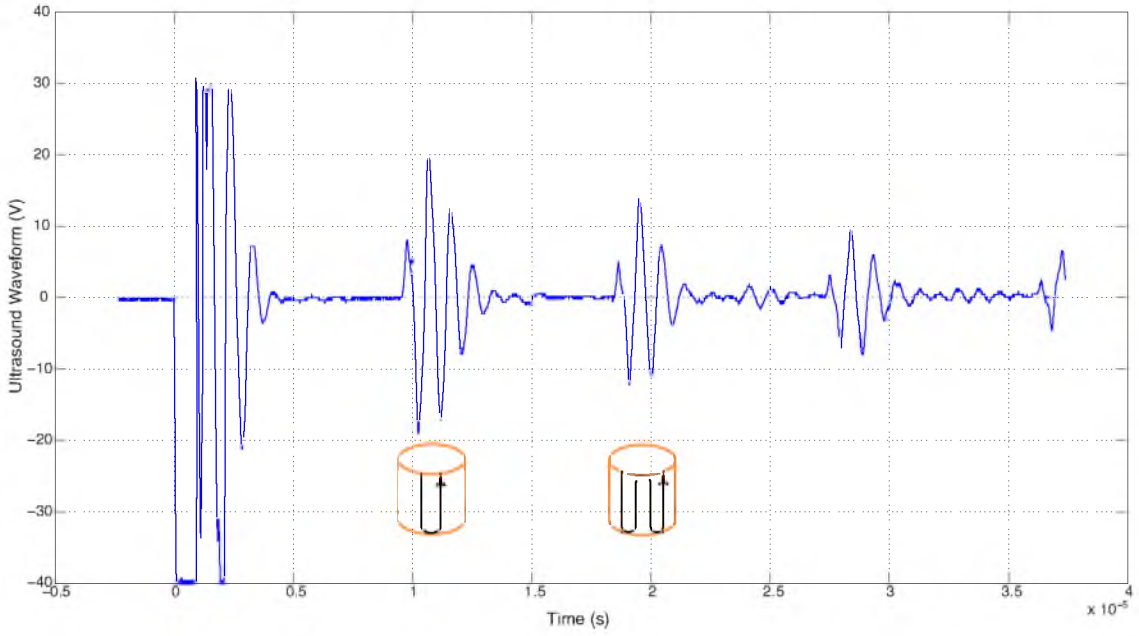

Figure 5.2: Ultrasound test of the aluminum shows multiple echoes corresponding to several round-trip travels of the test pulse through the sample.

TOF by the cross-correlation method. Figure 5.3 gives the result in which the first echo waveform is cross-correlated with the second reflected signal and the two waveforms are then aligned. The shift needed for such an alignment is precisely the value of the time of flight.

However, the cementitious samples are substantially more dissipative compared to metals, so we usually do not have repeated partial internal reflections from the same surface. In this situation, the cross-correlation method as described may not be the best option to apply to the measurements of the TOF. Therefore, our approach is to use the cross-correlation to, first, determine zero reference point correction relative to the trigger time provided by the pulser.

5.1.2 Zero Trigger Reference

Our tests show that the recorded trigger time, which corresponds to the time an electrical pulse is sent to the piezoeletric transducer, is not equal to the ultrasound zero time, which is the instant when the ultrasound pulse starts its propagation through the sample. Our approach is to find the correction to the trigger time in

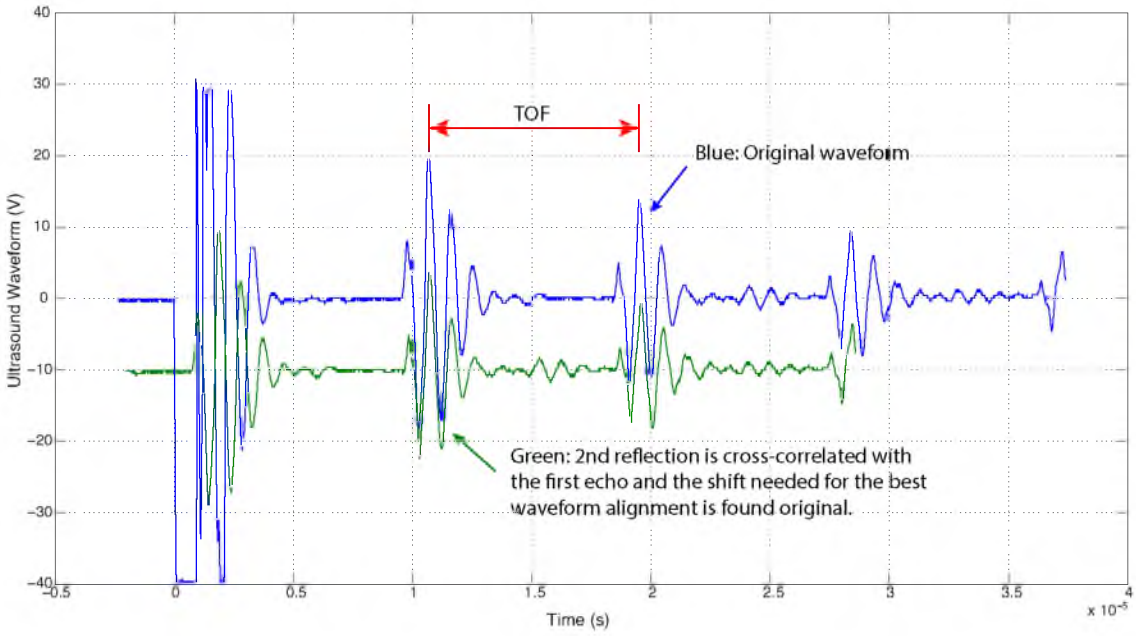

Figure 5.3: The calculated cross-correlation between the first two echoes gives the time shift needed for the best alignment of the two waveforms. This shift is equal to the TOF of the test pulse.

order to obtain a reference time relative to which the TOF will then be determined.

We started by using the cross-correlation method to find the trigger time correction (ultrasound signal delay) for the standard material with low ultrasound attenuation. Figure 5.4 shows the result obtained with the aluminum standard. The red dot on the blue waveform is the starting point of the first echo. By applying the TOF value, previously determined using the cross-correlation method (Figure 5.3), the trigger correction (the signal delay time) is determined to be equal to 91.2 nanoseconds.

To establish if the obtained correction depends on the sample, the experiments were repeated with several other materials, including bronze, stainless steel, steel, and plastic. Results for all tested materials are summarized in Table 5.1 and show that the trigger correction time, equal to the delay between the electrical excitation sent to the transducer and the resulting ultrasound pulse, does not vary significantly with the material of the sample.

This suggests that once the signal delay is determined using the cross-correlation method, it can then be used to identify the zero reference point, which might not

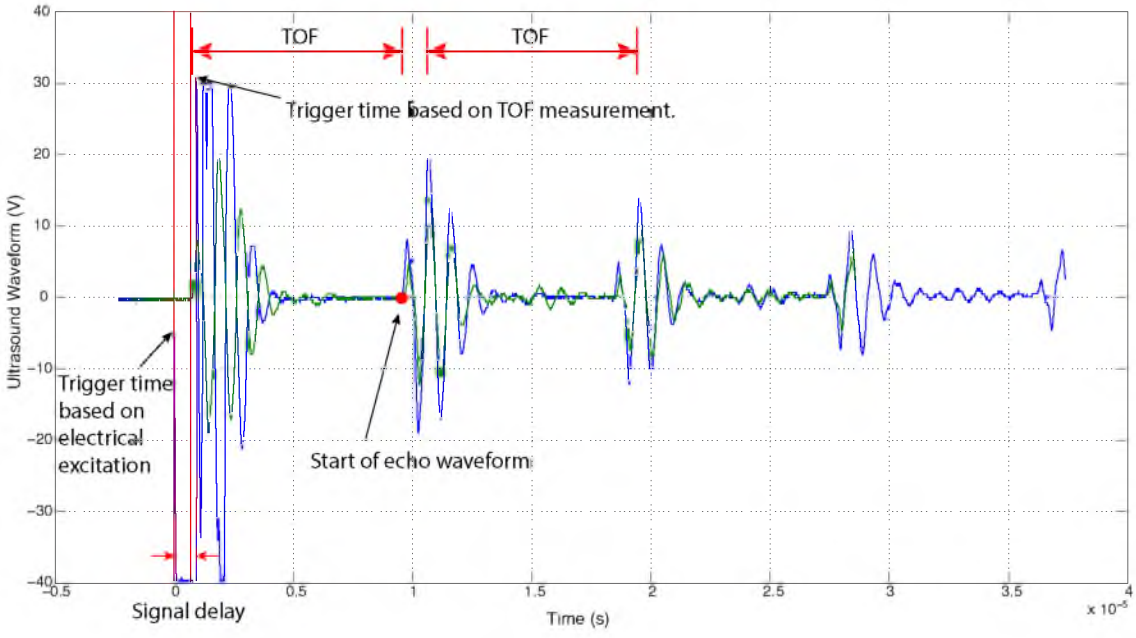

Figure 5.4: The correction of the electrical trigger time is found using the cross-correlation method with an aluminum standard.

Table 5.1: Signal delay after trigger for different materials

Material	Aluminum	Bronze	Stainless steel	Steel	Plastic
Signal delay after transducer trigger (ns)	91.2	96	94.4	94.4	94.4

be suitable for a sample with high acoustic attenuation.

While we observed no/little dependence of the trigger correction on the material of the sample, it is reasonable to expect that the size and design of the transducer may have an effect on the delay in transduction of the electrical pulse into the ultrasound signal. To test this hypothesis, we repeated the described experiment with a different 1 MHz transducer (Panametrics model A114s with 1 MHz central frequency). For the same aluminum sample, the signal delay observed with the A114s transducer is only 25.6 nanoseconds, which is substantially shorter than the transduction delay for V302 transducer.

The possible reason for two transducers with the same central frequency but different trigger delays is its exciting bandwidth. V302 is a vedioscan type transducer, which has a wide broadband unit to optimize for near surface resolution. A114S is an accuscan type transducer with relatively narrow frequency bandwidth units designed for penetration.

5.1.3 Cross-correlation of Envelope of Waveform

Though the cross-correlation method performs better with attenuating materials than single-point timing, the results may still be unacceptable when significant distortion of ultrasound waveforms occurs, as is often the case with dissipative materials (e.g., materials with large grain sizes [28]). For waveform distorting samples, a higher precision can be achieved if the envelopes of the waveforms are used in timing [59], shown in Figure 5.1(C) and 5.1(D) for both cross-correlation methods.

The analytic signal, $s_a(t)$, of a given waveform, $s(t)$, is defined as the following complex function:

$$s_a(t) = s(t) + j\hat{s}(t) \tag{5.3}$$

where $j^2 = -1$ and $\hat{s}(t) = H(s)(t)$ is the Hilbert transform of $s(t)$, which represents the convolution of the original waveform with the function $h(t) = \frac{1}{\pi t}$. The envelope of $s(t)$ is then calculated as an instantaneous amplitude of its analytic signal:

$$A(t) = |s_a(t)| = \sqrt{s_a(t)s_a^*(t)} = \sqrt{s^2(t) + \hat{s}^2(t)}, \tag{5.4}$$

where * is the complex conjugation operator.

Several methods have been proposed to time ultrasound signals (echoes and transmission times) using the waveform envelopes. In [59], the transmission time of ultrasound pulses was measured by using the peak value of the waveform envelope as a reference point. Though this is still a single-point timing method, now based on the features of $A(t)$, it improved the accuracy when compared to timing based on single features of original waveforms (e.g., the first zero-crossing by $s(t)$). The cross-correlation of the envelope of the acquired echo with the envelope of the reference waveform was used in [51]. In the case of dissipative (cementitious) samples, a noticeable improvement was observed with this approach over the results obtained with waveform cross-correlation. A simplified version of cross-correlation of envelopes of waveform for TOF determination is shown in Algorithm 5.1.

Algorithm 5.1 Calculate $offset_t = \text{cross}(sig_1, t_1, sig_2, t_2)$

$ls_1, lt_1 \Leftarrow findintervals(sig_1, t_1)$
$ls_2, lt_2 \Leftarrow findintervals(sig_2, t_2)$
$env_1 \Leftarrow abs(hilbert(ls_1))$
$env_2 \Leftarrow abs(hilbert(ls_2))$
$CF, Lags \Leftarrow xcorr(env_1, env_2)$
$M, loc \Leftarrow max(CF)$
$offset \Leftarrow Lags(loc)$
if $offset > 0$ **then**
  $offset_t \Leftarrow lt_2(1 + offset) - lt_1(1);$
else
  $offset_t \Leftarrow lt_2(1) - lt_1(1 + offset);$
end if

However, in continuous temperature monitoring tests, we observed the unstableness of an enveloped waveform due to signal noise. Therefore, using only

cross-correlation of an enveloped waveform for TOF determination cannot ensure the result's accuracy.

5.2 Anisotropic Diffusion Filter

A new method proposed here uses the results of Perona and Malik [76]. They developed an anisotropic diffusion algorithm for image processing that smooths an image without blurring the edges found within. To achieve this outcome, the original image is iteratively subjected to a diffusion operator with a spatially dependent diffusion coefficient that becomes small on the edges. As a result, the image features away from the edges are smoothed by diffusion, while the diffusion is impeded across the edges to prevent their blurring.

The anisotropic diffusion operator used in the Perona-Malik filter has this following form:

$$\frac{\partial}{\partial \tau} u(\mathbf{r},\tau) = \nabla \cdot [D(\mathbf{r},\tau)\nabla u(\mathbf{r},\tau)], \tag{5.5}$$

$$u(\mathbf{r},0) = I(\mathbf{r}), \tag{5.6}$$

where the initial condition, $I(\mathbf{r})$, that initializes the iterations is the original image, $\mathbf{r} = (x, y)$ defines spatial position within the image, and τ is the ordering parameter that enumerates iteration steps of the discrete implementation of Equations 5.5 and 5.6. The diffusion coefficient $D(\mathbf{r},\tau)$ changes with position and is selected by the designer to decay at the edges. Two common choices that satisfy this requirement include [76]:

$$D_1(\mathbf{r},\tau) = \exp\left(-\left(\frac{|\nabla I(\mathbf{r},\tau)|}{\kappa}\right)^2\right) \tag{5.7}$$

$$D_2(\mathbf{r},\tau) = \frac{1}{1+\left(\frac{|\nabla I(\mathbf{r},\tau)|}{\kappa}\right)^{1+\alpha}}, \quad \alpha > 0 \tag{5.8}$$

where κ is a selected constant. In both cases, the diffusion is small on the edges where the gradient of the grayscale image intensity is high. A proper choice of the diffusion function preserves and even enhances edges (see, for example, [103]) while ensuring numerical stability [12]. Further discussion of the effect of different design parameters on the performance of diffusion filters is found in [99].

The described filter has been used in several ultrasound imaging applications. For example, in reference [46] the anisotropic diffusion was applied to ultrasound strain images; the application of this filter to seismic images is found in [99]. To the best of our knowledge, this approach has not been previously used in timing the arrival of ultrasound waveforms by matching single-point features or shapes of their filtered envelopes.

According to the proposed method, a 1D version of the diffusion filter from Equations 5.5 and 5.6 is iteratively applied to the envelope of the acquired ultrasound waveform:

$$\frac{\partial}{\partial \tau} u(t,\tau) = \frac{\partial}{\partial t}\left[D(t,\tau) \frac{\partial}{\partial t} u(t,\tau) \right] \tag{5.9}$$

$$u(t,0) = A(t). \tag{5.10}$$

The filtering process is initialized with the original envelope $A(t)$, given by Equation 5.4. The discrete approximation of Equation 5.9 is applied iteratively, with each new iteration using the results of the previous step as the initial condition.

The specific approximation of Equation 5.9 used by us during the experimental testing of the method is the same as the one found in [33]:

$$\begin{aligned} \frac{\partial}{\partial \tau} u(t,\tau) \approx & \frac{\partial}{\partial t}[D(t,\tau)\frac{1}{\Delta t}(u(t+\frac{\Delta t}{2},\tau) - u(t+\frac{\Delta t}{2},\tau))] \\ \approx & \frac{1}{\Delta t^2}[D(t+\frac{\Delta t}{2},\tau)(u(t+\Delta t,\tau) - u(t,\tau)) \\ & - D(t-\frac{\Delta t}{2},\tau)(u(t,\tau) - u(t-\Delta t,\tau))] \end{aligned} \tag{5.11}$$

where $\Delta t = 1$ and $u(t-\Delta t,\tau)$, $u(t,\tau)$, and $u(t+\Delta t,\tau)$ are the temporally consecutive values of the filtered envelope obtained at the preceding iteration. We elected to use the diffusion coefficient, D, given by Equation 5.7 because it tends to better preserve high-gradient data segments of the envelopes, which are analogous to high contrast edges in images. After approximating the gradient appearing in Equation 5.7, the following values of the diffusion coefficient are used in Equation 5.11:

$$D(t+\frac{\Delta t}{2},\tau) = \exp\left(-\frac{(u(t+\Delta t,\tau) - u(t,\tau))^2}{(\kappa \Delta t)^2} \right), \tag{5.12}$$

$$D(t-\frac{\Delta t}{2},\tau) = \exp\left(-\frac{(u(t,\tau) - u(t-\Delta t,\tau))^2}{(\kappa \Delta t)^2} \right), \tag{5.13}$$

where the parameter κ was set to 20. The updated value of the filtered envelope after each iteration is obtained by approximating the derivative on the left-hand side of Equation 5.11. For example, by using a simple forward difference approximation, the following update equation is obtained:

$$u(t,\tau+\Delta\tau) = u(t,\tau) + \Delta\tau \cdot rhs, \tag{5.14}$$

where *rhs* is the right-hand side of Equation 5.11 and $\Delta\tau$ is the "discretization" step selected to provide the desired rate of convergence. Algorithm 5.2 performs anisotropic diffusion upon a 1D enveloped waveform.

Algorithm 5.2 Calculate sig_{diff} = anisodiff($sig, iter, \delta t, \kappa$)

$sig_{diff} \Leftarrow sig$
$dx \Leftarrow 1$
$hW \Leftarrow [1\ -1\ 0]'$
$hE \Leftarrow [0\ -1\ 1]'$
for $t = 1$ **to** $iter$ **do**
  $\nabla W \Leftarrow conv(sig_{diff}, hW)$
  $\nabla E \Leftarrow conv(sig_{diff}, hE)$
  $cW \Leftarrow exp(-(\nabla W/\kappa)^2)$
  $cE \Leftarrow exp(-(\nabla E/\kappa)^2)$
  $sig_{diff} \Leftarrow sig_{diff} + \delta t * ((1/dx^2) * cW * \nabla W + (1/dx^2) * cE * \nabla E)$
end for

The described filtering process uses a diffusion coefficient that takes small values when the temporal changes in the envelope are rapid. It acts to sharpen the envelope peaks while maintaining their temporal position over many iterations. The filter blurs small and slow variations that contribute to inconsistency of timing results commonly occurring when dissipative materials are tested. As a result, the timing of ultrasound signals based on the filtered envelopes is expected to be more robust to the presence of measurement noises and distortions. In the following, we put this expectation to the experimental test.

5.3 Experiments and Results

For the two different ultrasound waveguides used in experiments, both materials were dissipative. One sample was obtained by hot pressing high-purity

alumina into a 12-inch long rod with a 1 inch diameter. Four 3/32 inch diameter holes were drilled radially along its length at 1, 2, 4, and 6 inches from the distal end, in Figure 5.5A. The other sample was obtained by self-cascade from cementitious material mixed with water, which showed strong dissipation and attenuation on its ultrasound signal. By casting multiple layers of the same composition and allowing for a partial curing before casting the next layer, enough variation in acoustic impedance is introduced to create partial US reflections and the interface. A two-layer cementitious sample is shown in Figure 5.5B.

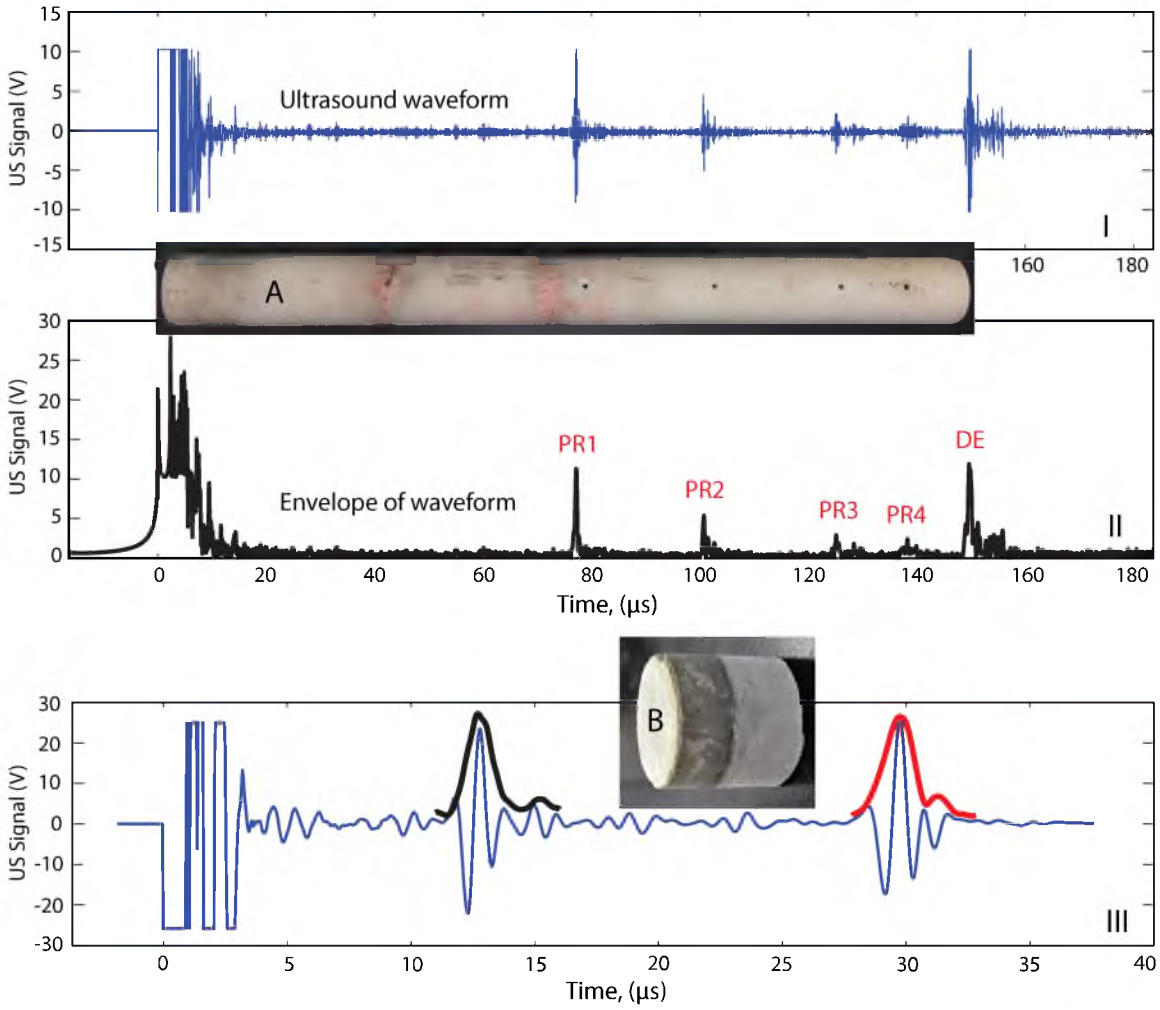

Figure 5.5: Top panel (I) shows echo waveforms produced by four echogenic features drilled along the length of the alumina waveguide and the reflection from its distal end. The corresponding envelopes are shown in the center panel (II). Bottom panel (III) shows echo waveforms and its envelopes produced from interface and distal end of cascaded cementitious sample.

Panametrics pulser/receiver (model 5072PR) and transducer (model V609) were used to create a broad-band excitation pulse with 5 MHz central frequency, and to receive echoes created by these partial reflectors and the reflection from the distal end of the waveguide. The echo waveforms were acquired using a Tektronix oscilloscope (model MSO 2024) interfaced to a computer. Custom Matlab code was written to control the acquisition, visualize the waveforms, and filter, analyze, and interpret the data. Figure 5.5 (top panel) shows typical waveforms collected from the alumina waveguide and its envelopes (center panel). Partial ultrasound reflections from the drilled holes are marked as PR1, ..., PR4 echoes; the reflection from the distal end of the waveguide is labeled as DE. The waveforms and their envelopes in the cementitious sample are also shown in Figure 5.5 (bottom panel).

The importance of accurately measured echoes' time of flight is highlighted by the influence the timing errors have on ultrasound measurements of temperature. Experimental characterization of $c = f(T)$ for our alumina waveguide indicated that at room temperature of 20°C, a TOF measurement error that overestimates the actual values by 0.1% implies that the temperature of the waveguide is 61°C—a temperature measurement error of 41°C! A measurement error corresponding to 1% overestimation in the TOF at the room temperature will result in the overestimation of the waveguide temperature by over 300°C.

When the ultrasound propagates through dissipative materials, noticeable variations in the waveforms taken under apparently identical experimental conditions are often present. Figure 5.6II illustrates the variability in the echo waveforms (blue traces) produced by an echogenic feature PR1 located in the middle of the waveguide. Both waveforms were acquired at identical experimental conditions but different times. The envelopes of the two waveform (black lines) are also affected by this variability. For instance, note the change in the position of the maximum envelope values indicated by green triangles. If the maximum values are used to time the arrival of echoes, the observed variability would result in TOF measurement errors and inconsistencies. Specifically, a shift in the maximum value between the two peaks in Figure 5.6II introduces the variation of 0.4% in the TOF measurements, which corresponds to a very significant (on the order of 150°C)

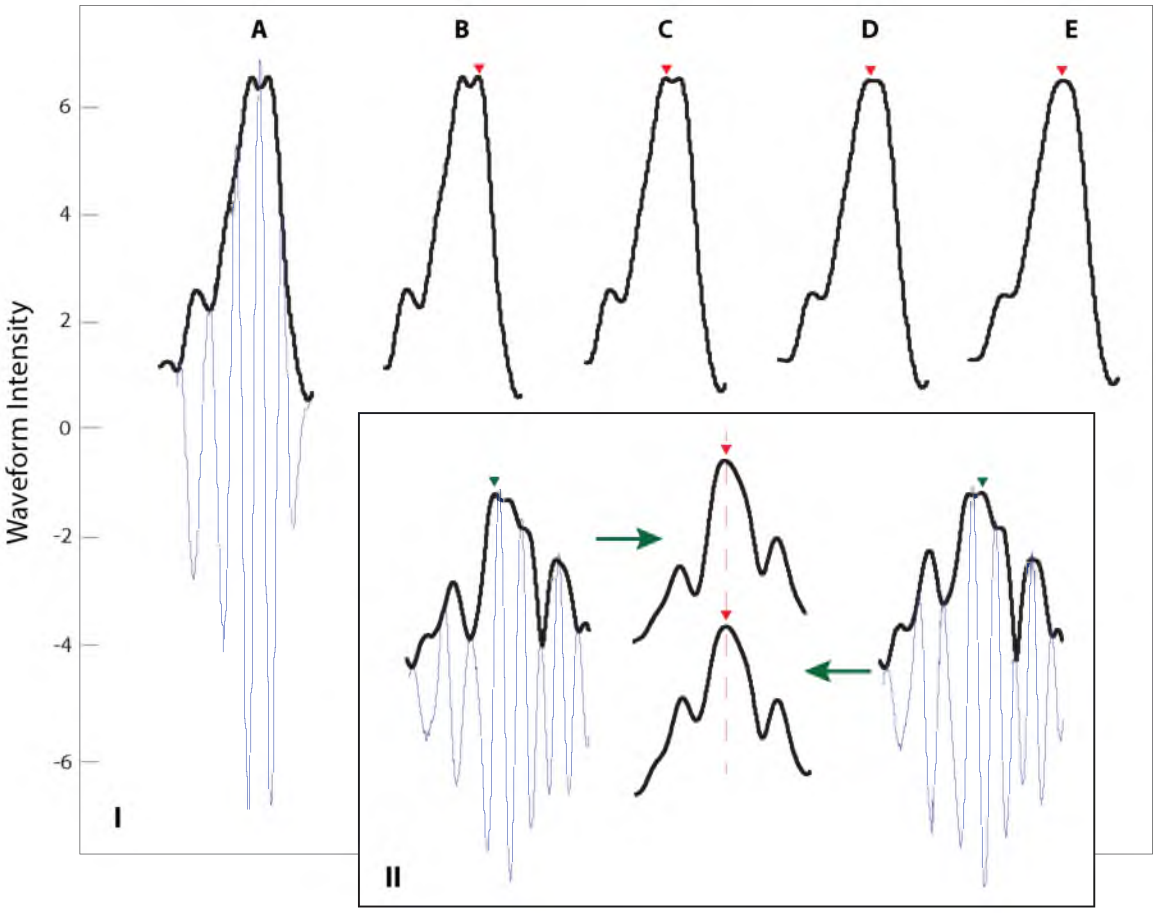

Figure 5.6: Examples of waveforms with the anisotropic diffusion filter treatment. (I) The original echo waveform, shown in blue, was produced by PR3 echogenic feature; its envelope is shown in A. The application of the filter for 100, 500, 1000, and 1500 iterations produced filtered envelopes respectively shown as B, C, D, and E. Maximum values of filtered envelopes are marked with red triangles. (II) Two echoes, shown as blue traces, were produced by PR1 feature, which were acquired at the same conditions but different times. Their envelopes show variability of the maximum value indicated by green triangles. After applying 3000 iterations, the filtered envelopes of both waveforms are shown in the middle of the panel. Red arrows show that the peak values coincide after filtering.

error in the estimated waveguide temperature.

Panel IA in Figure 5.6 shows the original echo waveform produced by the third echogenic feature of the waveguide (PR3) and its envelope. As in the case of echoes produced by PR1, the envelope of the original waveform is characterized by two closely separated peaks. Experiments showed that echo waveforms produced by PR3 and acquired at different times but identical conditions can also have the

maximum envelope value at either one of these peaks.

To address the observed inconsistencies and the corresponding timing errors, the proposed anisotropic filter was applied to the envelopes. Panels IB through IE show the filtered PR3 envelope as the number of iterations in applying anisotropic diffusion is increased from 100 to 1500. With more iterations, small variations are blurred, the filtered envelope retains a single peak, and its position is stabilized. The position of this peak can now be used to consistently time the arrival of ultrasound echoes. Once the filtered envelope is obtained, other single-point and shape-matching timing techniques may also be used.

Panel II shows that small variations in the envelopes of PR1 echoes acquired at identical conditions are filtered out after 3000 iterations and the single peak value is stabilized at the same location within both envelopes. If the maximum value of the filtered envelope is used to time the echoes, the identical estimation of the time of flight will be produced despite the variations in the original waveforms and their unfiltered envelopes.

The influence of different timing methods on the variability of the estimated TOF was investigated next. Several timing methods were considered: (a) Timing based on the maximum of the acquired echo waveform; (b) Timing by threshold value, which we selected to be 1/3 of the maximum of the waveform value; (c) Cross-correlation between the two waveforms; (d) Cross-correlation between their envelopes; (e) Maximum value of the filtered envelope; and (f) Cross-correlation between envelopes filtered using the anisotropic diffusion. The comparison was performed for the two PR1 echo waveforms shown in Figure 5.6II. For the selected methods, the difference in timing results when one or another waveform was used is given in Table 5.2, which also lists the corresponding errors in the estimates of the waveguide temperature. After applying 3000 iterations of the developed anisotropic diffusion filter, the peaks of filtered envelopes were located in the identical positions for both waveforms, as illustrated in Figure 5.6II. The cross-correlation between the two filtered envelopes shows that a zero shift is needed for the best match, indicating timing consistency when either one of the waveforms is used. For all other methods, the difference in timing based on the two waveforms

Table 5.2: Timing errors and corresponding temperature differences

Alumina		
Method	**Timing difference**, s	**Difference in** T, °C
Peak of the waveform	3.0×10^{-8}	50.47
Threshold of the waveform	2.5×10^{-8}	42.30
Waveform cross-correlation	2.6×10^{-8}	43.94
Envelope cross-correlation	2.6×10^{-8}	43.94
Peak of filtered envelope	0	0
Cross-correlation of filtered envelopes	0	0
Cementitious		
Method	**Timing difference**, s	**Difference in** T, °C
Peak of the waveform	9.0×10^{-8}	7.4
Threshold of the waveform	10.0×10^{-8}	8.2
Waveform cross-correlation	7.2×10^{-8}	5.9
Envelope cross-correlation	5.6×10^{-8}	4.6
Peak of filtered envelope	0	0
Cross-correlation of filtered envelopes	0	0

was on the order of 25 nanoseconds. If we assume that this difference is an increase in the TOF over the actual value acquired when the waveguide is maintained at 20 °C, the timing errors would correspond to the overestimation of the waveguide temperature by over 40 °C.

These timing methods were also applied for TOF estimation on the cementitious sample. The results were summarized in Table 5.2, too. The results clearly show that the cementitious sample has stronger dissipation and attenuation on the ultrasound collected waveform compared to the alumina waveguide. Both cross-correlation methods gave better results than peak and threshold methods, while filtered envelope methods are the most stable and consistent on TOF estimation. However, the speed of sound dependence of temperature is linear and much smaller for the cementitious sample than that of the alumina sample. For reference temperature at 20 °C, the 1% change of TOF causes a temperature difference of 25.9°C. Therefore, in this experimental test, the great inconsistency of TOF leads to much smaller temperature fluctuation for the cementitious sample, only less than 10 °C.

Figure 5.7 shows a comparison of real-time monitoring of this 12-inch alumina

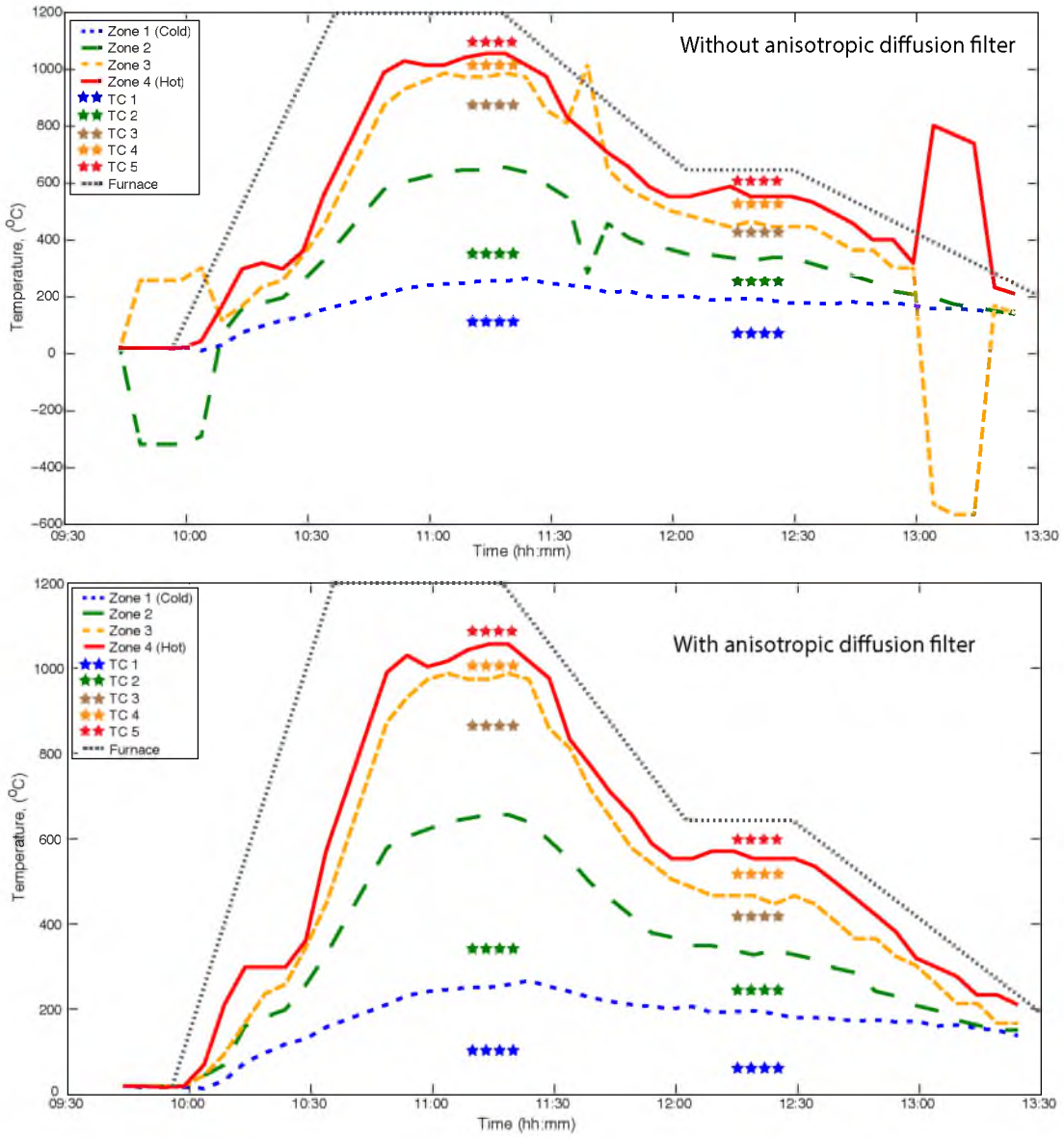

Figure 5.7: Real-time temperature monitoring results comparisons of TOF estimation treated without and with anisotropic diffusion filter.

rod temperature profile with part of the rod inserted into the horizontal electronic furnace without and with anistropic diffusion filter treatment. There are peak fluctuations found in temperature calculated only using the waveform envelope which caused significant temperature fluctuations in the top figure. The bottom result with anisotrpic filter computation for temperature showed a stable and consistent temperature profile of this alumina rod for a long time. Furnace temper-

ature setup order is shown as a grey dash line in Figure 5.7. The thermocouples' temperature at steady state are also included. Temperatures measured using the ultrasound method match with thermocouple results very well. Especially, the US method responded to furnace temperature vibration more sensitively than the thermocouples.

CHAPTER 6

PILOT-SCALE OXYFUEL COMBUSTOR EXPERIMENTS

6.1 Pilot-Scale Oxyfuel Combustor

The 100 kW pilot-scale ultrasound temperature measurement experiments were carried out on a downfired oxyfuel combustor (OFC) schematically shown in Figure 6.1. This unit was designed to allow for a systematic control of inlet gas flow rates and wall temperatures high enough to simulate the self-sustaining combustion conditions of full-scale units in terms of the temperatures, coal particle concentrations, and mixing.

The OFC has three zones, from top to bottom: ignition (0.61 ID $\times$ 0.91 OD $\times$ 1.22 m height), radiation (0.27 $\times$ 0.61 $\times$ 2.60 m), and convection (0.15 $\times$ 0.15 $\times$ 3.66 m) zone. The combustion products exit the convection zone and pass through eight heat exchangers which cool the flue gas prior to discharge. The ignition zone is normally surrounded by 3 $\times$ 8 $\times$ 840 W flanged ceramic-plate electrical heaters used to control the wall temperatures of the furnace. However, these heaters fell off from the interior surface of the refractory wall during a previous test and our experiments proceeded without using them.

Nine pairs of ports (marked as P1–P9 in Figure 6.1) are positioned along the vertical section of the unit. They can be used for sampling, instrumentation insertion, and observations. Our refractory ultrasound waveguide was mounted in the ignition zone inside port P3. The burner for this unit is not equipped with an ignition nozzle. As a result, natural gas must first be used to heat up the furnace to a temperature high enough to ignite coal particles introduced into the ignition zone and to maintain sustained combustion. Natural gas was also used to keep furnace temperature high at night.

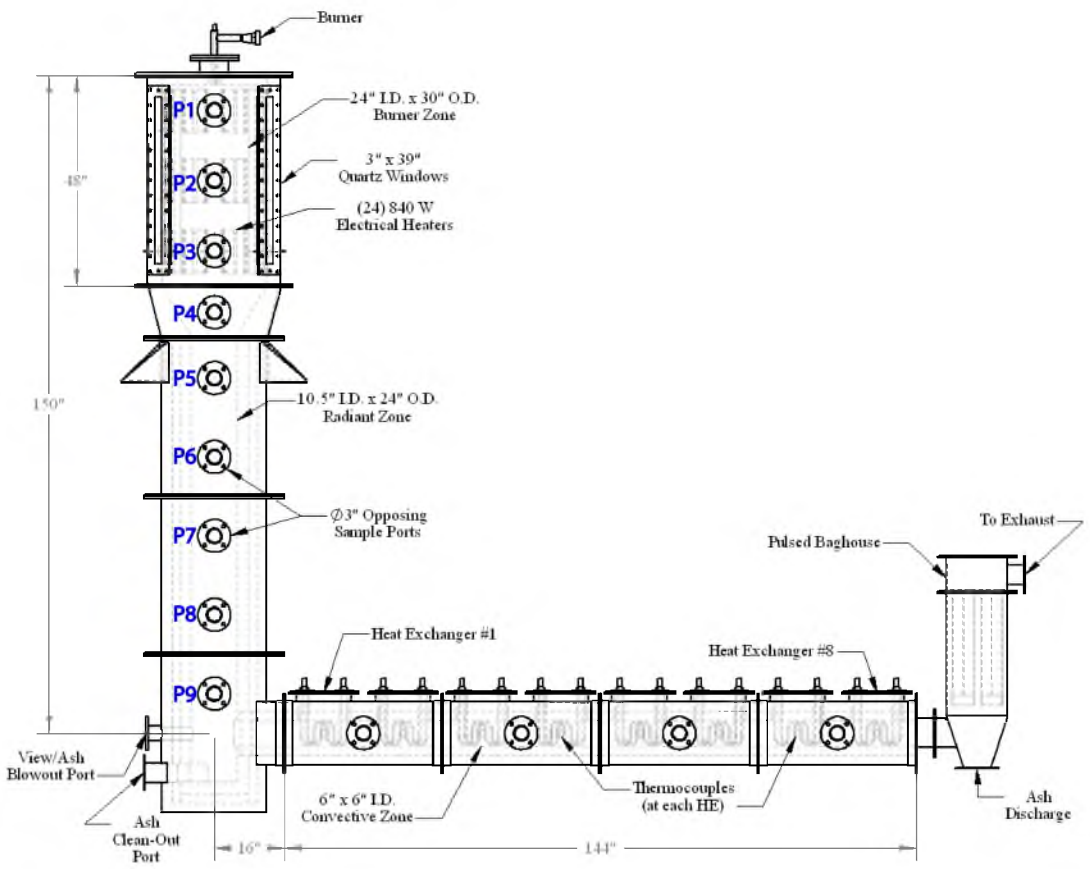

Figure 6.1: The 100 kW pilot-scale downfired oxyfuel combustor.

6.2 US-MSTD System Design and Implementation

The overall US-MSTD system that was designed to provide continuous real-time temperature measurements consists of an ultrasound waveguide structured to provide multiple partial reflection from known locations along its propagation length, an ultrasound transducer/receiver, and data acquisition, logging, interpretation, and real-time display system. The schematic view of the waveguide measurement system assembled to the furnace is shown in Figure 6.2.

The fixture for the waveguide insertion part is shown in Figure 6.3. It was designed to address several issues targeted for the field test, including confinement integrity, ultrasound coupling, and active cooling of the rod to insure that the temperature of its cold end is within the allowance temperature of the transducer.

The same alumina refractory rod with five segments was continuously used as the ultrasound waveguide for in-situ pilot-scale oxyfuel combustion tests, while

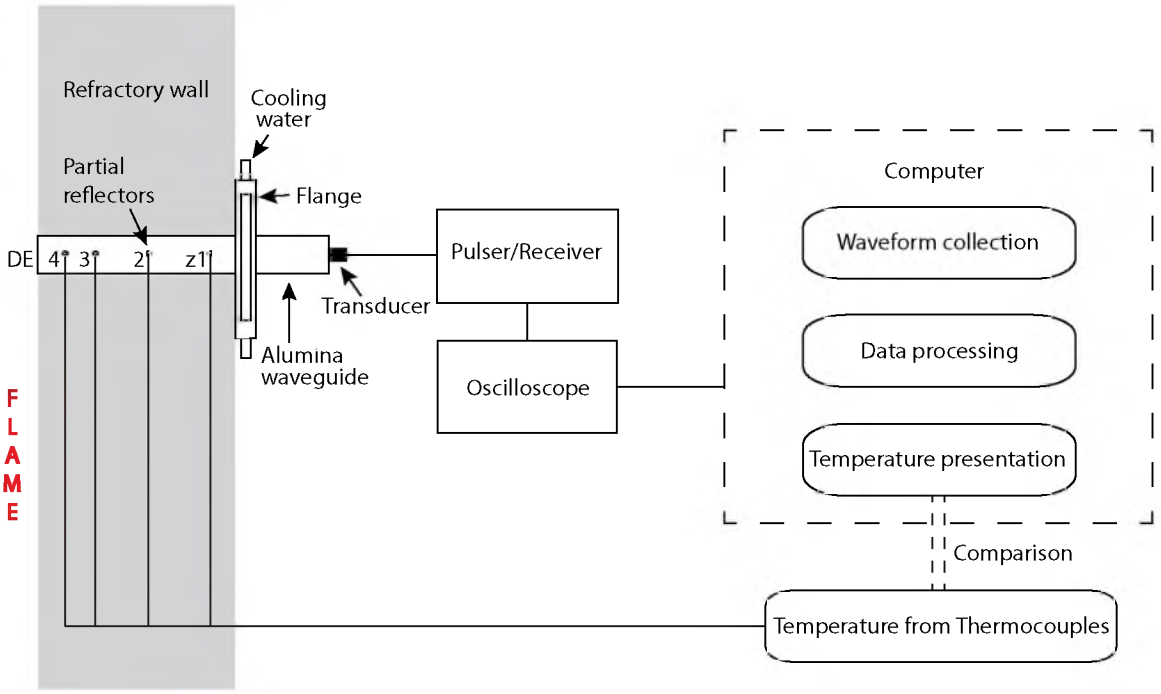

Figure 6.2: The schematic overview of US-MSTD installation on pilot-scale OFC. A 1×12-inch alumina waveguide was engineered at predetermined spatial locations along its length located 6, 4, 2, and 1 inches—marked as z_1, z_2, z_3, and z_4, from the hot distal end (DE) of the rod. The data acquisition and interpretation systems provide real-time temperature distribution across the refractory and compare with thermocouple measurements.

the segment from transducer-waveguide interface to z_1 is served as delay line, and the temperature in this segment is not estimated. The thickness of the refractory and the vessel shell combined is $6^1/_2$ inches. The length of the inserted alumina waveguide was selected to place the distal end of the waveguide flush with the OFC refractory. Port 3 has an opening of 3 inches. The inserted waveguide was wrapped with fiberglass insulation to fill the gap between ultrasound waveguide and OFC refractory. Omega Super OMEGACLAD® type K thermocouples were bent at 90° and inserted into the holes drilled into the waveguide to provide ultrasound echoes to provide independent temperature measurements. Since there was no thermocouple attached on the hot distal end of the waveguide, one more Omega Super OMEGACLAD ® type B thermocouple was inserted in port 2 where the thermocouple's tip is at the edge of the refractory hot face. Cooling water was run through the fixture to ensure that the temperature of the rod's

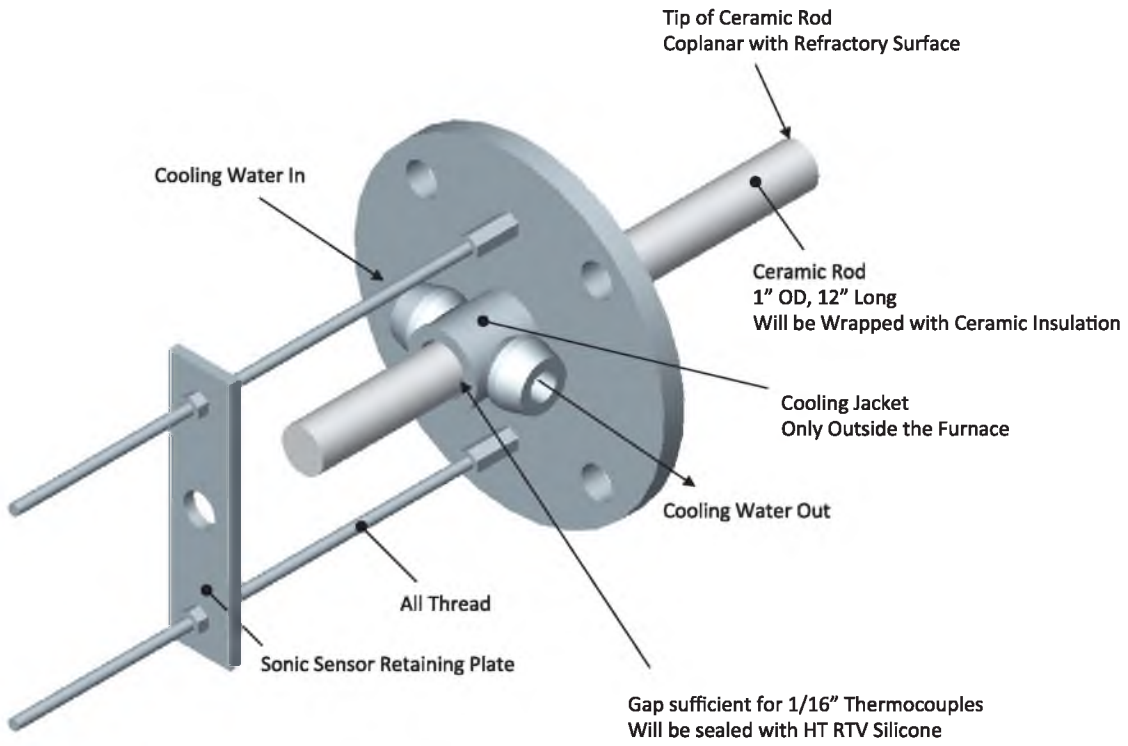

Figure 6.3: Port-mounted waveguide retention system.

cold side was within operating limits of the ultrasound transducer. A reflective shield was placed between the combustor and transducer, to minimize the effect of radiative heat transport on the ultrasound transducer. The transducer was mounted using a retaining plate with a threaded ring, which provided a secure and flexible way for its installation and coupled to the waveguide using silicone grease. In this described approach, the sensitive electronic components are kept away from harsh gasification environments and it is only required that the US transducer be acoustically coupled to the cold side of the refractory, representing minimal modifications to the combustor.

The data acquisition system was kept the same as from the high-temperature lab-scale test. A custom Matlab software was developed for online data acquisition, storage, interpretation, and temperature profile across the refectory visualization from ultrasound TOF measurements that used the combination of envelope cross-correlation method and anisotropic diffusion filter discussed in the previous chapter. Based on the time of flight results of each segment calculated

from collected ultrasound waveform, the real-time temperature information can be obtained through the calibrated relationship between temperature values and the speed of sound found experimentally from the high-temperature lab test. In order to process the ultrasound measurements at a high sampling rate (every 5 seconds), a simplifying assumption was made. A piecewise constant distribution of temperatures in the four segments of the waveguide was applied during the real-time data manipulation. The algorithm for online temperature profile determined based on piecewise constant assumption is illustrated in Algorithm 6.1 The collected and saved waveforms during the experiments have been reinterpreted using a more accurate piecewise linear assumption after this campaign.

Algorithm 6.1 Ultrasound Waveform acquisition and temperature interpretation

$sig, t \Leftarrow invoke(readwaveform, channel)$
$sig \Leftarrow abs(hilbert(sig))$
$sig \Leftarrow anisodiff(sig, 100, 1/3, 20, 1)$
for $l = 1$ **to** n **do**
  $ls, lt \Leftarrow selectinterval(sig, t)$
  $m, loc \Leftarrow findpeaks(ls, NPEAKS, 1)$
  $peaks(l) \Leftarrow lt(loc)$
  if $l > 1$ **then**
    $TOF(l-1) \Leftarrow peaks(l) - peaks(l-1)$
  end if
end for
$\Sigma \Leftarrow c_{max} - c_{min}$
$\Phi \Leftarrow T_{max} - T_{min}$
$\alpha \Leftarrow \Sigma * a / c_{min}$
$\beta \Leftarrow \Sigma * R^{-T_{min}/\Phi - b} / c_{min}$
$Temp \Leftarrow log((1 + \alpha - 2 * L/(c_{min} * TOF))/\beta)\Phi / log(R)$

6.3 Experimental Conditions

During this pilot-scale oxyfuel combustion campaign, the following conditions were used for fuel fed rate. The flow rate of natural gas was between 6–6.5 lb/hr; Utah coal was fed at 8.4 lb/hr; primary O_2 maintained the flow at 2.3 lb/hr; primary flow of CO_2 was 11.9 lb/hr; secondary O_2 was fed at 16.5 lb/hr. The internal pressure was elevated by ~0.1" of water.

The OFC operation processes that the US-MSTD system used to monitor temperature distribution across the refectory include:

(a) steady state combustion of natural gas and coal;

(b) the fuel transition from natural gas to coal; and

(c) combustion at the different fuel flow rates.

6.4 Experiments and Results

6.4.1 Natural Gas Preheating

Figure 6.4 shows the measured temperature change along the waveguide based on piecewise constant assumption during initial preheating of the OFC by natural gas. About half an hour after the heat start, there was an unaccountable temperature drop at zone 4, which is the closest to the flame. Zone 4 reheated up after 15 minutes of temperature reduction, and was below the temperature of its adjacent zone 3 until 40 minutes later. The electrical heaters, normally used at the startup of the unit, were not available. We may be seeing a temperature change due to a combination of changing flow rates of natural gas and air, controlled manually and without the benefit of the electrically controlled refractory temperature. The acquisition of the thermocouple measurements did not start until 1 hour after fire start. The test for temperature distribution of the natural gas preheating process using the ultrasound approach lasts $2^1/_2$ hours. The drying of the ultrasound couplant caused the deterioration of the strength of the echo emanating from the hole closest to the reaction zone. The acquisition of the ultrasound signal was stopped and was not restarted until the next experiment.

6.4.2 Steady State Natural Gas Combustion

Temperature measurements based on piecewise constant assumption acquired after the unit was heated with natural gas for a long enough time to achieve stable conditions are shown in Figure 6.5. Figure 6.6 presents a more realistic and dynamic temperature profile that is determined using piecewise linear assumption along the ultrasound propagation waveguide. The temperature changes based on piecewise constant and piecewise linear assumptions of ultrasound measurements, and thermocouple measurements at reflector locations z_2, z_3, z_4, and the hot distal

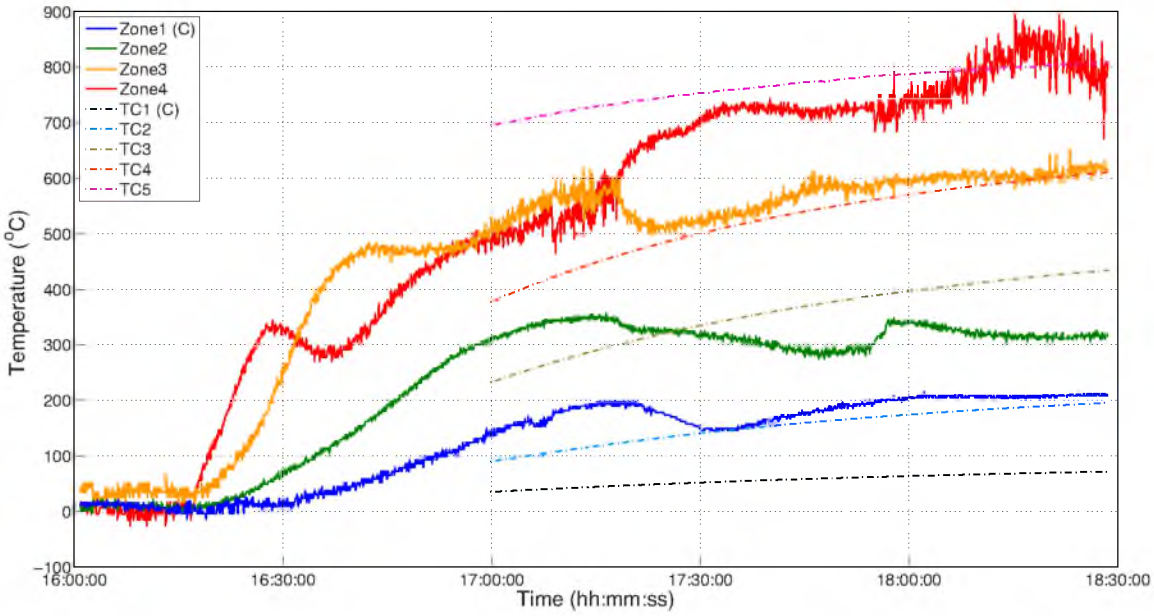

Figure 6.4: Ultrasound measurements with piecewise constant assumption and thermocouple measurements for temperature distribution across the refractory as the OFC is being preheated by the natural gas combustion without the electric heaters. Thermocouple measurements were not recorded until 1 hour after the campaign started.

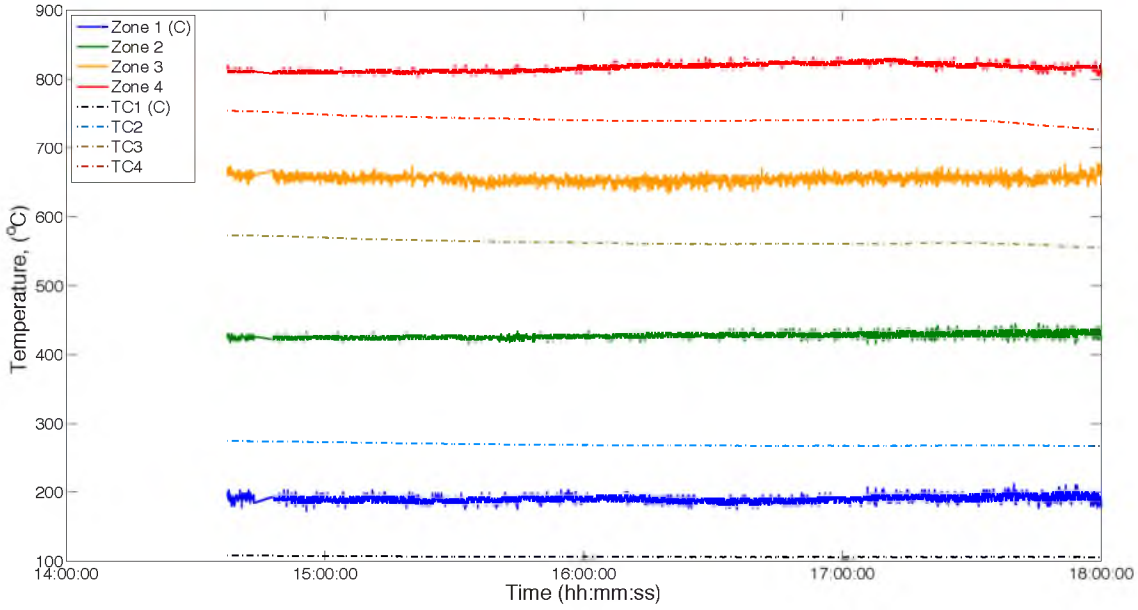

Figure 6.5: Ultrasound measurements with piecewise constant parameterization and thermocouple measurements show a same temperature trend during stable natural gas combustion.

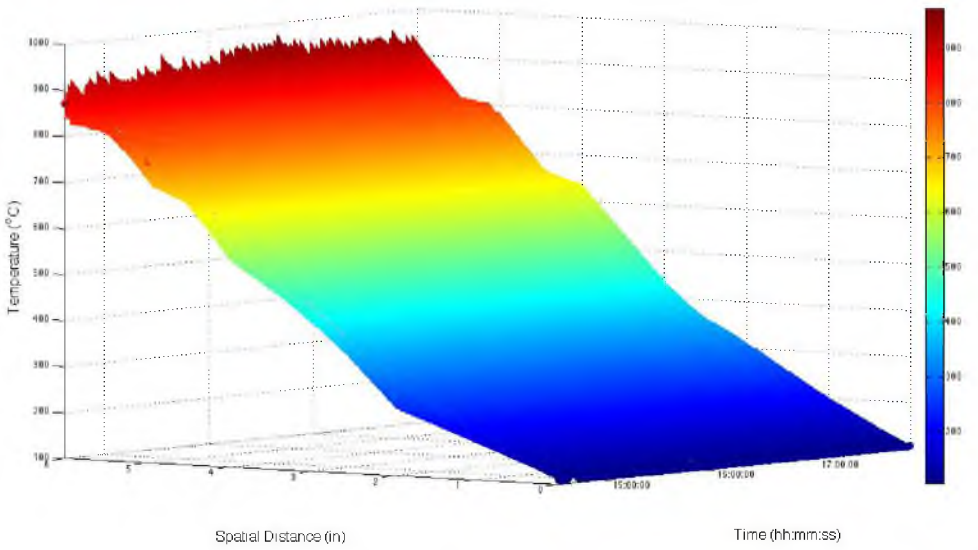

Figure 6.6: Temperature distribution across the refractory based on piecewise linear assumption during stable natural gas combustion.

end are shown in Figure 6.7. In Figure 6.7, the piecewise constant estimation presents the temperature of zone 4, while the piecewise linear method shows the point-wise temperature at this location. Thus, there is a temperature difference presented between thess two ultrasound temperature estimations. The temperatures from piecewise constant assumption at reflectors' locations are calculated by averaging the adjacent segmental temperatures. For over 3 hours of continuous experiments, both ultrasound measurement and thermocouples show the same trend on temperature, while ultrasound measurements appear to be more sensitive to temperature changes than thermocouples. The results from piecewise linear calculation give more temperature vibration than those from piecewise constant, due to the sensitivity of temperature response of the TOF vibration and the temperature continuity assumption along the propagation path.

6.4.3 Transition from Natural Gas to Coal

The next combustion process that US-MSTD captured is the fuel transition from natural gas to coal. Figures 6.8 and 6.9 show the overall temperature changes using piecewise constant and piecewise linear assumption, respectively, compared with thermocouple measurements. The transition happened after the natural gas

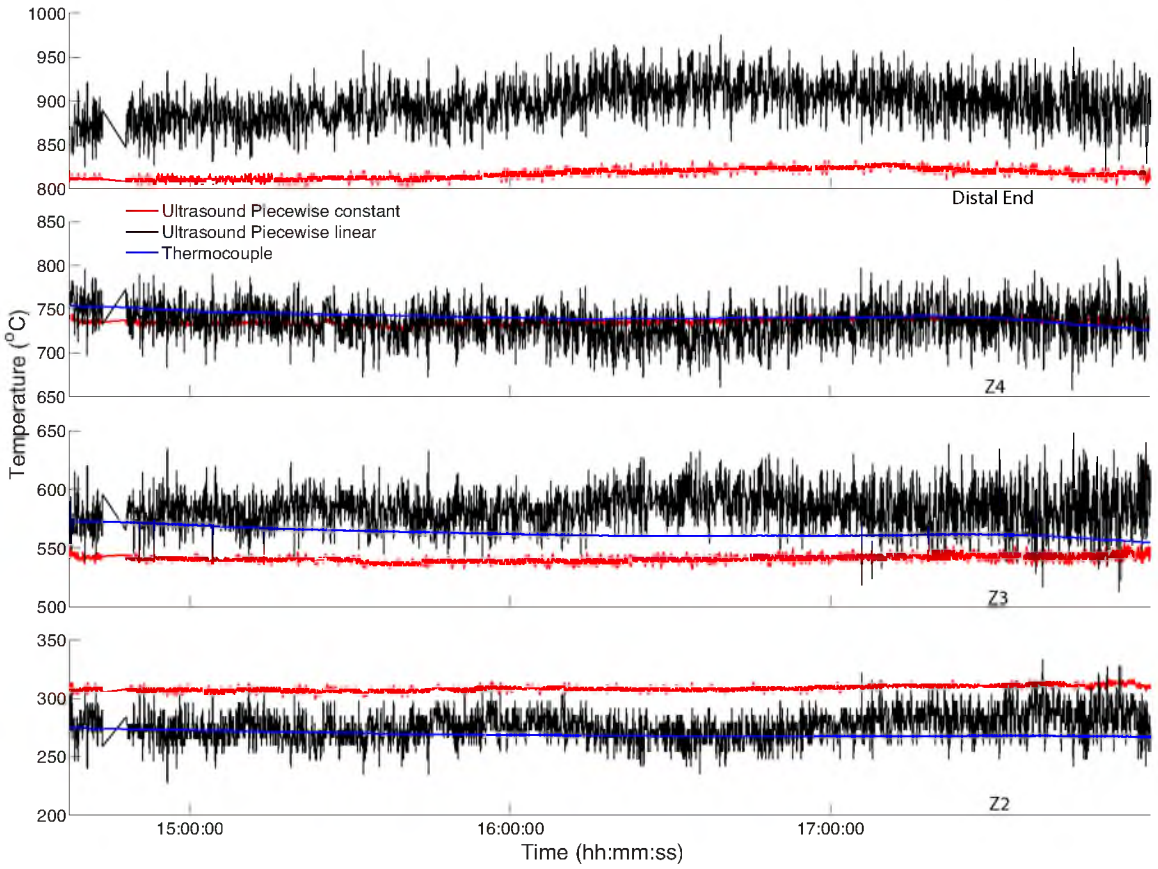

Figure 6.7: Temperature distributions obtained from ultrasound measurements using two different parameterizations and thermocouple measurements during stable natural gas combustion are compared at all echogenic features' locations and the hot distal end. A great agreement of temperature change is shown for all the methods. In addition, both ultrasound measurements appear to be more sensitive to temperature changes than thermocouples.

combustion reached steady state for over 8 hours. A half hour after the start of this temperature profile measurement, the flow of natural gas was stopped, leading to the decrease of the temperature, first seen in zone 4, then zone 3 with descending temperature drop. The US-MSTD system immediately responded to the thermal energy changes, even before the thermocouple did. The feeding of coal started about 10 minutes later. Again, the ultrasound measurements promptly indicated that the change in fuel had occurred by showing the trend of rising temperatures. The temperature distribution change along the waveguide indicates the heat conduction process from the refractory hot face to the vessel shell. The comparisons of temperature results of both ultrasound interpretations

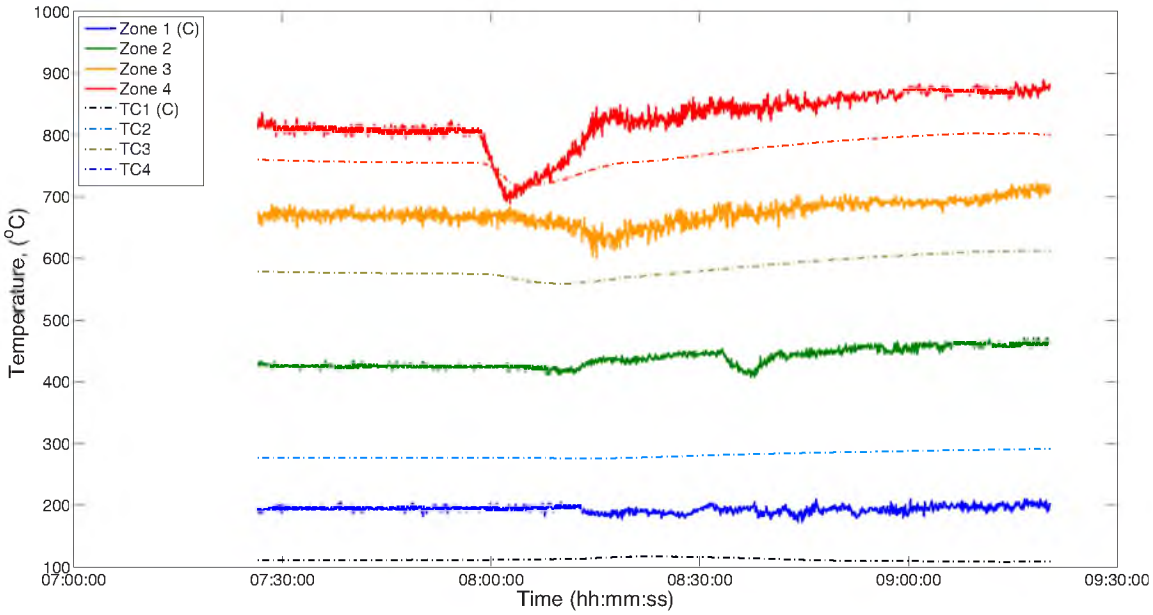

Figure 6.8: Segmental temperature profiles obtained from both ultrasound with piecewise constant assumption and thermocouple measurements during transition from natural gas to coal combustion. The plots show good agreement with two methods, and ultrasound responses for temperature change are faster than thermocouples.

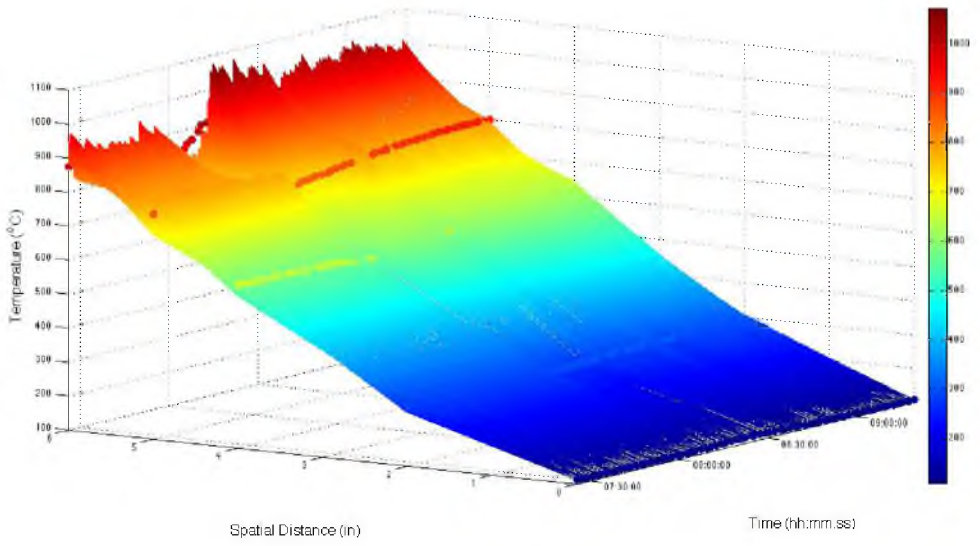

Figure 6.9: The real-time temperature profiles across the refractory obtained from ultrasound based on piecewise linear assumption and thermocouple measurements during transition from natural gas to coal combustion captured the temperature responses for fuel transition.

and thermocouple measurements at the hot distal end and all echogenic features are shown in Figure 6.10. Compared to thermocouples, the US measurements give both faster and more pronounced indication that the operating conditions have changed.

6.4.4 Response to Decreased Flow Rate of Coal

Temperature distributions obtained from the coal combustion process, which started right after the transition in fuel from natural gas to coal, tested on another day, are shown in Figures 6.11 and 6.12, based on piecewise constant and piecewise linear assumption, respectively. Temperature has an initial increase after the fuel transition shown in zone 4 and 3, while zone 1 and 2 have not recovered from the temperature drop due to a stop of the natural gas feed. After temperature rising and

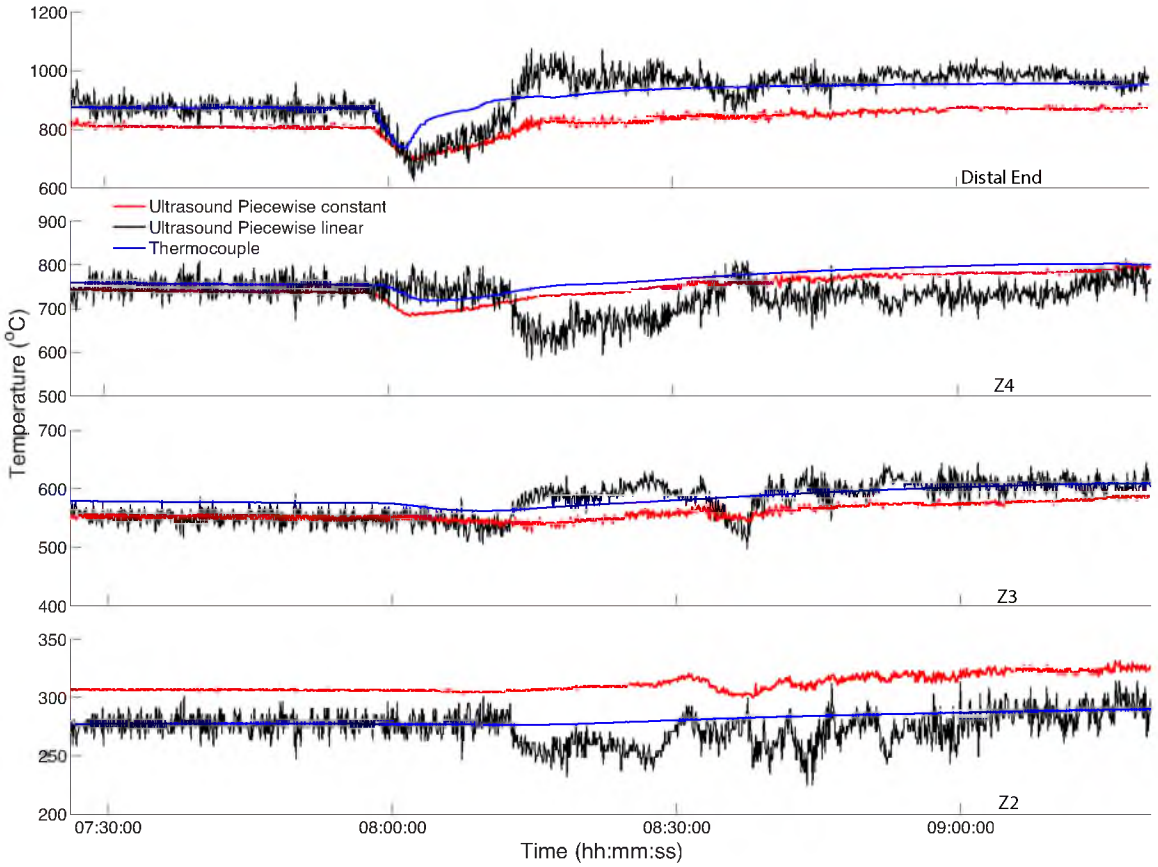

Figure 6.10: Temperature profiles obtained from the US-MSTD approaches and thermocouples during transition from natural gas to coal combustion show comparable temperature results at echogenic features' locations and the hot distal end.

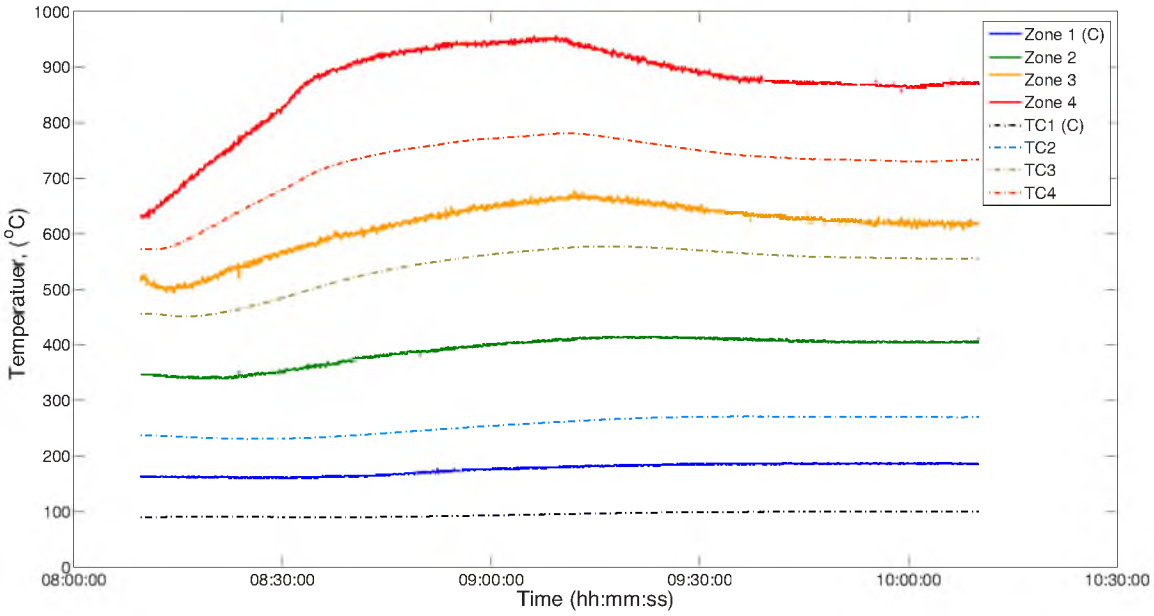

Figure 6.11: Segmental temperature responses from ultrasound measurements based on piecewise constant assumption and thermocouple measurements are captured during the process of a change feed rate of coal combustion, followed by the fuel transferred from natural gas to coal. Both temperature measurements present the same trend on temperature changes.

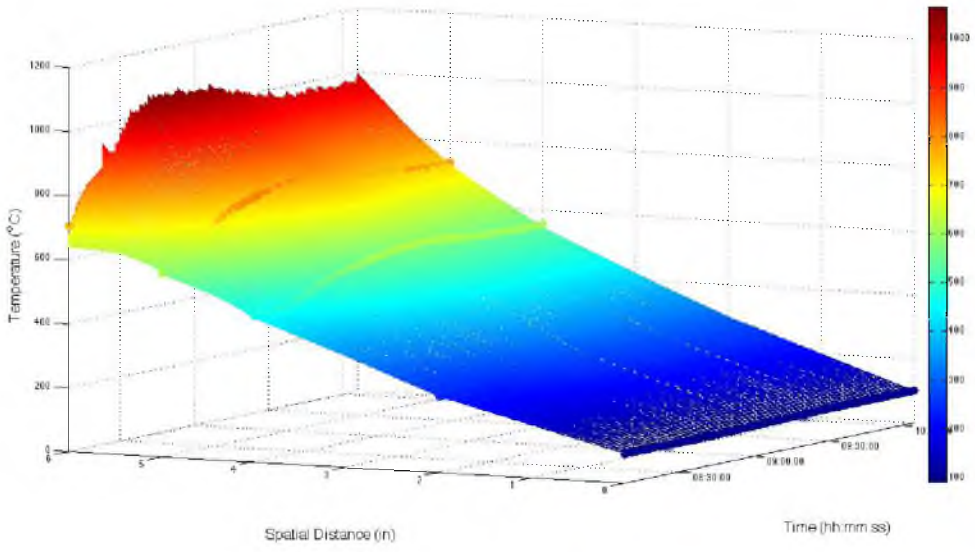

Figure 6.12: Temperature response from ultrasound based on piecewise constant assumption and thermocouple measurements for a change feed rate of coal combustion.

then stabilizing, about 1 hour after this experiment started, the temperature started to decline in response to the reduced flow rate of coal, beginning from the hot distal end. The reduction of coal flow rate has a limited effect on the temperature change of zone 2 and 1. The temperature profiles of comparison among ultrasound piecewise constant, piecewise linear calculation, and thermocouples at the hot distal end and all echogenic features' locations present an excellent agreement, shown in Figure 6.13.

6.4.5 Stable Coal Combustion

The last captured process for this campaign shown in Figures 6.14 and 6.15 is the temperature profile of a continuous stable coal combustion, estimated by ultrasound measurements using piecewise constant and piecewise linear assumption,

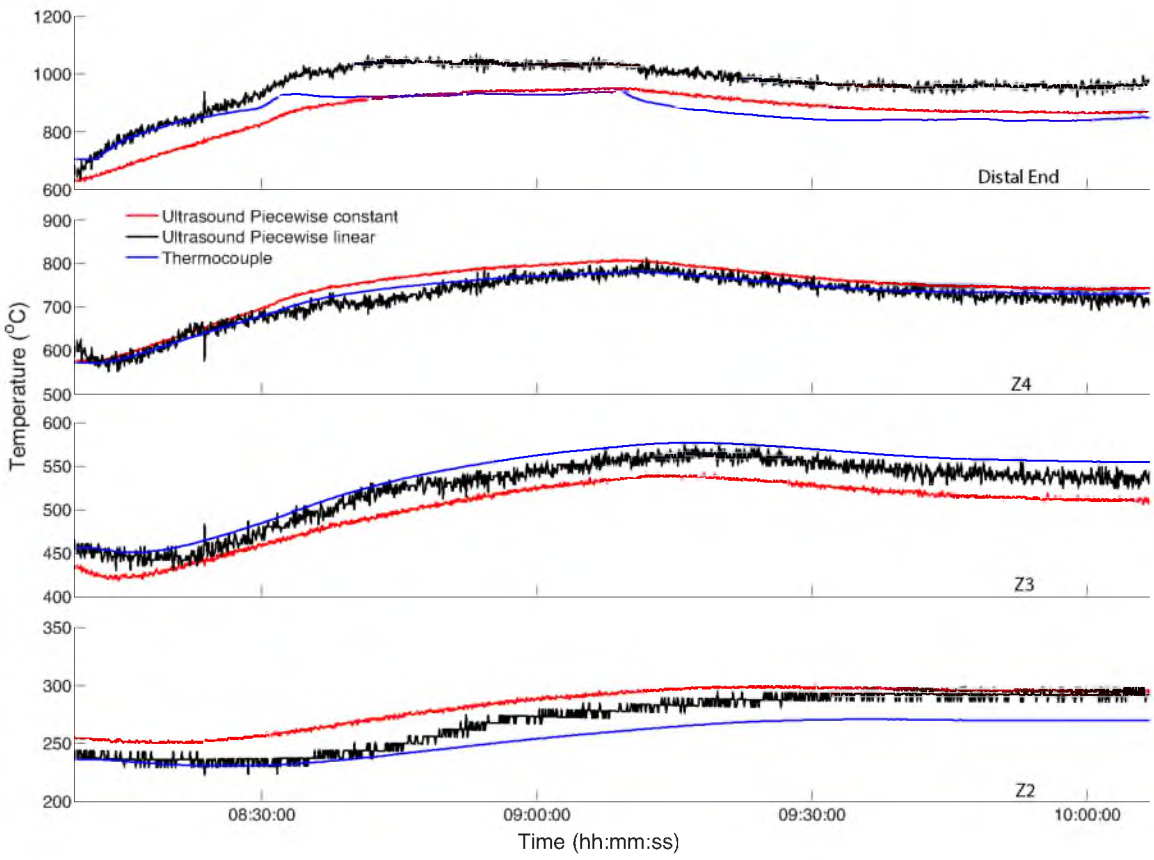

Figure 6.13: Temperature responses from ultrasound and thermocouple measurements for a change feed rate of coal combustion at echogenic features' locations and the hot distal end show an excellent agreement of these two approaches, while ultrasound responses are more sensitive than thermocouples.

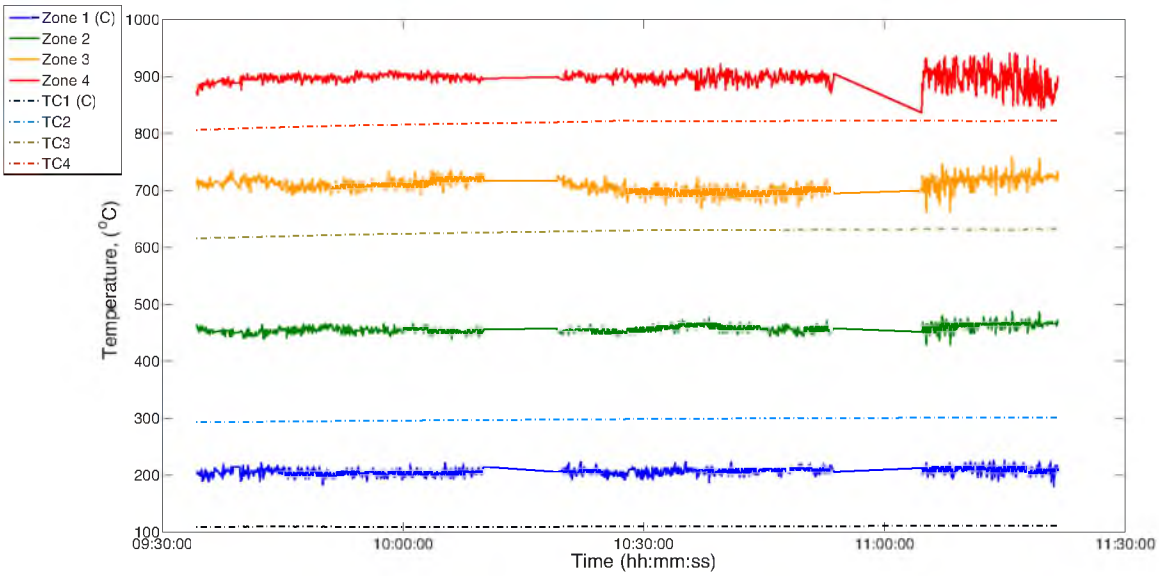

Figure 6.14: Ultrasound measurements using piecewise constant assumption and thermocouple measurements for temperature distributions during stable coal combustion. Intervals of ultrasound measurements flat lined correspond to the application of fresh ultrasound couplant at the transducer-waveguide interface. The vibration of ultrasound measurement is stronger than previous acquired processes due to significant reduction of ultrasonic waveform strength.

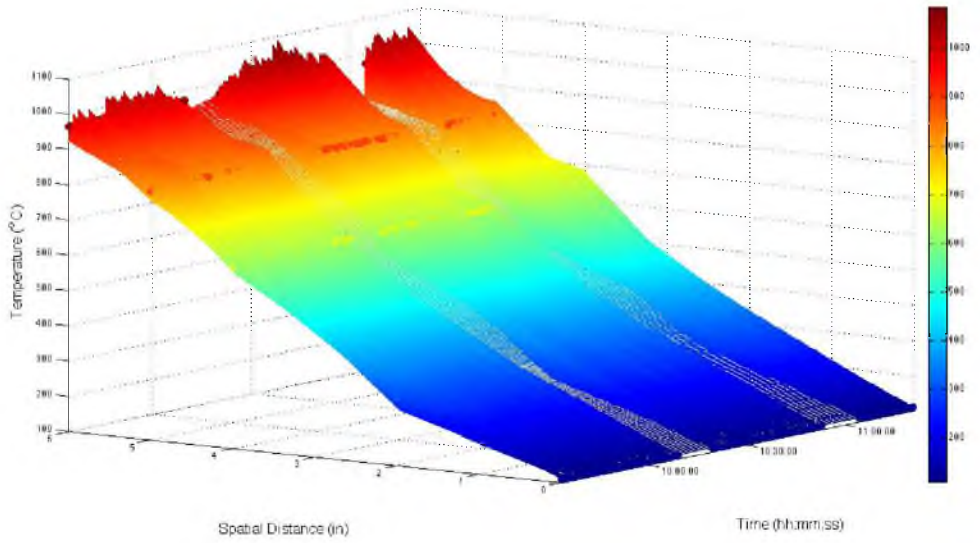

Figure 6.15: Ultrasound measurements using piecewise linear assumption and thermocouple measurements for temperature distributions during stable coal combustion.

respectively. The comparisons of temperatures of both ultrasound interpretations and thermocouple measurements at the hot distal end and all echogenic features are shown in Figure 6.16. The overall temperatures of coal combustion are higher than the natural gas combustion, especially in zone 3 and 4. The vibration of ultrasound measurement is stronger than other acquired processes. Significant reduction of ultrasonic waveform strength was observed during the test, especially at interfaces 1 inch from the distal end. Several intervals when ultrasound measurements flat lined correspond to times when the signal had deteriorated enough to motivate the application of fresh ultrasound couplant at the transducer-waveguide interface. After-test investigation on this alumina waveguide discovers that a more likely reason for deterioration of the ultrasound signal is the change in the material

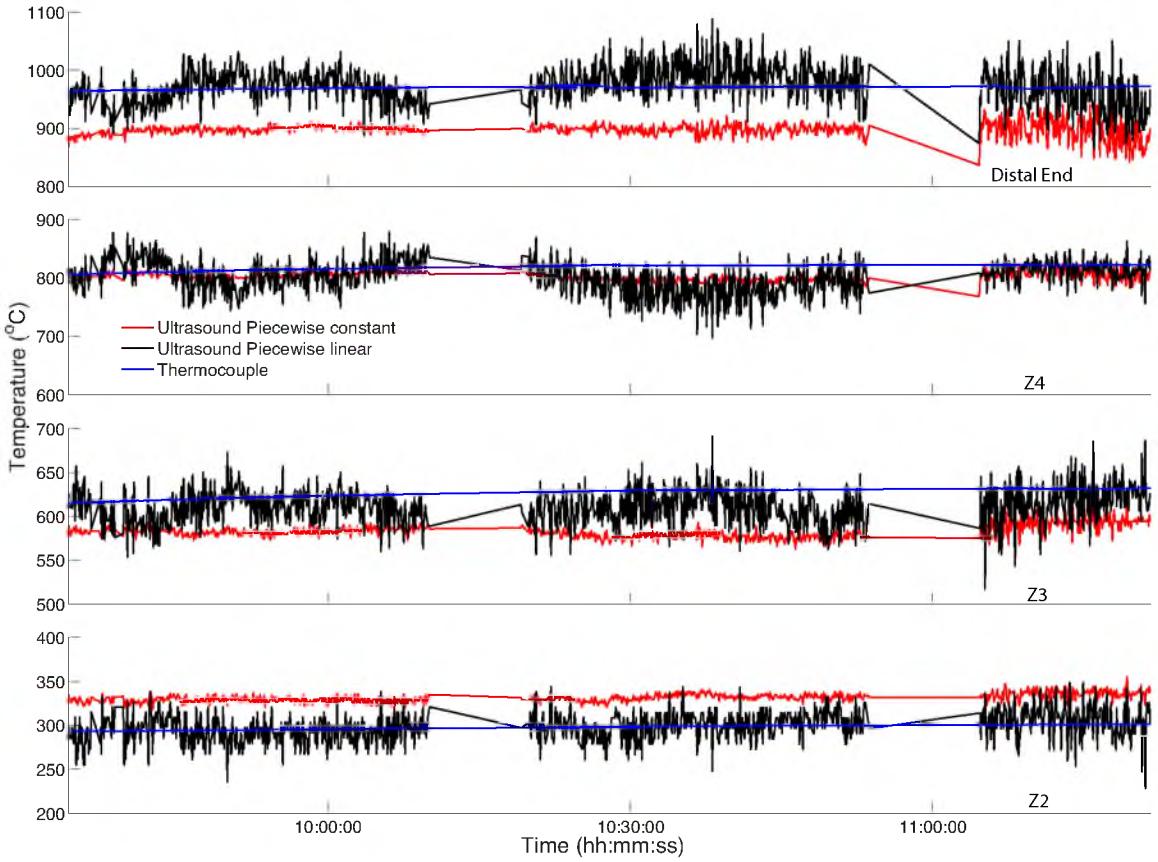

Figure 6.16: Temperature profile comparisons between ultrasound and thermocouple measurements at echogenic features' locations. The overall temperature distributions from both measurements are comparable, while stronger vibration in ultrasound measurement is observed than in other acquired processes.

properties, mainly the grain structure.

6.4.6 Temperatures at Distal End

Since there was no thermocouple attached at the hot distal end of the alumina waveguide, the temperature profiles at this location were obtained only from ultrasound measurements. The verification of the US-MSTD system results at the location is performed using the temperatures that were recorded from a type B thermocouple at port 2, where the TC's tip was aligned with the distal end of the waveguide. The results of the last four processes, including the stable combustion of both fuels, the fuel transition, and the flow rate change, are summarized in Figure 6.17. The temperature results of the ultrasound method are consistent with the independent thermocouple measurements—presenting the same trend on the temperature changes. More important, the values obtained from the US-MSTD system are in the same temperature range as TC's. This demonstration shows

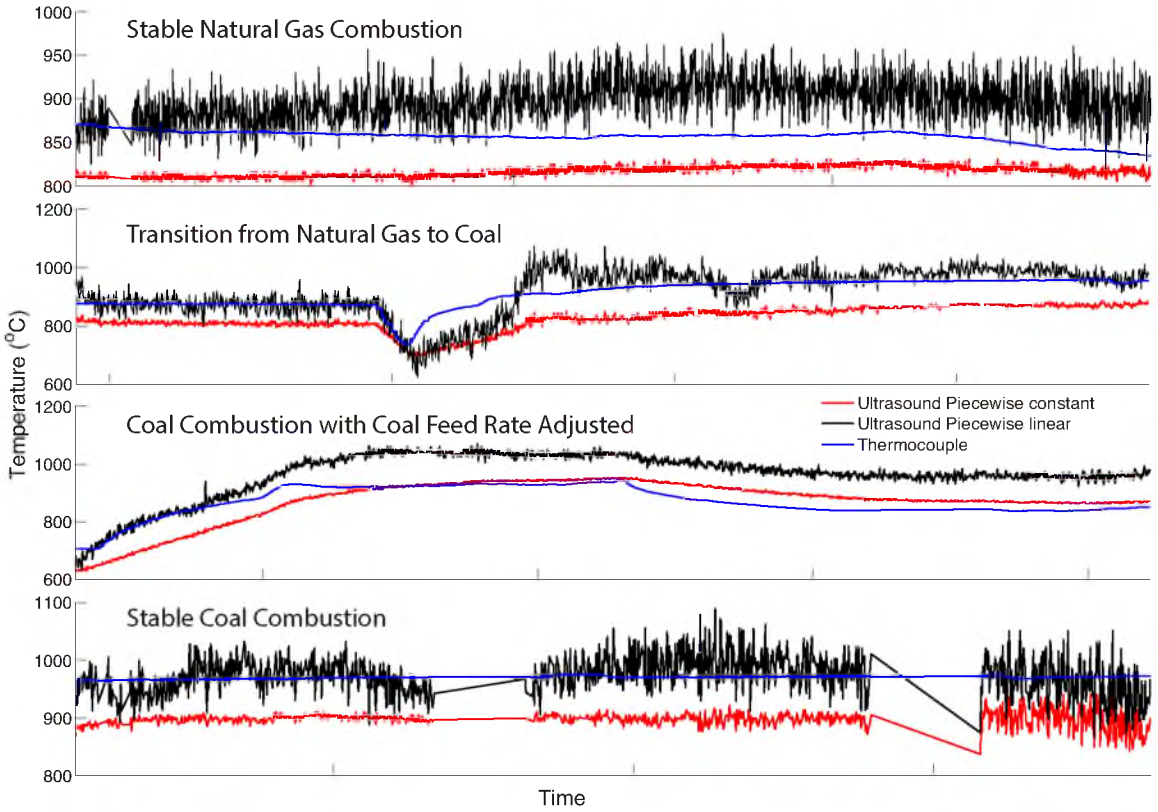

Figure 6.17: The temperature profiles obtained from the US-MSTD system at the hot distal end are verified with the thermocouple measurements at port 2.

that the US-MSTD system is able to monitor the real-time temperature profile for industrial-scale facilities.

6.5 Discussion

The US-MSTD system was successfully tested during the pilot-scale OFC oxy-fuel campaign. Real-time temperature distributions along the waveguide were captured during all relevant process changes. The comparison of temperature results based on the US-MSTD method and thermocouple measurements exhibit excellent consistency. Several issues were revealed during the test.

6.5.1 Couplant

The continuous real-time temperature monitoring using the US-MSTD method requires permanent coupling which is essential for providing the acoustic bond between the transducer and the waveguide. Couplants come in different forms, gel, oil, grease, pastes, and many more. We chose silicon grease because of its close acoustic impedance to alumina, high viscosity, relatively slow drying/evaporation rate compared to gel, and low environmental sensitivity. However, we still need to change our couplant every 2–3 hours during the experiments. Bonding agents, such as silicon rubber compound or rigid bond with an adhesive such as cyanoacrylate, may provide good ultrasound transmission (comparable to wet couplants) and a relative strong bond if a thin adhesive layer is achieved with no air bubbles. However, the ultrasound performance of the bond and the long-term stability need to be studied for our application.

6.5.2 Alumina Refractory Waveguide

Unfortunately, the thermocouple on z_4 lost its functionality after this test. Its out sheathing was burned, became brittle, and the inner wires were exposed with any subsequent handling. The alumina waveguide had no visually detectable changes after 5 days, nonstop in a high-temperature environment inside the OFC. Limited ash deposit was found on its distal end and no surface corrosion was observed. However, significant and irreversible deterioration in ultrasonic signal strength was revealed. This indicates that this alumina experienced strong elastic prop-

erty changes during the high-temperature tests, mainly caused by microstructure changes. Grain growth is the major contributor to the microstructure changes, which is shown as an increase in size of grains (crystallites) in a material at high temperature, commonly seen in metals, minerals, and ceramics. This happens when recovery and recrystallization are complete and further reduction in the internal energy can only be achieved by reducing the total area of the grain boundary [88].

Grain boundaries have associated macroscopic and microscopic degrees of freedom, which play the essential role in controlling the dynamic growth/depletion of grains under specific thermal conditions. Excess free energy of grain boundaries imply a driving force for reduction in total area of grain boundary, as a result of grain size growth and number of grains per volume reduction. The characteristics of grain growth have been shown by Mullins [71] to be related to the kinetics of grain growth. The rate of change of the mean grain size, dr/dt, must be related to the migration rate of boundaries in the system. The mechanism for ideal grain growth and a quantitative relationship to a single measure of the microstructure gives us:

$$\upsilon = \frac{dr}{dt} = M\zeta\kappa, \tag{6.1}$$

where υ is the velocity of a grain boundary, M is grain boundary mobility, ζ is the grain boundary energy, and κ is the sum of the two principal surface curvatures. Integral of Equation 6.1 obtains:

$$r^2 - r_{t=0}^2 = M\zeta\kappa t, \tag{6.2}$$

where r is the final grain size and $r_{t=0}$ is the initial grain size. Grain growth is irreversible and strongly temperature-dependent. High-temperature environment would accelerate the grain growth rate. To mitigate the grain growth problem for refractories that are required to process at high temperature, a variety of dopants, such as MgO, CaO, and SiO_2, are often used to inhibit grain growth.

Figure 6.18 shows the SEM images of grain size distribution changes for alumina refractory Rescor 960 with heat treatment, obtained from FEI NovaNano 630 with magnification over 13000x. A green alumina rod sample without fire has a relative

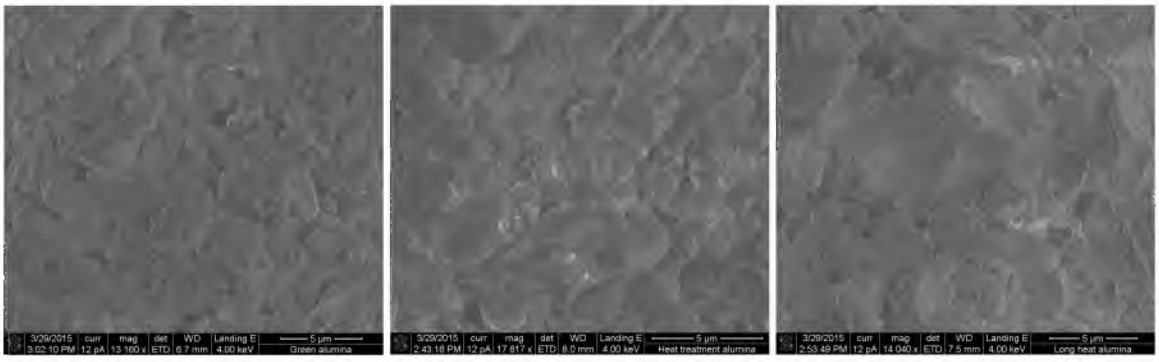

Figure 6.18: SEM images of alumina grains distribution under over 13000x magnification for alumina refractory Rescor 960 sample without heat treatment (A) short-term heat treatment (B) and long-term heat treatment (C)—pilot-scale tested alumina waveguide.

uniform particle size distribution, between 1 and 5 μm, in Figure 6.18(A). After short-term exposure to high temperature, over 800°C for less than 100 hours, the grain growth symptom has appeared on the alumina sample where the percentage of particles with larger size increases, shown in Figure 6.18(B). Figure 6.18(C) revealed the grain growth results for an alumina rod with heat treatment up to 1300°C, totalling over thousands of hours. One single particle almost has consumed its surrounding particles and its size is way over the whole image.

When the mean grain diameter of our alumina ceramic waveguide increases, the inhomogeneity causes stronger scattering and absorption of ultrasonic energy and increases the attenuation significantly, and the ultrasound reflected echoes from internal echogenic features cannot be identified. In addition, this observation indicates that we can monitor certain mechanical properties changes of the refractory material and detect the changes prior to the visible degradation or damage of the refractory.

CHAPTER 7

REFRACTORY WAVEGUIDE SELECTION

7.1 Potential Refractory Waveguide

Ultrasound tests with the alumina refractory rod severed as the propagating waveguide has shown promising results on temperature measurement over 1000 °C in lab-scale and pilot-scale OFC experiments. However, the experiments also revealed the limitations of alumina under an extreme environment for an extended time of operation because grain growth would deteriorate the ultrasound waveform for TOF determination. Therefore, the search for potentially the best candidates used as an ultrasound propagating waveguide at high temperatures continue.

7.1.1 Zirconia

Zirconia (ZrO_2) ceramic is a hard, corrosion and erosion resistant material. Zirconia-based ceramics are known for their excellent electronic, thermal, and optical properties. The combinations of these properties and the ability to manipulate its structure by doping makes zirconia useful in various applications including medical implants, catalysis, ionic conductors in solid fuel cells, in toughening nanocomposites, and as a refractory. The highest continuous working temperature for zirconia can be up to 2400 °C.

Zirconia can exist in three crystalline structures, namely monoclinic (M), tetragonal (T), and cubic (C). At room temperature, zirconia is stable in the monoclinic structure and changes to the tetragonal structure at about 1100 °C, transforming to cubic structure at about 2300 °C, upon heating. The phase transformations are reversible upon cooling with the tetragonal to monoclinic transformation being the most studied. The transformation of pure zirconia from the M-phase to the T-phase is accompanied by a volume increase of about 4–5% causing cracking and

structural failure. This volume change makes pure zirconia unsuitable for most applications.

7.1.1.1 Cubic Zirconia

This single crystal form of zirconia is optically colorless, transparent, has a relatively low fracture toughness and strength, but very high thermal shock resistance. This form is often used in jewelry as a diamond substitute.

Although it retains many properties including corrosion resistance at extremely high temperatures, zirconia does exhibit structural changes that may limit its use to perhaps only 500 °C. It also becomes electrically conductive as that temperature is approached.

This phase induces a partial cubic crystal structure instead of fully tetragonal during initial firing, which remains metastable during cooling. Upon impact, the tetragonal precipitates undergo a stress-induced phase transformation near an advancing crack tip. This action expands the structure as it absorbs a great portion of energy, and is the cause of the high toughness of this material. Reforming also occurs dramatically with elevated temperature and this negatively affects strength along with 3–7% dimensional expansion. The amount of tetragonal phase can be controlled by additions of the blends to balance toughness against loss of strength. To stabilize the high temperature T-phase at room temperature, appropriate amounts of divalent, trivalent, or lanthanide oxides such as MgO, CaO, CeO_2, and Y_2O_3 can be alloyed to pure zirconia. This was found to give zirconia-based ceramics high strength and exceptionally high fracture toughness for a ceramic.

7.1.1.2 Zirconia PSZ

Zirconia blends with approximately 10% MgO, called partially stabilized zirconia (PSZ), which is cream colored and has high toughness retained at elevated temperatures. These blends are lower in cost but also have larger grain structure, which is undesirable in our application since larger grains scatter ultrasound energy.

7.1.1.3 Zirconia TZP

Zirconia blends with approximately 3% yttria are called tetragonal zirconia polycrystal (TZP) and have the finest grain size with uniform sizes in 0.2–1 μm range. These grades exhibit the highest toughness at room temperature, because they are nearly 100% tetragonal, but this degrades severely between 200 and 500 °C as these irreversible crystal transformations also cause dimensional change. Zirconia TZP represents the most important class of zirconia ceramics.

As was previously mentioned, zirconia undergoes phase transformation under certain temperature and pressure conditions. The phase equilibrium in zirconia systems known to produce stabilized zirconia ceramics is shown in Figure 7.1, which is reproduced from the study of Scott [92].

The sample we selected to serve as a refractory waveguide contains 3–5 mol% yttria dopant, which was found to be sufficient to stabilize the T-phase at room temperature. The T-phase can be retained to room temperature as there is not a sufficient amount of energy for the T-M transformation to occur. The transforma-

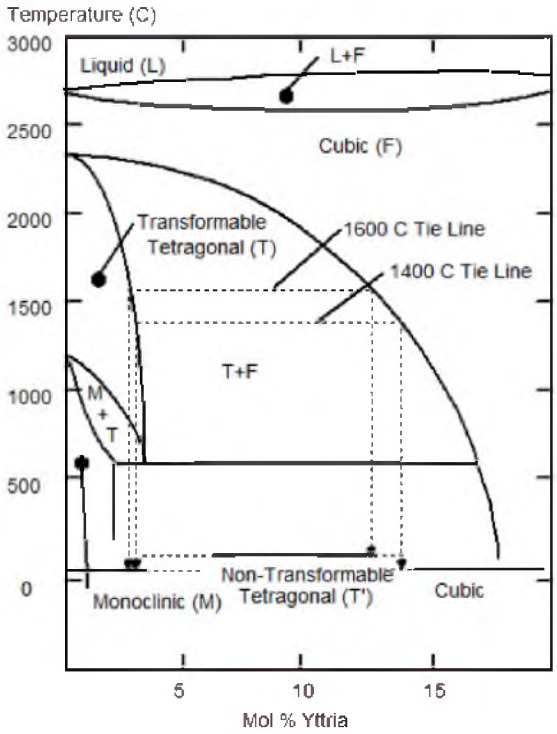

Figure 7.1: Phase diagram for the zirconia rich portion of the zirconia-yttria system reproduced from the study of Scott [92].

tion temperatures fall with yttria concentration and the tetragonal or cubic phase may become stable or metastable at room temperature. Doping was found to reduce the T-M transformation temperature from 1100°C to approximately 550°C. Below that temperature, it is in monoclinic and cubic (M+C) phase. Above the M+C phase field, there is a small monoclinic and tetragonal (M+T) phase field. At higher temperatures, the system has a transformable tetragonal phase field, about 750°C. This phase transformation affects the propagation of the ultrasound signal, which will be discussed later in this chapter.

7.1.2 Nitrides

Aluminum nitride (AlN) is stable at high temperatures in inert atmospheres and melts at 2800°C. In the air, surface oxidation occurs above 700°C, and even at room temperature, surface oxide layers of 5–10 nm have been detected. This oxide layer protects the material up to 1370°C. Above this temperature, bulk oxidation occurs, which becomes the limitation for our ultrasound application. AlN has high thermal conductivity, especially in comparison with traditional refractory material used in industry.

7.1.3 Carbides

7.1.3.1 Silicon Carbide

Silicon carbide is among the hardest of ceramics, and retains its hardness and strength at high temperatures, which translates into some of the best wear resistance available. SiC has a high thermal conductivity, especially in the chemical vapor deposition grade, which aids in thermal shock resistance. This material is relatively light at approximately half the density of steel. Based on the combination of hardness, resistance to wear, heat, and corrosion, SiC is often selected for seal faces and high performance pump parts.

Reaction bonded SiC has the lowest production cost but is characterized by coarse grains, which is undesirable in our application. It provides somewhat lower hardness and higher thermal conductivity. Direct sintered SiC is higher grade material than the reaction bonded form of silicon carbide and is commonly selected for high-temperature applications (e.g., optical temperature sensors [60]).

However, the highest working temperature of silicon carbide is approximately 1500 °C, which is below our desired range.

7.1.3.2 Tungsten Carbide

Tungsten carbide has a high melting point of 2870 °C. In its most basic form, tungsten carbide is a fine gray powder, but it can be pressed and formed into shapes for use in industrial machinery, cutting tools, abrasives, armor-piercing rounds, other tools, instruments, and jewelry.

Tungsten carbide is approximately two times stiffer than steel, with a Young's modulus of approximately 550 GPa, and is much denser than steel or titanium. Because of its extreme hardness, it can only be polished and finished with abrasives of superior hardness such as cubic boron nitride and diamond. We do not have capabilities to machine tungsten carbide parts to create echogenic features in waveguides. We were also unable to find suppliers willing to fabricate small-volume evaluation tungsten carbide parts at a reasonable cost.

7.2 Ultrasound Properties of Zirconia

Following our evaluation, we selected AmZirOx 86 Zirconia from Astro Met, Inc.—yttria-stabilized zirconia ceramic (Y-TZP) as our new waveguide which will replace the previously used alumina rod. The geometry of the Y-TZP waveguide was kept the same as before: a 12-inch rod with 1-inch diameter (Figure 7.2). Four small holes, located at 1, 2, 4, and 6 inches from the distal end of the waveguide, were introduced into the waveguide during manufacturing to create a train of ultrasound echoes. In this new waveguide, we reduced the size of echogenic holes to 1/32 inch. The original color of this sample was light caramel. It has precise shape, size, and highly polished finish. The material was doped with 5% yttria and had a bulk density of 6.01 g/cm^3. The maximum working temperature of this

Figure 7.2: Yttria stabilized zirconia rod as received from Astro Met, Inc..

material is expected to be 2400°C (4350°F).

The ultrasound testing at room temperature shows good SNR. The waveforms obtained with two different transducers with central frequencies of 5 MHz and 10 MHz are shown in Figures 7.3. Both waveforms are clear and echoes correctly indicate the presence of echogenic features in expected locations. A 5 MHz transducer produced a more detailed waveform. In addition to the expected echoes from the introduced echogenic features, the response indicated the presence of unexpected echoes indicated by red arrows. A 10 MHz transducer produced a cleaner echo signal but required a high level of ultrasound excitation, indicating an expected increase in ultrasound dissipation at higher frequencies. Unexpected echoes were present in this case as well.

In Figure 7.3, echoes marked by red arrows were unexpected. They are equally delayed from echoes produced by echogenic holes placed along the length of the waveguide. Delayed echoes appearing in alumina waveguide reflected from its distal end are due to the ultrasound propagating mode conversion between the longitudinal and shear wave. The cause for the delayed echoes in zirconia is completely different. Based on the equal delay symptom for every echogenic hole and distal end, we conclude that unexpected echoes are produced by the ultrasound

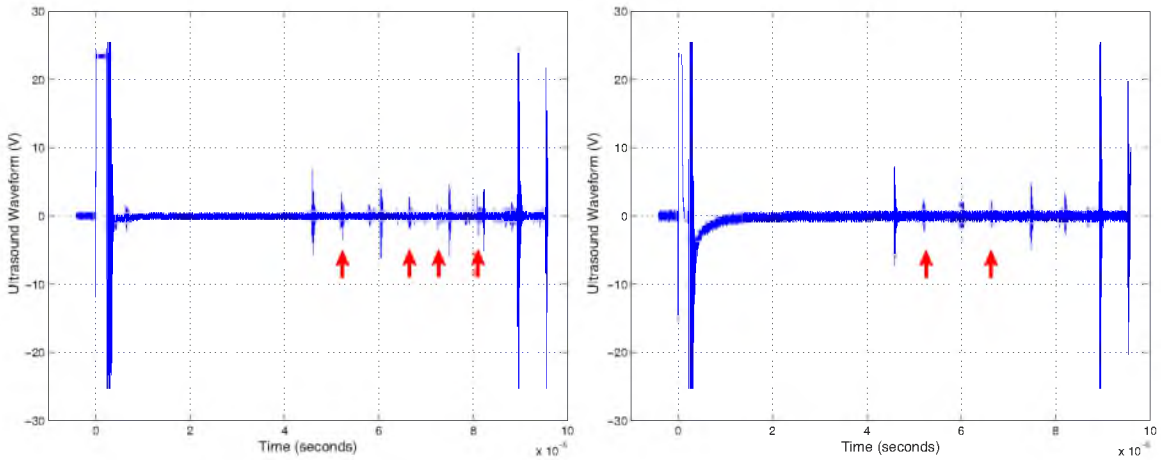

(a) Transducer V609 with frequency of 5 MHz (b) Transducer V611 with frequency of 10 MHz

Figure 7.3: The ultrasound echo waveforms obtained with this zirconia rod. The response at 9 μs is produced by the distal end of the sample and is preceded by four partial internal echoes produced by the drilled holes. Panels (a) and (b) show responses obtained with transducers having 5 and 10 MHz central frequencies.

signal traversing the couplant gel, between the transducer and the proximal end twice, as illustrated in Figure 7.4. This gel is water-based, and has much smaller density and slower speed of sound than zirconia, causing significant ultrasound impedance mismatch, leading to the ultrasound signal bouncing between the surface of the transducer and zirconia waveguide. Though the thickness of the couplant is only on the order of 1/32 inch, a relatively low density (0.983 g/cm^3) and slow speed of sound (1516 m/s) in the gel causes a delay of 2.4625 μs for a single pass through the couplant. A round trip through the couplant (excitation path II in Figure 7.4) will result in a delay close to 5 μs —the value consistent with the results in Figure 7.3. By carefully adjusting the thickness of the coupling gel, we confirmed that unexpected echoes in Figure 7.3 are indeed caused by an ultrasound signal partially bouncing between the transducer and the waveguide.

The coupling medium can cause transit time errors on the order of 1 percent of the measured values for velocity measurements. Due to partial transmission and partial reflections of sound energy in the couplant layer, there may be a change of shape of the waveform which can further affect velocity measurement accuracy [36]. Thus, a proper couplant should be carefully chosen for accurate TOF measurement.

Initial testing of the "as received" waveguide showed significant deterioration

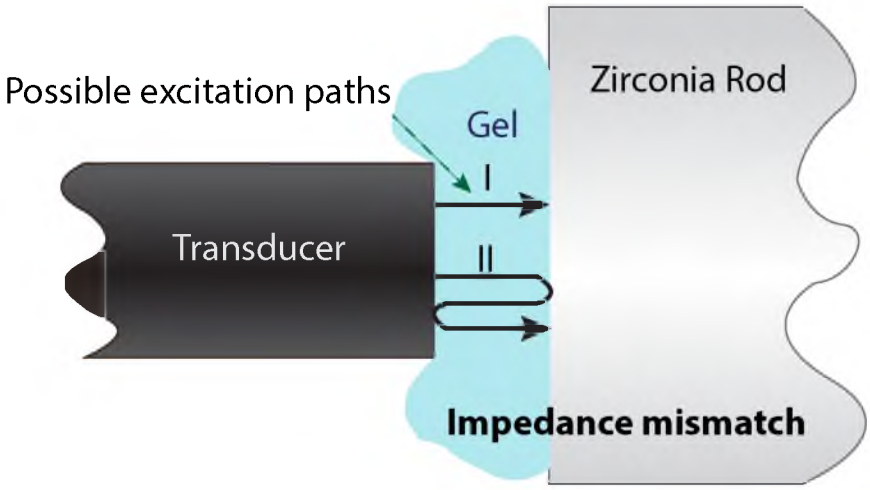

Figure 7.4: Unexpected echoes in Figure 7.3 are caused by multiple ultrasound reflections between the transducer and the zirconia waveguide.

of the ultrasound signal quality at high temperatures, which we attributed to the change in the crystal structure of the material. Signal strength recovered after the sample was cooled to the room temperature. We observed that heat treatment also changed the color of the sample. Figure 7.5 illustrates the whitening of the sample as a result of heating. The original waveguide was hot isostatically pressed into the final shape at a slightly reducing atmosphere, thus altering the stoichiometry through depletion of oxygen. Thermal treatment on the sample in air reintroduced the oxygen and whitened the sample.

Several additional thermal treatments were used to investigate the effect of annealing on the strength of the ultrasound signal. The two-stage sintering process helped reduce the rate of the grain size growth, concluded from studies from Rhodes [86] and Yu et al. [107]. First, the sample was kept at 1400 °C for 2 hours and then at 1200 °C for 5 hours. After the sintering, the signal at room temperature did not change, but the strength of echo signals from the echogenic features improved significantly even as the sample was heated to 1000 °C. Further sintering of the sample for two days did not result in additional significant improvement in the quality of the ultrasound waveforms of echo signals.

7.3 Experiments

We obtained the empirical correlation between the speed of sound and the temperature using the experimental setup similar to the one used to characterize alumina waveguide. The test temperature range was the same as the setup for alumina waveguide tests, which is depicted in Figure 4.6. An ultrasound data acquisition and analysis system was kept the same as previous calibrating alumina

Figure 7.5: Waveguide color changes after heat treatment. Top: Color gradient indicates oxidization of the hottest area. Bottom: The whole sample became white after high temperature sintering at a uniform temperature distribution.

tests. The experimental procedure did not change for zirconia ceramic, all 6 repeats. Randomized temperature points from 50 to 1150 °C with 50 °C increment and room temperature were obtained for calibrating the relationship between SOS versus temperature. Independent temperature measurements were provided by an OMEGA® Nextel ceramic insulated thermocouple that was attached to the distal end of the waveguide. Four 1/32-inch OMEGA Super OMEGACLAD® thermocouples were bent and inserted into engineered echogenic features/holes to provide independent and more accurate temperature measurements than surface attachment, as shown in Figure 7.6. These thermocouples were connected to data acquisition system DATAG DI-1000-TC for real-time temperature monitoring.

Figure 7.7 shows that the strength of echoes originating from echogenic features placed along the length of the ultrasound propagation path and the SNR change with temperature (compare echo waveforms produced by the same echogenic feature and acquired at different temperatures and marked with red triangles). Below 400 °C, the signal to noise ratio is high but then degrades significantly as temperature increases to reach the range between 450 and 650 °C. The reduction of the signal quality leads to poor SNR and high excitation energy required to obtain usable ultrasound echoes. Further temperature increase above 700 °C improves the quality of the echo waveforms and increases the SNR. At high temperatures, strong and clean signals are back. We observe that 450 to 650 °C corresponds to the temperature range where structural transformations occur in Y-TZP— from monoclonal and cubic to tetragonal and cubic. This structural transformation is likely the reason the attenuation of ultrasound is higher in this temperature range.

Figure 7.6: The placement of thermocouples used during real-time temperatures monitoring.

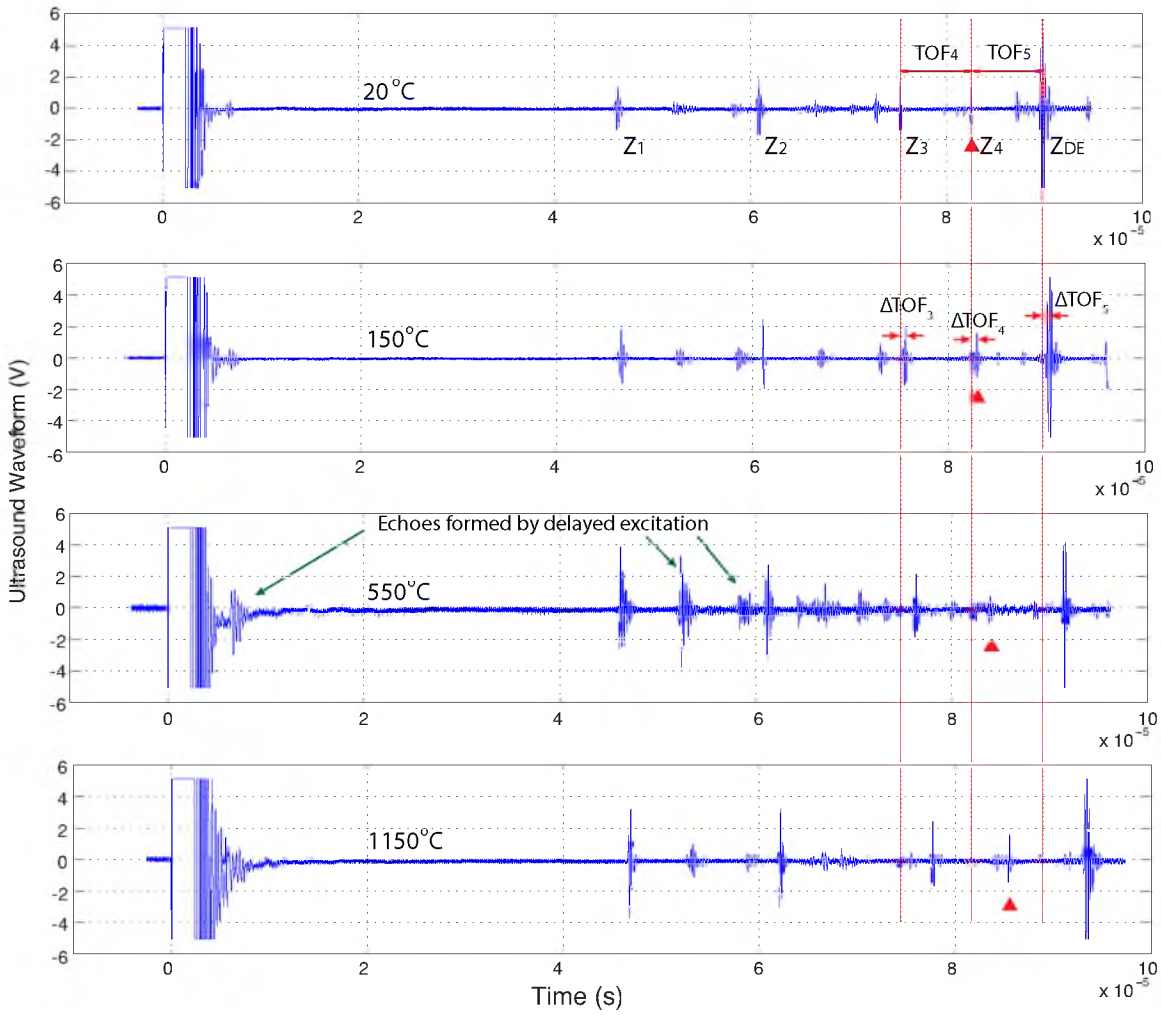

Figure 7.7: Echo waveforms collected at different temperatures. The strength of the signal changes with temperature as crystal structure changes in the waveguide material at different temperatures. Strong temperature dependence of the SOS is evident as temperature increases from room temperature to 1150°C.

7.4 The SOS Dependence on Temperature

Figure 7.8A shows the experimental correlation between the speed of sound of the yttria stabilized zirconia and the temperatures. As discussed in Chapter 4, compensation for thermal expansion is not essential as long as the same calculations for the SOS are used to construct the SOS versus temperature relationship and to infer the temperature from the measurements of the change in the TOF of ultrasound echoes. The result shown in Figure 7.8 is not compensated for thermal expansion.

Figure 7.8A also presents the SOS versus temperature relationship or alumina

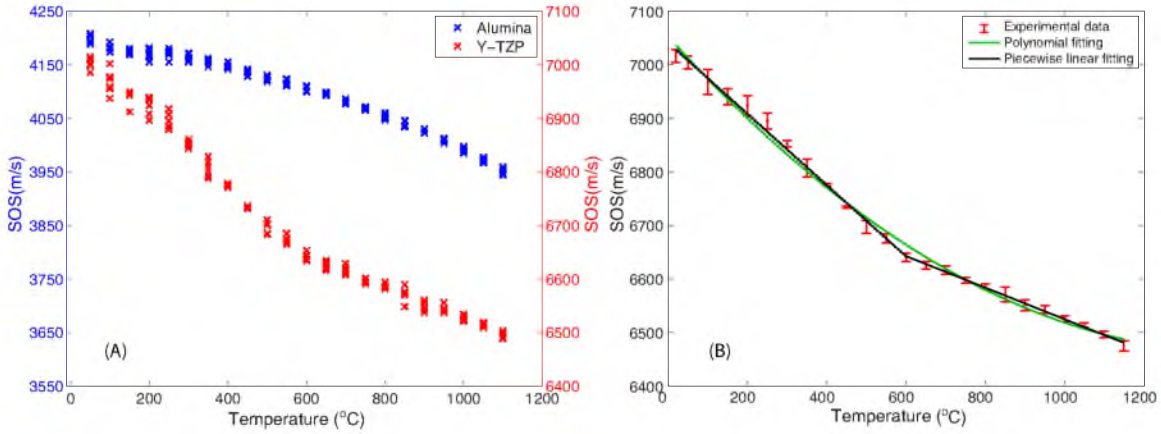

Figure 7.8: The SOS versus temperature relationship comparison of waveguides of alumina (primary y-axis) and zirconia (secondary y-axis) (A). Both piecewise linear and polynomial fitting models are used to illustrate the SOS and temperature calibration results (B).

waveguide used in previous tests. The slope of SOS curve for zirconia is steeper than the alumina. A more complex behavior is also evident from the examination of the results. Several temperature ranges are associated with different SOS versus temperature slopes. For example, the temperature dependence is the strongest when the temperature is between 400 and 600°C, which is the range where the phase transformation from M+C to M+T structure occurs.

Two fitting models were used to describe the correlation between the SOS and temperature for the Y-TZP sample, shown in Figure 7.8B. The piecewise linear model is expressed as

$$c(T) = \begin{cases} -0.66T + 7041.14 & 20\,^{\circ}\mathrm{C} \le T \le 599.22\,^{\circ}\mathrm{C} \\ -0.29T + 6819.33 & 599.22\,^{\circ}\mathrm{C} \le T \le 1150\,^{\circ}\mathrm{C} \end{cases} \tag{7.1}$$

with the coefficient of determination of 0.995.

The quadratic model fitting gives the following correlation:

$$c(T) = 2.84e-4T^2 - 0.82T + 7052.55. \tag{7.2}$$

The coefficient of determination for polynomial model is 0.994, less accurate than the piecewise linear model in the 500–700°C range.

The Young's modulus calculated based on SOS measurement for YSZ is shown in Figure 7.9. The calculated Young's modulus based on long rod Equation 2.7

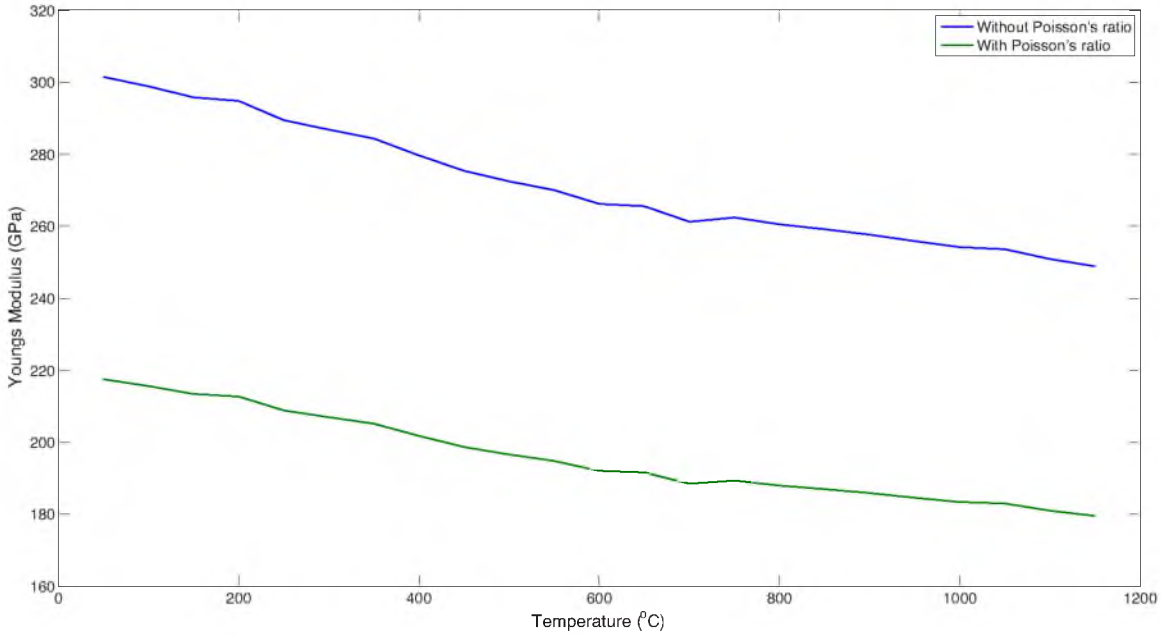

Figure 7.9: The calculated Young's modulus as function of temperature based on experimental SOS results.

at room temperature is 303.39 GPa; this value becomes 218.88 GPa if Equation 2.5—including Poisson's ratio (assuming constant)—is applied with manufacture properties. The manufacturer-provided Young's modulus value is 204 GPa, very close to our experimental result. Moreover, the great difference between these two estimated Young's modulus approaches shows the long, thin rod Young's modulus approximation indeed is not suitable for our waveguide. The manufacturer properties data are listed in Table 7.1, with the comparison of our results from ultrasound measurements.

Table 7.1: AmZirOx 86 zirconia properties

Property (20°C)	Manufacturer	Experiment
Density (g/m^3)	6.01	6.16
Young's modulus (GPa)	204	218.88
Poisson's ratio	0.31	-
Thermal expansion (10^{-6}/ °C)	10.3	-

CHAPTER 8

CONCLUSIONS AND FUTURE WORK

In this dissertation, the history and evolution of the ultrasound measurements of a segmental temperature distribution system is described. Our conclusion is that this noninvasive approach provides a very powerful abstraction for solving challenging problems on long-term temperature monitoring for an extreme environment such as gasifiers that conventional temperature sensors are incapable to use. This US-MSTD system is also a potential alternative for the optical techniques when the optical access ports are impractical, a novel approach if point of interest is inaccessible, and more comprehensive even if prior heat flow information to reconstruct the temperature is not incorporated.

The ultrasound approach for the temperature distribution determination is to construct segmented structures or embed a segmented waveguide which requires minimal changes on the existing structures and estimate the time of flight for each segment based on collected partial ultrasound reflections as the ultrasound excitation pulse propagates through the scattered waveguide. Therefore, the temperature distribution along the ultrasonic propagating waveguide can be interpreted based on the time of flight and the predetermined correlation between the speed of sound and temperature on this particulate waveguide material.

During this research, we solved the challenge of the feasibility of creating partial internal reflectors on waveguides from cementitious materials to high-temperature advanced ceramics. We introduced a noise-robust reduction method that applies an anisotropic diffusion filter to ultrasonic waveform envelopes to achieve a consistent and accurate time of flight estimation for dissipative and distortive media. We constructed our ultrasound measurement system to determine the speed of sound dependence on temperature for refractories such as alumina and yittria-stabilized

zirconia. We designed and developed a specialized data acquisition and analysis system to provide a real-time visualized temperature distribution monitoring and heat flux determination.

The ultrasound temperature measurement system was successfully tested during a pilot-scale oxyfuel combustor campaign. Real-time temperature distributions across the refractory were captured during all relevant process changes. The comparison of temperature results based on the US-MSTD method and thermocouple measurements exhibits excellent consistency. We are sufficiently encouraged by the results based on field tests to proceed with the construction of an automated system that incorporates multisensor arrays on the entire combustor to provide a 3D temperature distribution profile.

In addition to applications involving the internal temperature distribution estimation, plans are underway for expanding the method to the characterization of the micro- and macromechanical property changes as function of temperature for refractory, metals, and other materials. Therefore, significant anomalies and discontinuities, such as cracks in bricks or developments of a brittle zone, can be immediately identified during the operation, allowing for a better maintenance scheduling and safer operations of gasifiers. In addition, detection of refractory build-up and estimation of its thickness provides means for the gasifier process optimization that can extend the campaign life substantially.

The wide range, fine resolution, fast response to temperature change, rapid availability of a large data set, free from temperature drifts, and continuous operation at elevated temperature environments will permit us to apply this promising new technique to research on energy conversion containers, material production, casting industrial, food process, and other emerging manufactures.

There are several potential research topics to improve and expend this research further. A long-term temperature monitoring can be achieved if a good contact between the transducer and its attached waveguide surface is implemented. A more accurate temperature distribution performance by the ultrasound approach may be achieved if the sizes and spaces of the internal echogenic structures are optimized. The temperature resolution can be guaranteed if the data acquisi-

tion system has a high resolution and high sample rate for the TOF estimations. Additionally, a more robust, de-noise, and efficient signal processing technique, especially for TOF measurements, would significantly improve the accuracy of the temperature implementation. It might be hard to find a universal ultrasonic propagating waveguide material to be suitable for use in different temperature ranges and under various environmental conditions. These aspects that should be evaluated for finding the most suitable waveguide material may include but are not limited to the density, elastic properties, chemical composition, porosity, grain size distribution, macro- and microstructure homogeneity, and grain structure responses to heat treatment, etc.

This research was only focused on using longitudinal waves for the SOS measurement. The shear wave, as well as the surface acoustic wave (SAW), may be used for a surface temperature distribution monitoring. This proposed US-MSTD system has no limit on the size of the testing object. This system can be used on a huge container such as the nucleation reactor vessel, or as a temperature controller for a nanostructured semiconducting oxidization process.

REFERENCES

[1] Arthur, R., Trobaugh, J., Straube, W., and Moros, E. Temperature dependence of ultrasonic backscattered energy in motion compensated images. *IEEE Trans. Ultrasonics, Ferroelectric and Frequency Control 52* (2005), 1644–1652.

[2] Auld, B. A. *Acoustic fields and waves in solids*, vol. 2. RE Krieger, 1990.

[3] Balasubramaniam, K., Shah, V. V., Costley, R. D., Boudreaux, G., and Singh, J. P. High temperature ultrasonic sensor for the simultaneous measurement of viscosity and temperature of melts. *Review of Scientific Instruments 70*, 12 (1999), 4618–4623.

[4] Baskaran, G., Balasubramaniam, K., and Rao, C. L. Shear-wave time of flight diffraction (s-tofd) technique. *NDT & E International 39*, 6 (2006), 458 – 467.

[5] Baudson, H., Debucquoy, F., Huger, M., Gault, C., and Rigaud, M. Ultrasonic measurement of young's modulus mgo/c refractories at high temperature. *IEEE Trans. Ultrasonics, Ferroelectric and Frequency Control 19* (1999), 1895–1901.

[6] Bennett, J., and Kyei-Sing, K. Refractory liner materials used in slagging gasifiers. *Refractory Applications and News 9* (2004), 20–25.

[7] Bennett, J. P., Krabbe, R., Kwong, J., and Thomas, H. Improved temperature sensing in slagging gasifiers. In *23rd Annual Conference on Fossil Energy Materials* (May 12-14, 2009).

[8] Bennett, J. P., Kwong, J., Petty, A., Powell, C., Thomas, H., and Krabbe, R. Field trial results of netl's phosphate-modified high chrome oxide refractory material for slagging gasifiers. In *Gasification Technologies Conference, San Francisco, Oct* (2007), Citeseer, pp. 14–17.

[9] Bennett, J. P., and Kwong, K.-S. Failure mechanisms in high chrome oxide gasifier refractories. *Metallurgical and Materials Transactions A 42*, 4 (2011), 888–904.

[10] Bentley, R. Thermocouple materials and their properties. *Theory and Practice of Thermoelectric Thermometry: Handbook of Temperature Measurement* (1998), 25–81.

[11] Bhatia, A. B. *Ultrasonic absorption.* Clarendon Press, 1967.

[12] Black, M., Sapiro, G., Marimont, D., and Heeger, D. Robust anisotropic diffusion. *IEEE Transactions on Image Processing 7*, 3 (Mar 1998), 421–432.

[13] Blitz, J., and Simpson, G. *Ultrasonic methods of non-destructive testing*, vol. 2. Springer Science & Business Media, 1996.

[14] Bouda, A. B., Lebaili, S., and Benchaala, A. Grain size influence on ultrasonic velocities and attenuation. *NDT & E International 36*, 1 (2003), 1–5.

[15] Bramanti, M., Tonazzini, A., and Tonazzini, A. An acoustic pyrometer system for tomographic thermal imaging in power plant boilers. *Measurement Science and Technology 45* (1996), 87–94.

[16] Brennan, R. E. *Ultrasonic nondestructive evaluation of armor ceramics*. ProQuest, 2007.

[17] Brooker, D. D., Falsetti, J. S., Pertuit, A. J., Vuong, D.-C., and Wolfenbarger, J. K. Gasifier monitoring apparatus, Sept. 10 1996. US Patent 5,554,202.

[18] Carovac, A., Smajlovic, F., and Junuzovic, D. Application of ultrasound in medicine. *Acta Informatica Medica 19*, 3 (2011), 168.

[19] Chakraborty, S., Sarkar, S., Gupta, S., and Ray, A. Damage monitoring of refractory wall in a generic entrained-bed slagging gasification system. *Proceedings of the Institution of Mechanical Engineers, Part A: Journal of Power and Energy 222*, 8 (2008), 791–807.

[20] Champagne, B., Eizenman, E., and Pasupathy, S. Exact maximum likelihood time delay estimation for short observation intervals. *IEEE Transactions on Signal Processing 39*, 6 (Jun 1991), 1245–1257.

[21] Chen, E.-S. *Behavior of refractory linings for slagging gasifiers*. PhD thesis, Massachusetts Institute of Technology, 1984.

[22] Christensen, D. *Ultrasonic bioinstrumentation*. Wiley, 1988.

[23] de Faoite, D., Browne, D. J., Chang-Díaz, F. R., and Stanton, K. T. A review of the processing, composition, and temperature-dependent mechanical and thermal properties of dielectric technical ceramics. *Journal of Materials Science 47*, 10 (2012), 4211–4235.

[24] de Korte, C., van der Steen, A., Dijkman, B., and LancÃłe, C. Performance of time delay estimation methods for small time shifts in ultrasonic signals. *Ultrasonics 35*, 4 (1997), 263 – 274.

[25] Department of Energy, N. E. T. L. Coal gasification systems. From http://www.netl.doe.gov/research/coal/energy-systems/gasification/, 2011.

[26] Dils, R. High-temperature optical fiber thermometer. *Journal of Applied Physics 54*, 3 (1983), 1198–1201.

[27] Dogan, C. P., Kwong, K.-S., Bennett, J. P., and Chinn, R. E. Improved refractories for slagging gasifiers in igcc power systems. *DOE Report 835687* (2003).

[28] El Guerjouma, R., Mouchtachi, A., Jayet, Y., and Baboux, J. Nondestructive evaluation of graphite by ultrasonic velocity measurement using cross-correlation and hilbert transform methods. In *Proceedings of IEEE Ultrasonics Symposium* (Oct 1992), pp. 829–832 vol.2.

[29] Ensminger, D. *Ultrasonics: Fundamentals, technology, applications, revised and expanded*. CRC Press, 1988.

[30] Erikson, K. R., Fry, F. J., and Jones, J. P. Ultrasound in medicine-a review. *Sonics and Ultrasonics, IEEE Transactions on 21*, 3 (1974), 144–170.

[31] Forbes, A. Acoustic monitoring of global ocean climate. *Sea Technology; (United States) 35*, 5 (1994).

[32] Gault, C., Huger, M., Auvray, J., Soro, J., and Yeugo Fogaing, E. Contribution of high temperature ultrasonic measurements to investigations of thermomechanical behaviour of refractories. In *10th International Conference and Exhibition of the European Ceramic Society* (2007).

[33] Gerig, G., Kubler, O., Kikinis, R., and Jolesz, F. Nonlinear anisotropic filtering of MRI data. *IEEE Transactions on Medical Imaging 11*, 2 (Jun 1992), 221–232.

[34] Green, S. An acoustic technique for rapid temperature distribution measurements. *J. Acoustical Society of America 77* (1985), 765–769.

[35] Green, S. F. An acoustic technique for rapid temperature distribution measurement. *Journal of the Acoustical Society of America 77*, 2 (1985), 759 – 763.

[36] Green Jr, R. E. Ultrasonic nondestructive materials characterization. In *Analytical Ultrasonics in Materials Research and Testing*. DTIC Document, 1984, pp. 1–29.

[37] Grobnic, D., Mihailov, S. J., Smelser, C. W., and Ding, H. Sapphire fiber bragg grating sensor made using femtosecond laser radiation for ultrahigh temperature applications. *Photonics Technology Letters, IEEE 16*, 11 (2004), 2505–2507.

[38] Grobnic, D., Smelser, C. W., Mihailov, S. J., and Walker, R. B. Long-term thermal stability tests at 1000°C of silica fibre bragg gratings made with ultrafast laser radiation. *Measurement Science and Technology 17*, 5 (2006), 1009.

[39] Guo, R., Cheng, G., and Wang, Y. Texaco coal gasification quality prediction by neural estimator based on dynamic pca. In *IEEE International Conference on Mechatronics and Automation* (2006), pp. 2241–2246.

[40] Hanscombe, P. A., and Richards, P. N. Distributed temperature sensor, Feb. 15 1994. US Patent 5,286,109.

[41] Hedrick, W. R., Hykes, D. L., and Starchman, D. E. *Ultrasound physics and instrumentation*. Elsevier Mosby, 2005.

[42] Heyman, J. S., and Malyarenko, E. V. Dynamic acoustic thermometer, July 29 2008. US Patent 7,404,671.

[43] Higman, C., and van der Burgt, M. *Gasification*, 2nd ed. Gulf Professional Publishing, Burlington, MA, 2008.

[44] Hornick, M. J., and McDaniel, J. E. The Tampa electric integrated gasification combined-cycle project, final technical report for project under cooperative agreement de-fc-21-91mc27363. Tech. Rep. united2002tampa, United States. Department of Energy, The U.S. Department of Energy, Office of Sossil Energy, National Energy Technology Laboratory, Morganton, West Virginia, August 2002.

[45] Hull, D., Kautz, H., and Vary, A. Measurement of ultrasonic velocity using phase-slope and cross-correlation methods. *Materials Evaluation 43*, 11 (1985), 1455–1460.

[46] Hussain, M. A., Alam, S. K., Lee, S. Y., and Hasan, M. K. Robust strain-estimation algorithm using combined radiofrequency and envelope cross-correlation with diffusion filtering. *Ultrasonic Imaging 34*, 2 (2012), 93–109.

[47] Ihara, I., Takahashi, M., and Yamada, H. A non-contact temperature sensing with ultrasound and the potential for monitoring heated materials. In *Sensors, 2009 IEEE* (2009), IEEE, pp. 1709–1714.

[48] J Lu, K Wakai, S. T., and Shimizu, S. Acoustic computer tomographic pyrometry for two-dimensional measurement of gases taking into account the effect of refraction of sound wave paths. *Measurement Science and Technology 11*, 6 (2000), 692 – 697.

[49] Jackson, J., Summan, R., Dobie, G., Whiteley, S., Pierce, S., and Hayward, G. Time-of-flight measurement techniques for airborne ultrasonic ranging. *Ultrasonics, Ferroelectrics, and Frequency Control, IEEE Transactions on 60*, 2 (February 2013), 343–355.

[50] Jacovitti, G., and Scarano, G. Discrete time techniques for time delay estimation. *IEEE Transactions on Signal Processing 41*, 2 (Feb 1993), 525–533.

[51] Jia, Y., Puga, M., Butterfield, A. E., Christensen, D. A., Whitty, K. J., and Skliar, M. Ultrasound measurements of temperature profile across gasifier refractories: Method and initial validation. *Energy and Fuels 27*, 8 (2013), 4270–4277.

[52] Jia, Y., and Skliar, M. Anisotropic diffusion filter for robust timing of ultrasound echoes. In *Ultrasonics Symposium (IUS), 2014 IEEE International* (2014), IEEE, pp. 560–563.

[53] Kleppe, J. Advances in acoustic pyrometry. *J. Acoust. Soc. Am. 99* (1996), 2535–2574.

[54] Kováčik, J. Correlation between Young's modulus and porosity in porous materials. *Journal of Materials Science Letters 18*, 13 (1999), 1007–1010.

[55] Krautkramer, J., and Krautkrâmer, H. *Ultrasonic Testing of Materials.* Cambridge Univ Press, 1990.

[56] Kwong, K., Petty, A., Bennett, J., Krabbe, R., and Thomas, H. Wear mechanisms of chromia refractories in slagging gasifiers. *International Journal of Applied Ceramic Technology 4*, 6 (2007), 503–513.

[57] Kychakoff, G., Hollingshead, A., and Boyd, S. Use of acoustic temperature measurements in the cement manufacturing pyroprocess. In *Cement Industry Technical Conference* (2005), pp. 23–33.

[58] Laugier, P., and Haïat, G. Introduction to the physics of ultrasound. In *Bone quantitative ultrasound.* Springer, 2011, pp. 29–45.

[59] Le, L. H. An investigation of pulse-timing techniques for broadband ultrasonic velocity determination in cancellous bone: a simulation study. *Physics in Medicine and Biology 43*, 8 (1998), 2295 – 2308.

[60] Lee, B. Review of the present status of optical fiber sensors. *Optical Fiber Technology 9*, 2 (2003), 57–79.

[61] Lee, Y., Khuri-Yakub, B., and Saraswat, K. Temperature measurement in rapid thermal processing using the acoustic temperature sensor. *IEEE Trans. Semiconductor Manufacturing 9* (1996), 115–121.

[62] Leininger, T. Design, fabrication and testing of an infrared ratio pyrometer system for the measurement of gasifier reaction chamber temperature. Tech. rep., GE Energy, Mar 2005.

[63] Lempriere, B. M. *Ultrasound and elastic waves: Frequently asked questions.* Academic Press, 2003.

[64] Li, C., Huang, L., Duric, N., Zhang, H., and Rowe, C. An improved automatic time-of-flight picker for medical ultrasound tomography. *Ultrasonics 49*, 1 (2009), 61–72.

[65] Liang, Q., Guo, X., Dai, Z., Liu, H., and Gong, X. An investigation on the heat transfer behavior and slag deposition of membrane wall in pilot-scale entrained-flow gasifier. *Fuel 102* (2012), 491–498.

[66] Lu, G., Yan, Y., Riley, G., and Bheemul, H. C. Concurrent measurement of temperature and soot concentration of pulverized coal flames. *Instrumentation and Measurement, IEEE Transactions on 51*, 5 (2002), 990–995.

[67] Malyarenko, E. V., Heyman, J. S., Chen-Mayer, H. H., and Tosh, R. E. High-resolution ultrasonic thermometer for radiation dosimetry. *The Journal of the Acoustical Society of America 124*, 6 (2008), 3481–3490.

[68] Mann, M., Seames, W., Shukla, D., Hong, X., and Hurley, J. Dynamic testing of gasifier refractory, the University of North Dakota. *US Department of Energy Grant* (2005).

[69] MartÃĐnez Bueno, M. J., AgÃijera, A., GÃşmez, M. J., Hernando, M. D., GarcÃĐa-Reyes, J. F., and FernÃąndez-Alba, A. R. Application of liquid chromatography/quadrupole-linear ion trap mass spectrometry and time-of-flight mass spectrometry to the determination of pharmaceuticals and related contaminants in wastewater. *Analytical Chemistry 79*, 24 (2007), 9372–9384.

[70] Minchener, A. J. Coal gasification for advanced power generation. *Fuel 84*, 17 (2005), 2222–2235.

[71] Mullins, W. The statistical self-similarity hypothesis in grain growth and particle coarsening. *Journal of Applied Physics 59*, 4 (1986), 1341–1349.

[72] Ng, D., and Fralick, G. Use of a multiwavelength pyrometer in several elevated temperature aerospace applications. *Review of Scientific Instruments 72*, 2 (2001), 1522–1530.

[73] O'Brien, W. D. Ultrasound–biophysics mechanisms. *Progress in Biophysics and Molecular Biology 93*, 1 (2007), 212–255.

[74] Papadakis, E. P. Grain-size distribution in metals and its influence on ultrasonic attenuation measurements. *The Journal of the Acoustical Society of America 33*, 11 (1961), 1616–1621.

[75] Parrilla, M., Anaya, J. J., and Fritsch, C. Digital signal processing techniques for high accuracy ultrasonic range measurements. *IEEE Transactions on Instrumentation and Measurements 40*, 4 (1991), 759–763.

[76] Perona, P., and Malik, J. Scale-space and edge detection using anisotropic diffusion. *IEEE Transactions on Pattern Analysis and Machine Intelligence 12*, 7 (Jul 1990), 629–639.

[77] Phillips, J. Different types of gasifiers and their integration with gas turbines. *The Gas Turbine Handbook* (2006).

[78] Pickrell, G., Zhang, Y., and Wang, A. Development of a temperature measurement system for use in coal gasifiers. In *19th Annual International Pittsburgh Coal Conference* (2002).

[79] Portune, A. R. *Nondestructive ultrasonic characterization of armor grade silicon carbide*. PhD thesis, Rutgers University, 2011.

[80] Praher, B., Straka, K., and Steinbichler, G. An ultrasound-based system for temperature distribution measurements in injection moulding: system design, simulations and off-line test measurements in water. *Measurement Science and Technology 24*, 8 (2013), 084004.

[81] Ragauskas, A., Daubaris, G., Ragaisis, V., and Petkus, V. Implementation of non-invasive brain physiological monitoring concepts. *Medical Engineering & Physics 25*, 8 (2003), 667 – 678. Cerebrovascular Modelling.

[82] Raghavan, A., and Cesnik, C. E. Review of guided-wave structural health monitoring. *Shock and Vibration Digest 39*, 2 (2007), 91–116.

[83] Ramalingam, R., and Neumann, H. Fiber Bragg grating-based temperature distribution evaluation of multilayer insulations between 300 k-77 k. *Sensors Journal, IEEE 11*, 4 (2011), 1095–1100.

[84] Rayleigh, J. W. S. B. *The theory of sound*, vol. 2. Macmillan, 1896.

[85] Reddy, B. Fundamental heat transfer mechanism between bed-to-membrane water-walls in circulating fluidized bed combustors. *International Journal of Energy Research 27*, 9 (2003), 813–824.

[86] Rhodes, W. Agglomerate and particle size effects on sintering yttria-stabilized zirconia. *Journal of the American Ceramic Society 64*, 1 (1981), 19–22.

[87] Rieker, G. B., Jeffries, J. B., and Hanson, R. K. Calibration-free wavelength-modulation spectroscopy for measurements of gas temperature and concentration in harsh environments. *Appl. Opt. 48*, 29 (Oct 2009), 5546–5560.

[88] Rollett, A., Humphreys, F., Rohrer, G. S., and Hatherly, M. *Recrystallization and related annealing phenomena*. Elsevier, 2004.

[89] Rosen, M. Analytical ultrasonics for characterization of metallurgical microstructures and transformations. In *In NASA. Lewis Research Center Analytical Ultrasonics in Materials Research and Testing* (1987), DTIC Document, pp. 79–97.

[90] Sarigul, I. Model-based estimation of adiabatic flame temperature during coal gasification. Master's thesis, University of Utah, 2012.

[91] Schmidt, P. L., Walker, D. G., Yuhas, D. J., and Mutton, M. M. Thermal measurements using ultrasonic acoustical pyrometry. *Ultrasonics 54*, 4 (2014), 1029–1036.

[92] Scott, H. Phase relationships in the zirconia-yttria system. *Journal of Materials Science 10*, 9 (1975), 1527–1535.

[93] Shen, Y., Tong, L., Wang, Y., and Ye, L. Sapphire-fiber thermometer ranging from 20 to 1800 c. *Applied Optics 38*, 7 (1999), 1139–1143.

[94] Simon, C., VanBaren, P., and Ebbini, E. S. Two-dimensional temperature estimation using diagnostic ultrasound. *Ultrasonics, Ferroelectrics, and Frequency Control, IEEE Transactions on 45*, 4 (1998), 1088–1099.

[95] Sukul, G., and Balaramakrishna, P. A review of refractory linings for gasification reactors. *Journal of the Australian Ceramics Society Volume 50*, 2 (2014), 83–92.

[96] Takahashi, M., and Ihara, I. Ultrasonic determination of temperature distribution in thick plates during single sided heating. *Modern Physics Letters B 22*, 11 (2008), 971–976.

[97] Taler, J., Duda, P., Węglowski, B., Zima, W., Grądziel, S., Sobota, T., and Taler, D. Identification of local heat flux to membrane water-walls in steam boilers. *Fuel 88*, 2 (2009), 305–311.

[98] Tipler, P. A., and Mosca, G. *Physics for scientists and engineers*. Macmillan, 2008.

[99] Tsiotsios, C., and Petrou, M. On the choice of the parameters for anisotropic diffusion in image processing. *Pattern Recognition 46*, 5 (2013), 1369–1381.

[100] Van Veen, S., Claas, E., and Kuijper, E. J. High-throughput identification of bacteria and yeast by matrix-assisted laser desorption ionization-time of flight mass spectrometry in conventional medical microbiology laboratories. *Journal of Clinical Microbiology 48*, 3 (2010), 900–907.

[101] Viola, F., and Walker, W. A comparison of the performance of time-delay estimators in medical ultrasound. *IEEE Transactions on Ultrasonics, Ferroelectrics, and Frequency Control 50*, 4 (April 2003), 392–401.

[102] Wang, A., Gollapudi, S., May, R. G., Murphy, K. A., and Claus, R. O. Sapphire optical fiber-based interferometer for high temperature environmental applications. *Smart Materials and Structures 4*, 2 (1995), 147.

[103] Wei, G. Generalized Perona-Malik equation for image restoration. *IEEE Signal Processing Letters 6*, 7 (1999), 165–167.

[104] Werner, J., Aneziris, C. G., and Dudczig, S. Young's modulus of elasticity of carbon-bonded alumina materials up to 1450°C. *Journal of the American Ceramic Society 96*, 9 (2013), 2958–2965.

[105] Wolfenden, A. Measurement and analysis of elastic and anelastic properties of alumina and silicon carbide. *Journal of Materials Science 32*, 9 (1997), 2275–2282.

[106] Young, K., Ireland, S., Melendez-Cervates, M., and Stones, R. On the systematic error associated with the measurement of temperature using acoustic pyrometry in combustion products of unknown mixture. *Measurement Science and Technology 9*, 1 (1998), 1.

[107] Yu, P., Li, Q., Fuh, J., Li, T., and Lu, L. Two-stage sintering of nano-sized yttria stabilized zirconia process by powder injection moulding. *Journal of Materials Processing Technology 192* (2007), 312–318.

[108] Yuhas, D. E., Walker, D. G., Mutton, M. J., et al. Methods and apparatus for measuring temperature and heat flux in a material using ultrasound, Sept. 4 2012. US Patent 8,256,953.

[109] Yun, Y., Chung, S. W., and Lee, S. J. *Considerations for the Design and Operation of Pilot-Scale Coal Gasifiers*. INTECH Open Access Publisher, 2012.

[110] Zener, C. Internal friction in solids ii. general theory of thermoelastic internal friction. *Physical Review 53*, 1 (1938), 90.

[111] Zhang, H., Basin, M., and Skliar, M. Itó-volterra optimal state estimation with continuous, multirate, randomly sampled, and delayed measurements. *IEEE Trans. Automat. Control 52* (2007), 401–416.

[112] Zhang, Y., Pickrell, G. R., Qi, B., Safaai-Jazi, A., and Wang, A. Single-crystal sapphire-based optical high-temperature sensor for harsh environments. *Optical Engineering 43*, 1 (2004), 157–164.

[113] Zhou, H.-C., Lou, C., Cheng, Q., Jiang, Z., He, J., Huang, B., Pei, Z., and Lu, C. Experimental investigations on visualization of three-dimensional temperature distributions in a large-scale pulverized-coal-fired boiler furnace. *Proceedings of the Combustion Institute 30*, 1 (2005), 1699–1706.